ENERGY LEVELS AND PROPERTIES
OF A SEMICONDUCTOR QUANTUM WELL SYSTEM:
THE INFLUENCE OF THE SURROUNDINGS AND WELL PARAMETERS

by

SIMON FAFARD

Submitted to the School of Graduate Studies in
partial fulfillment of the requirements
for the degree of Ph.D in Physics

Department of Physics
University of Ottawa

ISBN 0-315-80070-4

A ma famille

ABSTRACT

The constituent layers of a semiconductor quantum well system were studied systematically and sequentially using various spectroscopic and optoelectronic techniques such as photoluminescence, photoreflectance, photovoltage, electro-reflectance, or electroluminescence. Complete single quantum well samples with various well parameters were then studied with the appropriate techniques. The purpose of the study was to find how the energy levels (the bound states as well as the continuum states) of the quantum well structure were influenced by the surroundings (such as the cap layer, the buffer or the substrate) and the well parameters. To that effect, the well width and the alloy composition (x) of an $In_xGa_{1-x}As/GaAs$ single quantum well were varied, and the results obtained with samples having different cap thicknesses (the other parameters being kept the same) were compared. A theory predicting the influence on the energy levels of the cap layer thickness was developed, and experimental evidence was found in modulated reflectance measurements which showed spectral oscillations for energies above the barrier. The behavior is explained by deriving the wavefunction of the carriers with energies larger than the barrier (continuum states) taking into account the finite size of the cap layer. It was also found in the sequential study that in luminescence, depending on the excitation used, the substrate can

contribute to the response obtained with the complete device. The influence of an external perturbation such as an electric field was also studied. Electroreflectance spectra showed that the bound states were Stark shifted, while the peaks of the cap-related oscillations of the continuum states were shifted linearly in energy with the electric field. Study of a multiple quantum well under the same conditions showed that the cap-related oscillations of the continuum states were strengthened by the presence of the additional wells. The theory also predicts that the first well(s), closer to the surface, will be more energy selective in capturing carriers in the continuum. This may result in different capture efficiencies for the various wells of a multiple quantum well structure.

SOMMAIRE

Les couches constitutrices de structures à puits quantiques furent étudiées de façon systématique et séquentielle, en utilisant diverses techniques spectroscopiques et optoélectroniques comme la photoluminescence, la photoréflectance, le photovoltage, l'électroréflectance ou l'électroluminescence. Des échantillons complets à puits quantiques simples furent alors analysés avec les techniques appropriées. Le but de l'étude était de déterminer comment les niveaux d'énergie (autant les états liés que les états du continuum) d'un dispositif à puits quantique(s) sont influencés par leur entourage (la couche capuchon, la couche intermédiaire ou le substrat) et par les paramètres du puits. A cet effet, la largeur et la composition de puits quantiques simples de $In_xGa_{1-x}As/GaAs$ furent variées et les résultats obtenus avec une série d'échantillons ayant différentes épaisseurs de couche capuchon furent comparés. Une théorie décrivant l'influence de l'épaisseur de la couche capuchon sur les niveaux d'énergie fut développée et l'évidence expérimentale fut trouvée dans les spectres de réflectance modulée qui sont marqués par des oscillations aux énergies au-dessus de la barrière. Ce comportement est expliqué en dérivant la fonction d'onde des porteurs ayant des énergies plus grandes que la barrière (les états du continuum) tout en tenant compte que la couche capuchon est d'épaisseur finie.

L'étude systématique a aussi permise de déterminer que selon la source utilisée en luminescence, le substrat peut contribuer au signal obtenu avec le dispositif complet. L'influence d'une perturbation externe, tel qu'un champs électrique, fut également étudiée. Des spectres d'électroréflectance démontrent que l'énergie des états liés est changée par l'effet Stark, tandis que les oscillations des états du continuum, au-dessus de la barrière, voient leurs extrema déplacés de façon linéaire avec le champs électrique. L'étude de puits quantiques multiples dans des conditions comparables a montré que les oscillations des états du continuum sont renforcées par l'ajout des puits supplémentaires. La théorie prédit aussi que le ou les premier(s) puits adjacent(s) à la surface seront plus sélectif(s) en énergie dans la capture des porteurs dans le continuum. Il s'en suit que les différents puits d'une structure à puits quantiques multiples pourraient ne pas avoir la même efficacité de capture.

Statement of Originality

Given below is a list of work done during the course of this study, which to the best of the author's knowledge, had not been previously undertaken:

- Systematic and sequential study of the component layers of a quantum well system.

- Understanding of the influence of Si-doped GaAs substrate on the properties of InGaAs/GaAs quantum wells.

- Theoretical study of the influence of a high potential in the vicinity of a quantum well structure; study of the influence of the finite-size of the cap layer on the bound and the continuum states.

- Experimental evidence of the influence of the finite-size of the cap layer on the continuum states of Single Quantum Wells and Multiple Quantum Wells.

The above work led (or will lead) to the publication of the following papers:

i) Articles:

-S. Fafard, 1992, Energy levels in quantum wells with capping barrier layer of finite size: bound states and oscillatory behavior of the continuum states, accepted on May 29, 1992 for publication in Phys. Rev. B, August 15.

-S. Fafard, E. Fortin, A.P. Roth, 1992, Oscillatory behavior of the continuum states in InGaAs/GaAs quantum wells due to capping barrier layer of finite size, Phys. Rev. **B-45**, 13769, Rap. Comm. (June 15 1992).

-S. Fafard, E. Fortin, and A.P. Roth, 1991, Sequential optical study of the component layers of a semiconductor quantum-well system, Can. J. Phys., 69, pp.346-352.

-E. Fortin, B.Y. Hua, A.P. Roth, A. Charlebois, S. Fafard, C. Lacelle, 1989, Luminescence, level saturation and optical gain in a single InGaAs/GaAs Quantum well, J. Appl. Phys., 66, pp.4854-4857.

ii) Other contributions:

-S. Fafard, E. Fortin, A.P. Roth, 1992, Oscillatory behavior of the continuum states in InGaAs/GaAs quantum wells due to capping barrier layer of finite size, *presented at* the APS meeting at Indianapolis, March 16-20, Bull. Am. Phys. Soc. 37, p. 794.

-S. Fafard, E. Fortin, F. Davidson and A.P. Roth, 1991, Luminescence switching in InGaAs/GaAs single quantum well, *presented at* the First Graduate Student Conference on Opto-electronic Materials, Devices, and Systems, at University of McMaster, Hamilton, Ont. June 24-26.

-S. Fafard, 1990, Evolution of the energy levels in semiconductor quantum wells, *presented at* the Ottawa-Carleton Institute of Physics Graduate student symposium, Fall 1990 at University of Carleton.

-S. Fafard, E. Fortin and A.P. Roth, 1990, Sequential optical study of the component layers of a semiconductor quantum-well system, *presented at* the Fifth Canadian Semiconductor Technology Conference, in Ottawa August 14-16.

-S. Fafard, E. Fortin and A.P. Roth, 1990, Sequential optical study of the component layers of a semiconductor quantum-well system, *presented at* 1990 CAP Conference in St-John's Newfoundland, Physics in Canada, vol 46, May '90, p.53.

iii) Submitted or in preparation:

-S. Fafard, E. Fortin, and A.P. Roth, 1992, Influence of the electric field on the energy levels of an InGaAs/GaAs Single Quantum Well, Phys. Rev. B.

-S. Fafard and E. Fortin, 1992, Low intensity "switching" of the photoluminescence due its nonlinearity with excitation in InGaAs/GaAs single quantum well, J.Appl.Phys..

The study has also led to the publication of other papers which are not directly related to Quantum Wells:

-E. Fortin, S Fafard, A. Anedda, F. Ledda and C. Charlebois, 1991, Photoluminescence of $MgIn_2S_4$ and $HgIn_2S_4$, Solid State Commun., 77, pp.165-167.

-S. Fafard, E. Fortin, 1990, Electroluminescence in $CdIn_2S_4$ thin films, Thin Solid Films, 187, pp.245-251.

-S. Fafard, E. Fortin, P. Bernard, M. Goléa, 1988, Optoelectronic properties of thin $CdIn_2S_4$ films, *presented at* the 1988 CAP Conference at Montreal, Physics in Canada, vol 44, #3, May '88, p. 74.

-S. Fafard, E. Fortin, P. Bernard, M. Goléa, 1988, Propriétés optoélectroniques des couches minces $CdIn_2S_4$, *presented at* the 1988 ACFAS Conference at Moncton, Les Annales de l'ACFAS, vol 56, p. 167.

ACKNOWLEDGEMENTS/REMERCIEMENTS

Je voudrais remercier Dr. Emery Fortin pour m'avoir introduit aux propriétés optiques des semiconducteurs, il y a de cela déjà 5 ans; d'avoir mis à ma disposition un laboratoire pourvu d'équipements à la fine pointe de la technologie; d'avoir rendu possible ma participation à plusieurs conférences scientifiques où les plus récentes découvertes sont échangées et finalement, pour ses conseils tout au long du projet.

Also I would like to thank Dr. Alain Roth, and his team at the Institute for Microstructural Sciences at the National Research Council of Canada, without whom the project on the quantum wells could have been no more than a theoretical idea. The good samples he provided us with, custom designed to our specific research needs, were very much appreciated. Thank you also to S. Rolfe for the SIMS measurements of the cap layer thicknesses. Thanks are also due to the staff of the physics department for their technical support; in particular to Roger Chagnon because he introduced me to the McIntosh technology, which was indispensable for the production of the figures for the thesis and the publications.

Je voudrais remercier Francine, Mélissa et toute ma famille pour leur patience et leur soutien pendant l'accomplissement de mes études.

Finally, I would like to acknowledge the Natural Sciences and Engineering Research Council of Canada (NSERC) and the University of Ottawa for the Scholarships.

TABLE OF CONTENTS

Abstract.. iii
Sommaire.. v
Statement of originality........................ vii
Acknowledgements/Remerciements.................. x
Table of contents............................... xi
List of figures................................. xiii
List of tables.................................. xvii
Introduction.................................... 1

1 Theoretical evaluation of the energy levels of Single Quantum Wells (SQW):

1-1 SQW with barriers of infinite spatial extent, in the absence of an electric field............. 10
1-2 Presence of a uniform electric field............ 18
1-3 SQW with a finite cap layer, in absence of an electric field.................................. 21
1-3-1 Bound states........................ 21
1-3-2 Continuum states.................... 25
1-4 Presence of a uniform electric field............ 39

2 Experimental Techniques:

2-1 Sample growth and preparation.................. 49
2-2 Photoluminescence (PL)......................... 53
2-3 Photoreflectance (PR) and Electroreflectance (ER)......................... 60
2-4 Photovoltage (PV) and Electroluminescence (EL).. 68

3 Influence of the surroundings, and of the well parameters on the energy levels of SQW samples:

3-1 Sequential study of the influence of the substrate and buffer layers.................... 76
3-1-1 Substrate................................ 77
3-1-2 Buffer................................... 79
3-1-3 Complete SQW............................ 83
3-2 Influence of the cap........................... 98
3-2-1 Without an electric field................ 98
3-2-2 With an electric field.................. 107

4 Multiple Quantum Wells (MQW):

4-1 Theory for bound states........................ 131
4-2 Theory for the continuum states................ 141
4-3 Experimental results........................... 146

Conclusions.. 151

Appendix 1: Collecting PL with 2 lenses.................. A-1
Appendix 2: Optimization of the efficiency of a monochromator using a single mirror to collect the light.......................... A-4
Appendix 3: Analogy between the condition for bound states of MQW and Legendre's polynomials A-8

References..xviii

LIST OF FIGURES

1-1: a) SQW surrounded on each side with barrier of infinite extent. b) Corresponding band diagram..... 11

1-2: Well width dependence of the energy levels of $In_{0.135}Ga_{0.865}As/GaAs$ SQWs............................ 16

1-3: SQW with a capping barrier layer of finite size a), and its band diagram b)........................ 22

1-4: Well width dependence of the bound states of $In_{0.16}Ga_{0.84}As/GaAs$ SQWs for various values of cap thicknesses.................................. 24

1-5: Energy variation of the normalized probabilities of finding the electrons in the cap a), well b), and buffer c) regions of a SQW with a 50 nm cap, and a well width of 3.5 nm......................... 31

1-6: Wavefunction for the first 2 peaks of fig. 1-5, in a) and b); and an off resonance situation c).... 34

1-7: Energy variation of the normalized probabilities of finding the heavy holes in the cap a), and in the well b) regions. Same SQW as fig. 1-5.......... 36

1-8: Band diagram of a SQW with a capping barrier layer of finite size when an applied electric field lowers the potential away from the surface... 40

1-9: Normalized probabilities of finding the heavy holes in the cap a), and in the well b) for various values of electric field. Same SQW as fig. 1-5 44

1-10: Shifts of the peaks with the applied field 46

2-1: Component layers of a SQW studied sequentially. Substrate a), buffer b), complete SQW c), and corresponding band diagram d) 51

2-2: SQW with electrical contacts 52

2-3: Position dependence of the transmission of light through semiconductor material with various values of absorption coefficient 55

2-4: Set-up for PL, collecting the emitted light with two lenses 56

2-5: Total internal reflection and critical angle of a semiconductor slab in PL experiments 59

2-6: Fit of the line shape of the 11H transition obtained in PR using various values of m_j in eq.(2-2) 65

2-7: Optimization of the throughput of a monochromator; PR and ER set-up 66

2-8: Electric field dependence of the PL emitted by a SQW for various excitation intensities 71

2-9: Dependence of the PL on the intensity of excitation for various values of electric field 71

2-10: ER excited with an external power supply a), and internally with the PV effect b) 73

3-1: PV a), EL b), and PL c) of a Si-doped GaAs substrate.. 78

3-2: PV a), PL with λ_{exc}= 514.5 nm b), EL with an Au barrier c), and EL with an ohmic contact for a 2.0 μm thick buffer layer........................... 80

3-3: PL spectra of a 0.5 μm thick buffer layer for λ_{exc} = 5'4.5 nm a), and λ_{exc} = 632.8 nm b)........... 82

3-4: PV a), PL with λ_{exc} = 514.5 nm b), and PL with λ_{exc} = 632.8 nm for the complete SQW with X = 0.135, and L = 5.0 nm.............................. 84

3-5: Comparison of the PL results obtained with the 0.5 μm buffer layer a) and b), and the SQW sample c) and d); a) and c) are excited at λ = 514.5 nm, and b) and d) are excited at λ = 632.8 nm.......... 86

3-6: High intensity PL spectra of the SQW............... 88

3-7: High intensity PL spectra of the corresponding buffer layer.. 88

3-8: EL of the SQW with X = 0.135, and L = 5.0 nm, for different type of contact.......................... 90

3-9: PR a) and ER b) of a 0.5 μm thick buffer layer..... 95

3-10: E_n vs $(n - 1/2)^{2/3}$ plots for the F.-K. oscillations of fig. 3-9b......................... 96

3-11: Dependence of the electric field on the applied voltage as found from fig. 3-10................... 97

3-12: PR of a SQW with t = 50 nm and L = 3.5 nm (sample 1)... 100

3-13: E_n vs n^2 plot for various samples, for the above-barrier cap-related oscillations............ 102

3-14: PR of a SQW with t = 65 nm and L = 3.5 nm (sample 2).. 106

3-15: ER for various applied voltages, for sample 1...... 108

3-16: Electric field dependence, for fixed energies above the barrier, of the calculated well occupancy a), and of the experimental ER signal b).. 111

3-17: ER spectra of sample 1 compared at various temperatures.................................... 113

3-18: ER for various applied voltages, for sample 2...... 114

3-19: ER for various applied voltages, for a SQW with t = 100 nm, and L = 3.5 nm (sample 3)............... 116

3-20: ER for various applied voltages, for a SQW with t = 67 nm, and L = 12.0 nm (sample 4)............... 119

3-21: Stark shift of the 11H transtion for sample 4...... 121

3-22: ER for various applied voltages, for a SQW with t = 67 nm, and L = 8.0 nm (sample 5)................ 123

3-23: Stark shift of the 11H transition: a); and shifts of intermediate transtions of sample 5: b)......... 125

3-24: ER of sample 4 and 5 at higher sensitivity, showing the above-barrier cap-related oscillations.................................... 128

4-1: Well width dependence of the bound states of an $In_{0.16}Ga_{0.84}As/GaAs$ system with the calculated bandwidths for superlattices having barriers of 5.0 and 10.0 nm.......... 133
4-2: Band diagram of a MQW with n wells.......... 135
4-3: Bound state(s) for a SQW, DQW, and so on, up to a MQW with 6 wells; for the first bound electron states with L = 8.0 nm, d = 10.0 nm, V = 121 meV. a) is for cap layer thicknesses t $\gtrsim$ 10.0 nm, b) is for t = 2.5 nm, and c) shows the cap layer dependence of the energy levels.......... 137
4-4: Energy variations of the normalized probabilities of finding the electrons in the various regions of a DQW as in fig. 1-5, with d = 5.0 nm.......... 144
4-5: PV spectrum, at T = 77 K, of a MQW sample with 5 wells, with L = 8.0 nm, and d = 10.0 nm, and t = 65 nm.......... 147
4-6: ER spectra at T = 77 K of the MQW of fig. 4-5 for bias voltages between -1.4 and 1.4 V.......... 149

A-1: Legendre's polynomials.......... A-9
A-2: Comparison between $P_5(x)$ and eq. (4-3a) for a MQW with 5 wells.......... A-10

LIST OF TABLES

3-1: Parameters of the SQW sample studied.......... 76

INTRODUCTION

From the simple particle in a box to the entire crystalline lattice, a variety of quantum mechanical textbook problems[L80] became available for direct study and applicable to technology due to the precision achieved with the modern epitaxial growth techniques of solids. Indeed, Single Quantum Well (SQW), Multiple Quantum Well (MQW), Superlattice (SL), or other semiconductor devices of reduced dimensionality[†] , owe their interesting properties to the physical size of the active layers. And so, in addition to the bandgap engineering[W87,WV91] which controls the depth of the well(s), size engineering of the active layers and of the cladding layers permits to adjust the properties of quantum well devices to a specific need[NH86]. Indeed, depending on the probing technique, the cladding layers surrounding the active quantum well region may also contribute to the phenomena observed with the complete device[FF91]. Little research had been done on the influence of the spatial extent of these cladding layers; a good understanding of their physical properties, or of their influence on the physics involved with the active layers, is required in a multi-element semiconductor system since it is sometimes difficult to establish the exact origin of some features obtained in spectroscopic studies of such devices. At times, it is tempting to forget the presence of the cladding layers

† *B88, BB91, SC91b, MP91*

and their influence on the results obtained with the complete device, or to make use of standard excitation wavelengths in photoluminescence without considering the consequences of this choice on the response of the cladding layers. Whether a transition originates from the QW itself, from the cladding layers (including sometimes the substrate), or both, may not be unambiguous in all instances[FH89a].

If the carriers diffuse coherently throughout the device, remote interfaces can become an important part of the potential configuration. In the ideal model commonly used in calculations, a quantum well structure is considered to be surrounded by potential barriers of finite height but infinite spatial extent on each side. In most cases, the barrier on the side of the buffer layer extends over a large distance (of the order of 1 μm); however the cap layer on the other side of the well is generally much thinner, and so the energy distribution of the carriers in the vicinity the well may be modified by the presence of the external surface which represents a high potential for these carriers within the semiconductor. The influence of the surface potential will be more important for continuum states than for bound states since the wavefunctions of the former are not restricted to the well region.

Even in the absence of a nearby high potential, simple calculations show the presence of resonant states in the continuum for energies at which a particle has a probability of transmission above the quantum well equal to unity. These continuum states are believed to play an important role in the capture of the carriers by the well [BZ84,BB86] even though there is little experimental evidence to that effect and the results are sometimes contradictory[D90,ZP84]. In any case, the continuum states play an important role because they are the states in which the carriers are first created when excitation energies larger than the barrier are used.

To facilitate the identification of the optical transitions observed with the strained InGaAs/GaAs system, a systematic and sequential study was performed on the component layers of an $In_{0.13}Ga_{0.87}As/GaAs$ SQW. The sequential study will help to distinguish between transitions originating from cladding layers and those whose origin is associated to the presence of the quantum well, providing us with a good understanding of the influence of each layer. The type of cladding layers (GaAs substrate, buffer, and cap layers) studied here are common to many QW systems, and so that the conclusions presented here could be applicable to other systems as well.

In particular, this work will describe the effects of the high potential at the device surface on the continuum states[O90,PA92] of such SQWs having thin ($t < 100$nm) cap layers. The influence of a high potential in the vicinity of a

SQW structure will be considered theoretically in chapter 1. Such a configuration would represent a quantum well device having a cap layer of finite size. It will be assumed that the external surface of the cap layer represents an infinitely high potential. This will be a good assumption for energies up to a few hundred meV in the continuum, given that the actual height of the surface potential will be of the order of few eV (the work function of the carriers in the semiconductor). The envelope function will be required to vanish at the external surface. This will be valid for the treatment of an ideal free surface, and merely illustrates the fact that for the energy range of interest, the carriers cannot escape the semiconductor crystal. The model developed here also applies to quantum well structures terminated with a material having a band gap much larger than the barriers[O90] (such as AlGaAs/GaAs/InGaAs/GaAs), even though these structures will not be discussed specifically in this work. The presence of impurity, or defect surface states would change the problem, but once these localized states are filled, this problem could also be solved by assuming that the envelope wavefunction vanishes at the surface, taking into account the resulting band curvature. Such band curvature could be considered by approximating the curved potential with a series of small linear potential segments[LF86,H91]. Here for simplicity and clarity, the theory will consider analytically the cases of a flat band potential, or a uniformly applied linear potential.

It is found that the bound states would be influenced only in the case of very narrow cap layers ($t \lesssim 10$ nm); but for the continuum states, the high potential at the surface of the cap and the finite-size of the cap layer produce quantum interference in the wavefunctions which leads to oscillations in the probabilities of finding the carriers in the various regions of the structure. In the flat band condition, the modulation is expected to be set mainly by $\sin^2(k_b t)$, where t is the thickness of the cap layer, and k_b is the wavevector in the barrier and includes the carrier effective mass. Because of this effective mass and the cap layer dependence, the cap-related oscillations should observable for the various types of carriers depending on the value of t. The amplitude of the oscillations was found to depend on the well width. As an electric field lowers the potential away from the surface, the extrema of the oscillations in the probabilities are found to shift linearly with the electric field.

The theory developed for the effect of the finite-size of the cap layer is in no way restricted to the InGaAs/GaAs system, but since the barrier is the GaAs, the samples are naturally barrier-terminated, and chances of getting a nearly perfect external surface (GaAs cap layer) are greater than if an alloy is used for the barrier, as in the AlGaAs/GaAs system for example. The AlGaAs/GaAs samples often have a GaAs cap layer on top of the AlGaAs barrier, and this would correspond to a different potential configuration.

Chapter 2 will briefly describe the samples studied and the experimental techniques used, with particular attention given to the optimization of the experimental conditions. It will also discuss the method used to analyze the data, and the physics of the experimental techniques. Chapter 3 deals with the exerimental results, and is divided in two main sections: sect. 3-1 uses a sequential study to demonstrate the influence of the substrate and buffer layers. The sequential study shows that when the experimental conditions permit the excitation of the substrate, a peak of substrate origin whose amplitude is comparable to that of the fundamental peak of quantum well origin (11H) could be observed. In photoluminescence, long-wavelength excitation, a thin buffer layer, or high intensities of excitation may enhance emission from the underlying substrate. The nature of the contact used in the electroluminescence and photovoltaïc effects may also influence the relative response of the component layers.

In the second part of chapter 3, sect. 3-2, experimental results are given for the influence of the cap layer. Photoreflectance (PR) spectra of InGaAs/GaAs SQWs have shown above-barrier oscillations of amplitude comparable to those of transitions involving only bound states. The oscillations follow the relation $E_n = E_o + \alpha\ n^2$ for the n-th extremum at an energy E_n (E_o is the energy of the barrier, and α is a constant). These results demonstrate experimentally that the continuum states are influenced by the finite extent of the barrier on the side of the well which terminates the device (the cap layer). Also as predicted, depending on the value of t, these cap-related oscillations are observed for the various types of carriers in photoreflectance experiments, while their visibility depends on the well width.

Sect. 3-2 also describes the effect related to an external perturbation such as an applied electric field. Electroreflectance (ER) techniques allow quantitative control of the applied electric field, and therefore for the study of its influence on the bound and the continuum states in the quantum well structures. Results showed that in the case of transitions involving bound states only, the electric field influences the selection rules of the transitions and the energy levels are Stark shifted as expected. As was the case in the flat-band condition (i.e. in PR), the finite-size of the cap layer did not have any drastic influence on the bound states for the cap thicknesses studied. For the continuum states however, the extrema of the above-barrier oscillation are shifted linearly as the applied field is changed, and the shifts are different for different cap thicknesses. These findings were expected theoretically from the calculations of chapter 1.

Finally, the influence of additional wells in the case of MQWs is studied in chapter 4. Calculations for the bound states (considering the exact number of wells) show that the well adjacent to the surface will be influenced similary to what was found for the case for the SQW. It is also theoretically predicted and experimentally found that the additional wells strengthen the cap related oscillations of the continuum states. The theory also predicts that the well(s) closer to the external surface will be more energy selective in capturing carriers in the continuum. This may result in different capture efficiencies for the various wells of a multiple quantum well structure.

CHAPTER 1

THEORETICAL EVALUATION OF THE ENERGY LEVELS OF SINGLE QUANTUM WELLS.

1-1 SQW with barriers of infinite spatial extent in absence of an electric field........................ 10

1-2 Presence of a uniform electric field................ 18

1-3 SQW with a finite cap layer, in absence of an electric field.. 21

1-3-1 Bound states............................. 21

1-3-2 Continuum states......................... 25

1-4 Presence of a uniform electric field................ 39

The first two sections of this chapter review the calculations usually performed to obtained the energy levels of SQW structures, considering the barriers surrounding the well to be of infinite spatial extent. A slightly different approach will be described in sect. 1-1 to calculate the bound states in such structures. A convenient picture of the evolution of the energy levels (as the well width is changed) is easily obtained using this method. In the last two sections, the problem of SQW having cap layer of finite extent will be introduced. The resulting changes in the physical properties expected from these calculations will be discussed with several examples pertinent to the experimental study of chapter 3.

1-1 SQW with barriers of infinite spatial extent, in the absence of an electric field.

A SQW potential is created when a semiconductor layer is embedded between layers of semiconductor material having a larger band gap as shown in fig. 1-1a. The semiconductor with the smaller band gap grown in the middle of the structure forms the well, and fig. 1-1b shows the corresponding band diagram if the barriers surrounding the well are of infinite spatial extent. The solutions for the bound states of such a potential are well known[†], they are found by solving separately for each type of carriers using the Envelope Function Approximation and, for simplicity, by assuming parabolic bands. The envelope wavefunctions (in the direction of the crystal growth) are constructed from an exponentially decaying function in the barriers, and sine and cosine functions for the well. Matching the wavefunction and its derivative divided by the effective masses (the particle current density is conserved) at the interfaces one readily obtains the condition for the bound states:

[†] *L80, W87, B88, BB91*

Fig. 1-1: a) Hypothetical SQW surrounded on each side with barrier of infinite spacial extent.

b) Corresponding band diagram if the electrons and the holes are confined in the well.

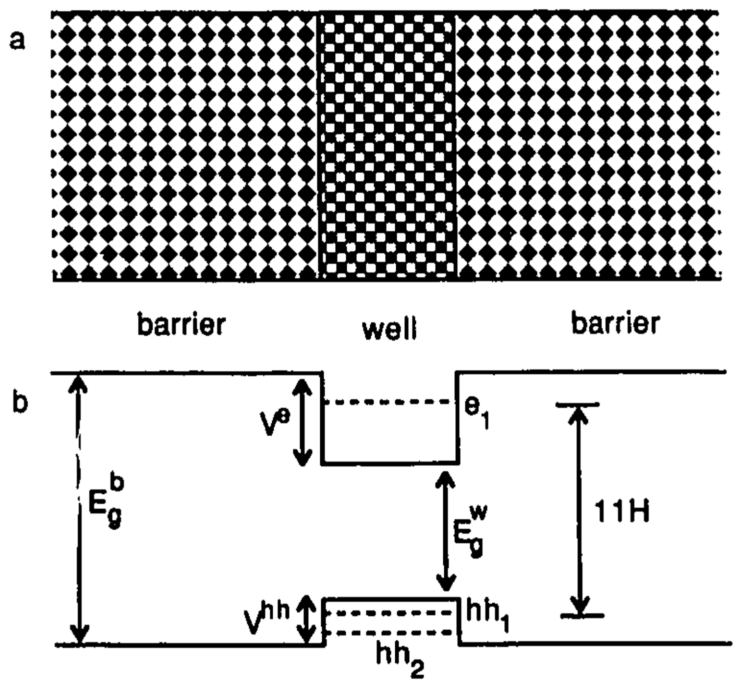

$$\xi = \tan\,(k_w L/2),\ \text{and}\ -\xi = \text{cotg}\,(k_w L/2) \qquad (1\text{-}1)$$

for the even and odd states respectively. If the energy ε is measured from the bottom of the well of depth V, then

$$k_w = \left[\frac{2m_w^*}{\hbar^2}\,\varepsilon\right]^{1/2},\ k_b = \left[\frac{2m_b^*}{\hbar^2}\,(|V|-\varepsilon)\right]^{1/2} \text{ and } \xi = k_b/k_w =$$

$$\left[\frac{m_w^*}{m_b^*}\,\frac{(|V|-\varepsilon)}{\varepsilon}\right]^{1/2}$$; m_b^* and m_w^* are carrier effective masses in the barrier and in the well respectively.

For the rest of sect. 1-1, an approach which gives a convenient picture of the evolution of the energy levels as the well width is changed (the other parameters being kept fixed) will be presented[FF91]. In addition to its importance in sample characterization, this method is particularly useful in sample design. The even and odd solutions of eq. (1-1) are regrouped for convenience in one equation as follows:

$$\left[\tan\left(\frac{L}{2\hbar} \sqrt{(2m_w^*\varepsilon)} \right)\right]^{(-1)^{(n+1)}} - (-1)^{(n+1)} \times \sqrt{\frac{m_w^*}{m_b^*} \left(\frac{V}{\varepsilon} - 1 \right)} = 0 \tag{1-2}$$

where n is related to the parity of the corresponding wave-function: $n = 1, 2, \ldots, n_{max}$;

$$n_{max} = 1 + \mathrm{INT} \left(\frac{L}{2\hbar} \sqrt{(2m_w^*V)} \Big/ \pi/2 \right) \tag{1-3}$$

is just the number of quadrants that the argument of the tangent goes through when $\varepsilon \rightarrow V$ (the confinement potential). There is one and only one solution ε_n (the n^{th} bound state) per quadrant (i.e. per integer multiple of $\pi/2$). It is easy to show that this implies that the energy of the n^{th} state of the finite well has to satisfy the inequality:

$$\varepsilon_{n-1}(L,\infty) \leq \varepsilon_n \leq \varepsilon_n (L,\infty),$$

where

$$\varepsilon_n(L,\infty) = \frac{\hbar^2}{2m_w^*} \left(\frac{n\pi}{L} \right)^2 \tag{1-4}$$

is the n^{th} energy level of the infinitely deep well having the same width L. The latter inequality is of interest when one wants to find the numerical solutions of eq. (1-1). It restricts the energy domain in which the search for the solution ε_n has to be carried out. In order to take into account the band non-parabolicity[NM87], one can make use of energy-dependent effective masses arising from various band interactions[PS90,RC90,B88]. Calculations showed that the use of such energy-dependent effective masses can improve the accuracy of the results for the energy of the higher-lying levels in wide wells by several meV in the case of electrons, but no appreciable shifts are expected for narrow wells, low-lying states or for the heavy-holes[R88]. For the system of interest here (InGaAs/GaAs), the light holes are not confined in the well because of the lattice-mismatched induced strain which will displace the light hole valence band edge of the well below that of the barrier[P88]. Therefore confinement of the light holes in SQW will not be considered since the light holes would occupy the cladding layers (buffer and cap) which have dimensions too large, and a barrier too low to obtain significant confinement effects.

Instead of solving eq. (1-1) numerically (as is usually done[W87,B88]) in order to get the bound energy levels (ε_n) for the electrons and holes, it is possible to transpose eq. (1-2) to solve analytically for $L = f(\varepsilon_n)$, i.e.: the well width required to get the n^{th} level at an energy ε_n. We obtain:

$$L(\varepsilon_n) = \frac{2\hbar}{\sqrt{(2m_w^{*}\varepsilon_n)}} \times \left[\tan^{-1}\left((-1)^{(n+1)} \times \left(\sqrt{\frac{m_w^{*}}{m_b^{*}}\left(\frac{V}{\varepsilon_n} - 1\right)} \right)^{(-1)^{(n+1)}} + \mathrm{INT}\left(\frac{n}{2}\right) \times \pi \right) \right] \tag{1-5}$$

Using eq. (1-5) for energies smaller than the electrons and the heavy holes confining potentials, V^e and V^{hh} respectively, for all the bound electron and heavy-hole states, the well-width dependence of the energy levels (and hence of the transitions in the well) is obtained. For excitonic transitions, the energy of the transition must be reduced by the binding energy of the exciton. This approach (using eq. (1-5) instead of calculating point by point) gives a powerful method of getting an overview of the possible transitions for a given depth of well (which is fixed by the choice of the composition of the alloy forming the well).

For energies larger than the confinement potentials, the electrons and holes can have any energy (continuum of energies). However, one may observe *resonant* states when the energy satisfies $\varepsilon = \varepsilon_n(L,\infty)$ with $n \geq n_{max}$, where $\varepsilon_n(L,\infty)$ and n_{max} were defined previously in eqs. (1-3) and (1-4) (ε is measured from the bottom of the well). For these energies, the transition coefficient T over the well, which is given[L80] by

$$\frac{1}{T} = 1 + \frac{1}{4} \sin^2\left(\sqrt{\left(\frac{2m_w^*}{h^2} (\varepsilon + |V|)\right)} \times L\right) \times \left(\xi - \frac{1}{\xi} \right)^2 , \qquad (1\text{-}6)$$

with $1/\xi = \left(\frac{m_w^*}{m_b^*} \times \frac{\varepsilon}{(\varepsilon + |V|)} \right)^{1/2}$,

is equal to unity since the argument of the sine term is equal to an integral multiple of π. For energies around these values, the transmission coefficient T can differ significantly from unity if the energy is not too high above the confining potential (V). These resonances in the transmission coefficient may create virtual levels which could have an important role in the capture of carriers[Bz84,BB86]. Transitions involving these *resonant continuum states* are observable[D90,BB86,ZP84] even though experimental evidence is not always clear-cut since these transitions could often have energies close to that of other possible transitions. For energies much larger than the confining potential (V), $\xi \to 1$ and $T \simeq 1$ for all energies, hence only few resonant continuum states, at energies close to the confining potential, are expected for QW structure surrounded with barriers of infinite spatial extent.

To illustrate the results expected with this model (which considers barriers of infinite spatial extent) for an $In_xGa_{1-x}As/GaAs$ SQW system, fig. 1-2 displays the well width dependence for X = 0.135 as calculated by the above method.

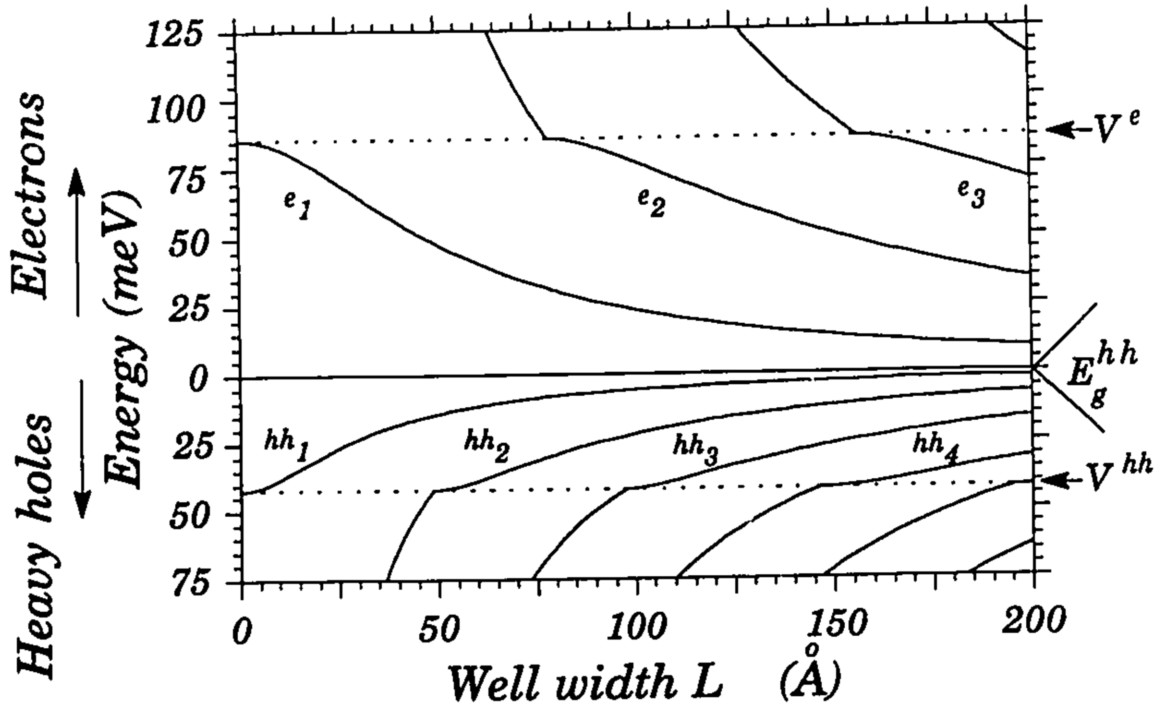

Fig. 1-2: Well width dependence of the energy levels of an $In_{0.135}Ga_{0.865}As/GaAs$ SQW. The energy of a transition ijH for a given well width is obtained from $E_{ijH} = e_i + hh_j + E_g^{hh}$. Where $E_g^{hh} = 1.380$ eV at T = 77, for that alloy composition. The dashed horizontal lines represent the onset of the continua (V_e = 86 meV and V_{hh} = 42 meV). The curves for energies larger than the confining potential (V's) represent the resonant continuum states, for which the transmission coefficient T over the well is equal to unity.

Knowing the well energy gap, $E_g^w = E_g^{InGaAs}$, and the barrier energy gap, $E_g^b = E_g^{GaAs}$, one can find the strained heavy-hole gap E_g^{hh} [BP74,P88,D90], and hence V^e and V^{hh} (the confinement potentials) are found from

$$V^e = (E_g^{GaAs} - E_g^{hh}) \times (1 - Q_v)$$
$$V^{hh} = (E_g^{GaAs} - E_g^{hh}) \times Q_v$$

Where Q_v is the valence band offset taken here as Q_v = 0.33[P88,D90,JJ88]. At T = 77 K, calculations give V^e = 86 meV,

V^{hh} = 42 meV, and E_g^{hh} = 1.380 eV. The dashed horizontal lines in fig. 1-2 represent the onset of the continua; the curves above the V's represent the resonant continuum states found from eqs. (1-4) and (1-3), for which T found from eq. (1-6) is equal to unity; and the curves below the V's represent the energy of the bound states as found from eq. (1-5). The energy of a transition from an electron state e_i to a heavy-hole state hh_j is simply given by the sum of these two (e_i + hh_j), plus the value of the strained heavy-hole gap E_g^{hh} which is taken to be independent of the well width. As mentioned above, if the transitions are excitonic in nature, this value must be reduced by the binding energy of the exciton. As it can be seen, this approach [using eq. (1-5) instead of calculating point by point with eq. (1-1)] gives a powerful method of getting an overview of the possible transitions for a given alloy composition at a specific temperature.

The sample used in the sequential study of sect. 3-1 has a well width of 5.0 nm, and X = 0.135, and so the possible transitions for this sample can be found from fig. 1-2: e_1 = 48 meV, hh_1 = 14 meV and hh_2 = 42 meV. The 11H transition is thus at E_{11H}= 48 meV + 14 meV + 1.380 eV = 1.442 eV. Hence, for a binding energy of 8 meV for the exciton[HS90], an excitonic 11H transition is expected at 1.434 eV (864.5 nm), and the other possible transitions are:

11H at E = 1.434 eV; 864.5 nm (excitonic),
12H at E = 1.470 eV; 843 nm,
ec-1H at E = 1.480 eV; 838 nm,
e1-cH at E = 1.470 eV; 843 nm,

where ec-1H means a transition from the electron continuum to hh_1, and similarly e1-cH is a transition from e_1 to the heavy-hole continuum.

This section gave the necessary background to calculate the bound and continuum energy levels in SQW under the flat band conditions, for barriers of infinite extent. The next sections will describe the modifications imposed on these energy levels by conditions often encountered in actual devices, such the application of an electric field, or having at least one barrier of finite spatial extent.

1-2 Presence of a uniform electric field.

The previous section was devoted to the presentation of bound and continuum states of SQW under flat-band conditions. In this section the case of an external and constant electric field superimposed on the band edge profile is examined with the assumption that the barriers surrounding the QW structure are of infinite spatial extent. The problem for the bound states has been investigated both theoretically and experimentally by several authors†. The envelope function solutions of the Schrödinger equation in the direction of crystal growth are Airy functions instead of the sine, cosine and exponentially decaying functions previously used to obtain eq. (1-1). However, if the barriers are assumed infinite in spatial extent, a constant electric field leads to a pathological behavior of the eigenstates of the resulting Schrödinger equation as a function of the field[BB91]. At zero field the Schrödinger equation admits a small number of bound states (given by eq (1-3) which depends on the values of L and V), while an arbitrarily small field is sufficient to transform the allowed energy spectrum into a continuum. This occurs because the potential energy for the barrier on the side of the well which is pushed down in energy with the electric field can be taken arbitrarily negatively large at distances large enough from the well, since the barriers are assumed to be of infinite extent. Nevertheless, the shifts in the energy of the bound states can be evaluated using various numerical acrobatics. For example one can cut off the electric field at some large distance from the investigated quantum well and impose the existence of an infinitely high barrier, as is the case for a finite but large crystal. In any case, the field leads to a shift to lower energy of the ground electron and hole states and, thus, of the fundamental band-

† *e.g.: IM87, TG91, W87 p.306, BB91 p.302*

to-band transition[BM83,MC84]. Going a step further, Trzeciakowski et al.[TG91] have studied the continuum states assuming a finite but large crystal (so that the energy spectrum is discrete but dense for calculation purposes). They predict oscillatory behavior for the continuum states for fields of polarity raising the potential, in the semiconductor, away from the surface. The spacing between the peaks of the oscillations decreases as the energy increases, in a way similar to the Franz-Keldysh oscillations[A80,CV90,CC91].

The study of the SQW under an applied electric field leads to interesting phenomena such as shifts in the energy levels, or appearance of above-barrier oscillations. But as discussed above, it could be more informative to consider crystals of finite size corresponding more closely to the physical situation. The next sections will treat the case of SQWs with one of the barrier layers (the cap layer) of such finite extent.

1-3 SQW with a finite cap layer, in absence of an electric field.

Most of the calculations dealing with SQWs are usually performed using the approaches described in the previous sections, considering barrier of infinite spatial extent on each side of the well. However, consideration of the finite size of the barrier(s) leads to interesting phenomena, especially for the continuum states. For a SQW structure having a finite cap layer, as shown in fig. 1-3a, the problem is to solve the Schrödinger equation for the corresponding potential depicted in fig. 1-3b. For a thick cap layer ($t \to \infty$) this potential reduces to the "*regular*" SQW potential problem (i.e.: finite height, but infinite extent of the barrier on each side) as discussed in sect.1-1. In the following subsections, theory is developed for quantum well structures having thin cap layers.

1-3-1 Bound states:

For $E < 0$ (see fig. 1-3b) the wavefunction $\Phi(x)$ is constructed in the following manner: it is required that $\Phi(0)=0$ since the potential is assumed infinitely high for $x \leq 0$; furthermore $V(x) > E$ in region I, and so the solution of the Schrödinger equation takes the form $\Phi_I(x) \propto \sinh k_b x$. In regions II and III the wavefunction is obtained in the usual

Fig. 1-3: a) SQW with a capping barrier of finite size; cap of width t, well of width L and depth V, and thick buffer layer.

b) Corresponding band diagram for the flat band condition. Region I and III are made of semiconductor material B with an effective mass m_b^*, and region II is made of semiconductor A with an effective mass m_w^*.

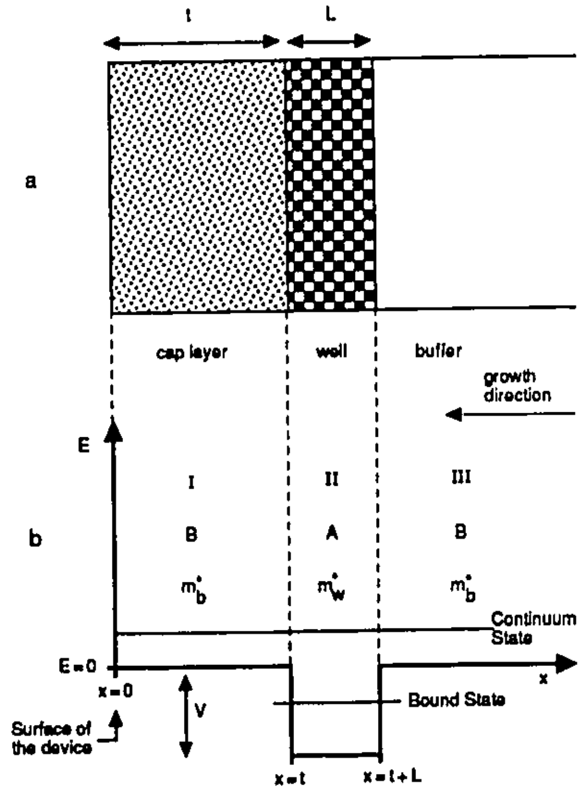

way: it is a combination of sine and cosine functions in the well region, and an exponentially decaying function for the buffer region. Matching at the interfaces the wavefunction and its derivative divided by the effective masses of the material (i.e. the particle current density), one readily obtains the condition for bound states:

$$2 \cos k_w L = \sin k_w L \left[(1/\xi - \xi) - e^{-2k_b t} (1/\xi + \xi) \right]. \qquad (1\text{-}7)$$

The symbols have the same meaning as in eq. (1-1) if the energy is measured from the bottom of the well ($\varepsilon = |V| - |E|$).

Eq. (1-7) has two limiting cases of interest: a) for large t (i.e. a *regular* SQW), it reduces to $2 \cos k_w L = \sin k_w L \, (1/\xi - \xi)$. It is easy to show that this gives the well-known eq. (1-1) for *regular* SQWs; b) $t \to 0$, i.e. a semi-infinite SQW, leads to $\cos k_w L = -\xi \sin k_w L$, or equivalently, $-\xi = \mathrm{cotg}\, k(2L_w)/2$, which gives the odd levels only of a *regular* SQW twice as wide. This is expected, since the odd levels of a *regular* SQW twice as wide will always have a node at their center, just as the semi-infinite SQW will have a node (the wavefunction is terminated) at the surface. Since only the odd levels are present, the semi-infinite SQW will have no bound states for $L < \dfrac{\pi\hbar}{2\left(2m_w^* V\right)^{1/2}}$ (i.e. until the second level appears in the *regular* well of twice the width having the same potential depth).

Between those limiting cases, eq. (1-7) was used to calculate the influence of the cap layer thickness t on the bound energy levels of SQWs. Fig. 1-4 gives an example of results for a system having confining energies V^e = 121 meV and V^{hh} = 60 meV for the electrons and heavy holes respectively, for well widths ranging from 0 to 10.0 nm. The effective masses were taken to be $m_w^* = m_b^* = 0.0665\ m_o$ PS90 for the electrons and $m_w^* = 0.37\ m_o$, $m_b^* = 0.41\ m_o$ for the heavy holes. Those values correspond to an $In_{0.16}Ga_{0.84}As/GaAs$ system which will be experimentally studied in sect. 3-3. The solid lines are for the *regular* SQW (i.e. $t \to \infty$). The –.–.–.– line is for

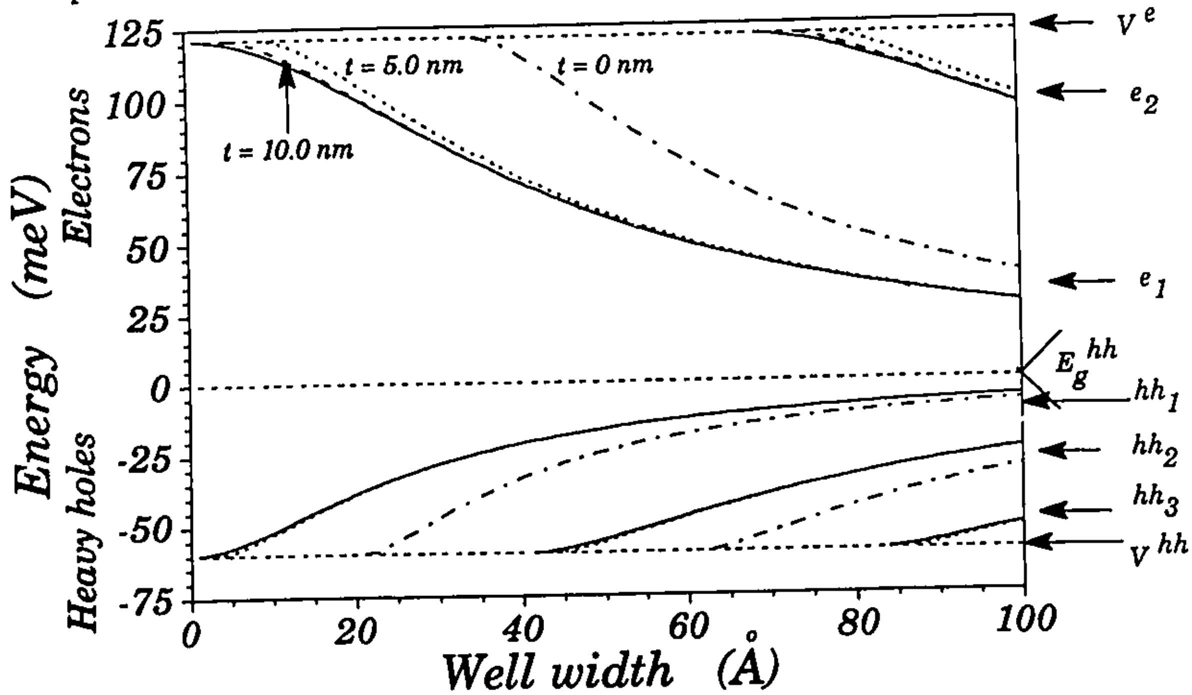

Fig. 1-4: Well width dependence of the bound states of a SQW as in fig. 1-3b for different values of cap thicknesses. For the electrons (top part) $V^e = 121$ meV, $m_w^* = m_b^* = 0.0665\ m_o$; for the heavy holes (bottom), $V^{hh} = 60$ meV, $m_w^* = 0.37\ m_o$ and $m_b^* = 0.41\ m_o$ (corresponding to an $In_{0.16}Ga_{0.84}As$/GaAs system at 4.2 K). The horizontal line at E = 0 represents the bottom of the wells (the electrons and the heavy holes are separated by the heavy hole band gap E_g^{hh}). The horizontal lines at the V's represent the onset of the continua. Two electron levels (e_1 and e_2) and three heavy hole levels (hh_1, hh_2, and hh_3) are shown by the curves, for 4 cap layer thicknesses: The solid line is for the regular SQW ("infinitely" large t), the -.-.-.-. line is for the semi-infinite QW (t = 0), the other two curves in between (often superposed to the solid line) are for t = 10.0 nm and t = 5.0 nm.

the semi-infinite QW (i.e. t = 0). The two lines in between are for t = 10.0 nm and t = 5.0 nm.

One notes first that for t $\gtrsim$ 10.0 nm, there is practically no deviation from the *regular* SQW results unless the well width is such that the highest bound level is just below the confining potential V. Indeed, because the wavefunction decays exponentially in the barrier of the *regular* SQW as $e^{-\gamma u}$ (where $\gamma = \left[\frac{2m_b^*}{\hbar^2}\ (|V|-\varepsilon)\right]^{1/2}$ and u is the distance from the well-barrier interface), the wavefunction dies off fairly quickly for typical values of $|V| - \varepsilon$ and m_b^* (ε is the energy measured from the bottom of the well). Therefore if t is larger than the "penetration depth", the wavefunction at the surface is zero anyway at a distance u = t away from the cap-well interface. One also notes that the shifts in the energy levels are smaller for the heavy holes because of their larger effective mass. For small t however, the shifts in the energy levels are quite significant and one could not neglect the influence of the finite-cap if such a device were to be built.

1-3-2 <u>Continuum states</u>:

For $E \geq 0$ (see fig. 1-3b) the Schrödinger equation allows a continuum of energy; but in order to understand the behavior of the carriers in these states, one has to construct the wavefunction in a similar manner as was done in the previous section for the bound states. Since in all regions $V(x) < E$, the solution of the Schrödinger equation in the various regions can be expressed in terms of sines and cosines. In region I, once again the infinitely high potential at $x = 0$ requires $\Phi_I(0) = 0$, so that $\Phi_I(x)$ is proportional to $\sin k_b x$, where $\dfrac{\hbar^2 k_b^2}{2m_b^*} = E$. And so:

$$\Phi_I \propto \sin k_b x \tag{1-8}$$

$$\Phi_{II} = A \sin k_w(x-t) + B \cos k_w(x-t), \qquad \frac{h^2k_w^2}{2m_w^*} = E + |V|$$

$$\Phi_{III} = C \sin k_b(x-(t+L)) + D \cos k_b(x-(t+L)).$$

The coefficients of eqs. (1-8) are found by matching the wavefunction and the current density at the interfaces, resulting in the following four equations:

$$\begin{aligned} A &= \xi \cos k_b t, \\ B &= \sin k_b t, \\ C &= \cos k_b t \cos k_w L - \frac{1}{\xi} \sin k_b t \sin k_w L, \\ D &= \xi \cos k_b t \sin k_w L + \sin k_b t \cos k_w L, \end{aligned} \tag{1-9}$$

here, $\xi = \dfrac{k_b m_w^*}{k_w m_b^*}$.

The probabilities of finding carriers with energy E in the various regions can be calculated using eqs. (1-8) and (1-9). Let us denote the unnormalized probability of finding carriers with energy E in the cap layer by

$$p_c = \int_0^t |\Phi_I(k_b(E),x)|^2 \, dx;$$

similarly the unnormalized probabilities for the well and the buffer regions are given respectively by

$$p_W = \int_t^{t+L} |\Phi_{II}(k_w(E),x)|^2 \, dx$$

(p_w is sometimes called the "*well occupancy*"), and

$$p_b = \int_{t+L}^{t+L+x_{max}} |\Phi_{III}(k_b(E),x)|^2 \, dx,$$

where x_{max} is the upper bound at which the integration is truncated. The truncation of the integral will not reduce the accuracy of the results if $x_{max} \gg t+L$. Since the buffer layer will be much thicker than the cap layer, the thickness of the buffer layer can be taken for the value of x_{max}. The substrate region (i.e. the material beneath the first-grown barrier) is not considered in the calculations because it is often doped or of poorer quality: hence, the coherence of the wavefunction will be lost after a short distance, and/or the different doping level can result in the presence of a barrier at the buffer/substrate interface. After integration:

$$p_c = \frac{t}{2}\left[1 - \frac{\sin 2k_b t}{2k_b t}\right] \tag{1-10a}$$

$$p_w = \frac{L}{2}\left[(A^2 + B^2) + (B^2 - A^2)\,\frac{\sin 2k_w L}{2k_w L} + 2AB\,\frac{\sin^2 k_w L}{k_w L}\right] \tag{1-10b}$$

$$p_b = \frac{x_{max}}{2}\left[(C^2 + D^2) + (D^2 - C^2)\,\frac{\sin 2k_b x_{max}}{2k_b x_{max}} + 2CD\,\frac{\sin^2 k_b x_{max}}{k_b x_{max}}\right]. \tag{1-10c}$$

The quantities of interest are the normalized probabilities of finding carriers of energy E in the various regions. These quantities are obtained by dividing the unnormalized probabilities by the total probability of finding carriers of energy E in the whole device, i.e. $p_t = p_c + p_w + p_b$. Thus, the normalized probabilities of finding the carriers in the respective regions are:

$$
\begin{aligned}
P_c &= p_c/p_t \\
P_w &= p_w/p_t \\
P_b &= p_b/p_t .
\end{aligned}
\tag{1-11}
$$

Another quantity of interest, which is associated with the density of states in the device induced by the presence of the well, is p_t/p_{box}, where p_{box} is the unnormalized probability of finding carriers with energy E in the corresponding box without the quantum well:

$$
p_{box} = \frac{x_{max}}{2}\left[1 - \frac{\sin 2k_b x_{max}}{2k_b x_{max}}\right] \tag{1-12}
$$

Calculations show that p_t/p_{box} behaves like the probabilities of finding the carriers in the various regions.

Of the three terms in eqs.(1-10b) and (1-10c), the first term is usually dominant because of the large denominators in the second and third terms (especially in eq.(1-10c)). Substituting the expressions of eqs. (1-9) into the first term of eq. (1-10c), one obtains:

$$C^2 + D^2 = \cos^2 k_wL + \sin^2 k_wL\,(1/\xi^2 \sin^2 k_bt + \xi^2 \cos k_bt) + 2\cos k_wL \sin k_wL \cos k_bt \sin k_bt\,(\xi - 1/\xi).$$

The well width L is usually relatively small compared to the cap layer thickness t, and so the above term oscillates with energy as k_bt changes, giving peaks of probability at certain energies in the various regions. When the energy $E \to 0$, $\xi \to 0$, and as E increases, $\xi \to 1$ and $C^2 + D^2 \to 1$, so that the oscillations of probability with energy disappear at higher energy; then, the system behaves classically. In this situation, the *classical probability* of finding carriers in any given region is given by the ratio of the width of the region to the total width of the device.

The best contrast† in the probabilities of eqs. (1-10b) or (1-10c) is obtained if k_wL is equal to an odd multiple of $\pi/2$ at an energy slightly above the barrier. For that energy, $\cos k_wL = 0$, $\sin k_wL = 1$; and for energies around this value, the unnormalized probability in the buffer region becomes

$$p_b \approx 1/\xi^2 \sin^2 k_bt + \xi^2 \cos^2 k_bt,$$

so that for small E, $\xi \to 0$ and p_b varies as $\sin^2 k_bt$, and

† *In analogy with optics, the contrast (or the visibility) of the oscillations can be defined as: (max - min)/(max + min); or simply: max/min. Where here, min and max are respectively the minima and maxima of the probabilities.*

consequently, it will oscillate with energy, having extrema (minima and maxima) at:

$$E_n = \frac{\pi^2 \hbar^2}{8 t^2 m_b^*} n^2 \qquad (1\text{-}13)$$

where n is an integer. If the buffer layer is thick (large x_{max}), p_b usually dominates p_t because of the x_{max} factor in eq. (1-10c). Therefore, carriers (which could have been photoexcited in the continuum with an energy E) will usually occupy the buffer region except at the energies around which p_b has a minimum, i.e. when $\sin^2 k_b t$ has a zero; then p_t is dominated by p_c, so that $P_c = p_c/p_t$ is close to unity, and then the probability to find the carriers in the cap increases. So that depending on the energy at which carriers are photoexcited in the continuum, they will tend to occupy preferentially a given region. This is illustrated in fig. 1-5 which shows the normalized probabilities of finding electrons in the cap (fig. 1-5a), in the well (fig. 1-5b) and in the buffer (fig. 1-5c) regions for a cap layer width of 50.0 nm, a buffer of 1.0 μm, for the system of fig. 1-4 (i.e. V^e = 121 meV, $m_w^* = m_b^* = 0.0665\ m_o$) with a well width of 3.5 nm. The dashed horizontal lines represent the values of the classical probabilities. In fig.1-5a one notes that P_c has sharp probability peaks, especially for small E, and outside these "resonance" peaks the probability goes back down close to zero, as explained above for the case $k_w L = \pi/2$ for small E. For example, the values for the first three maxima of

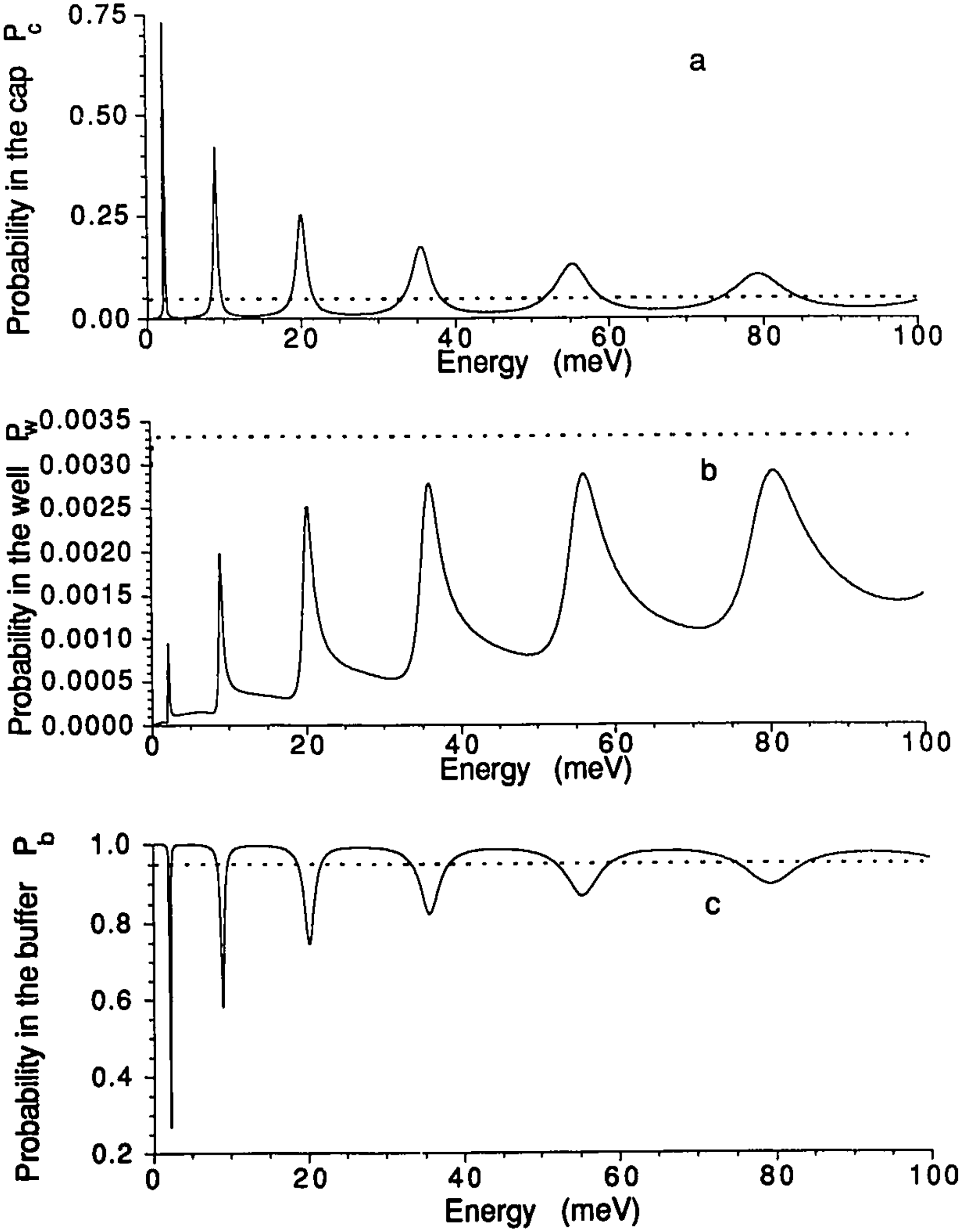

Fig. 1-5: Energy variations of the normalized probabilities of finding the electrons in the various regions of the SQW of fig. 1-3b, for a cap layer of 50.0 nm for the system of fig. 1-4 with a well width L = 3.5 nm. The buffer layer considered was 1.0 μm thick. The dashed horizontal lines are the classical probabilities. a) is for the cap layer region, b) is for the well and c) is for the buffer.

probability are: 73 %, 42 % and 26 %. That is, one has high probability that electrons will occupy the cap layer at some definite energies even though the cap is much thinner than the buffer. For the present situation, the classical probability to get carriers in the cap is 50.0 nm/ 1053.5 nm = 4.7 %. This is a remarkable energy segregation of the carriers amongst the various regions induced by the presence of the high potential at the surface.

Probability peaks similar to those of fig. 1-5a are also observed for the well region, see fig. 1-5b. The dimension of the well being small compared to those of the cap and buffer, the maximum values of probability in the well are smaller. As opposed to the situation for the cap, the envelope of the oscillation pattern decreases slowly on a smoothly increasing background to reach the value of the classical probability (3.5 nm / 1053.5 nm = 0.33 %) as E increases. Fig. 1-5c (the probability in the buffer) is approximately one minus the values of fig. 1-5a since the values for the probability in the well are small ($P_c + P_w + P_b = 1$). It merely illustrates that at the energies where the carriers are not in the cap, they occupy the buffer, except for the small fraction in the well, and therefore, carriers photocreated in a given region at these energies will redistribute accordingly.

As long as the thickness of the buffer layer is kept large compared to the size of the cap and well regions, the choice of the buffer layer size will only affect the values on the vertical axis of the graphs; indeed, for buffer layer sizes larger than a few times that of the cap layer, the shape of the oscillations is essentially independent of the buffer size. The ratio of the probabilities of finding the carriers in the various regions to the classical probabilities would be independent of the buffer size under these conditions. Oscillations in the probabilities of finding the carriers in the cap layer or oscillations in the well occupancy, such as those of fig. 1-5a or 1-5b for example, will be associated with the above-barrier oscillations observed in spectra of SQWs having such cap thicknesses and well widths. Experimental results obtained in modulated reflectivity are presented in sect. 3-3. Reflectivity experiments should be particularly sensitive to variations in the presences of carriers near the surface (cap and/or well) of the sample.

Considering the wavefunction for various values of energy, it is easy to visualize what is happening with the probabilities. Fig. 1-6 depicts the wavefunction of the electrons for the case studied above (fig. 1-5; well width 3.5 nm, cap layer is 50.0 nm, V^e = 121 meV, $m_w^* = m_b^*$ = 0.0665 m_o, and the wavefunction is independent of the buffer thickness assumed to be very large), for the first two resonant probability peaks of the cap (fig. 1-6a and 1-6b) , and for an off-resonance

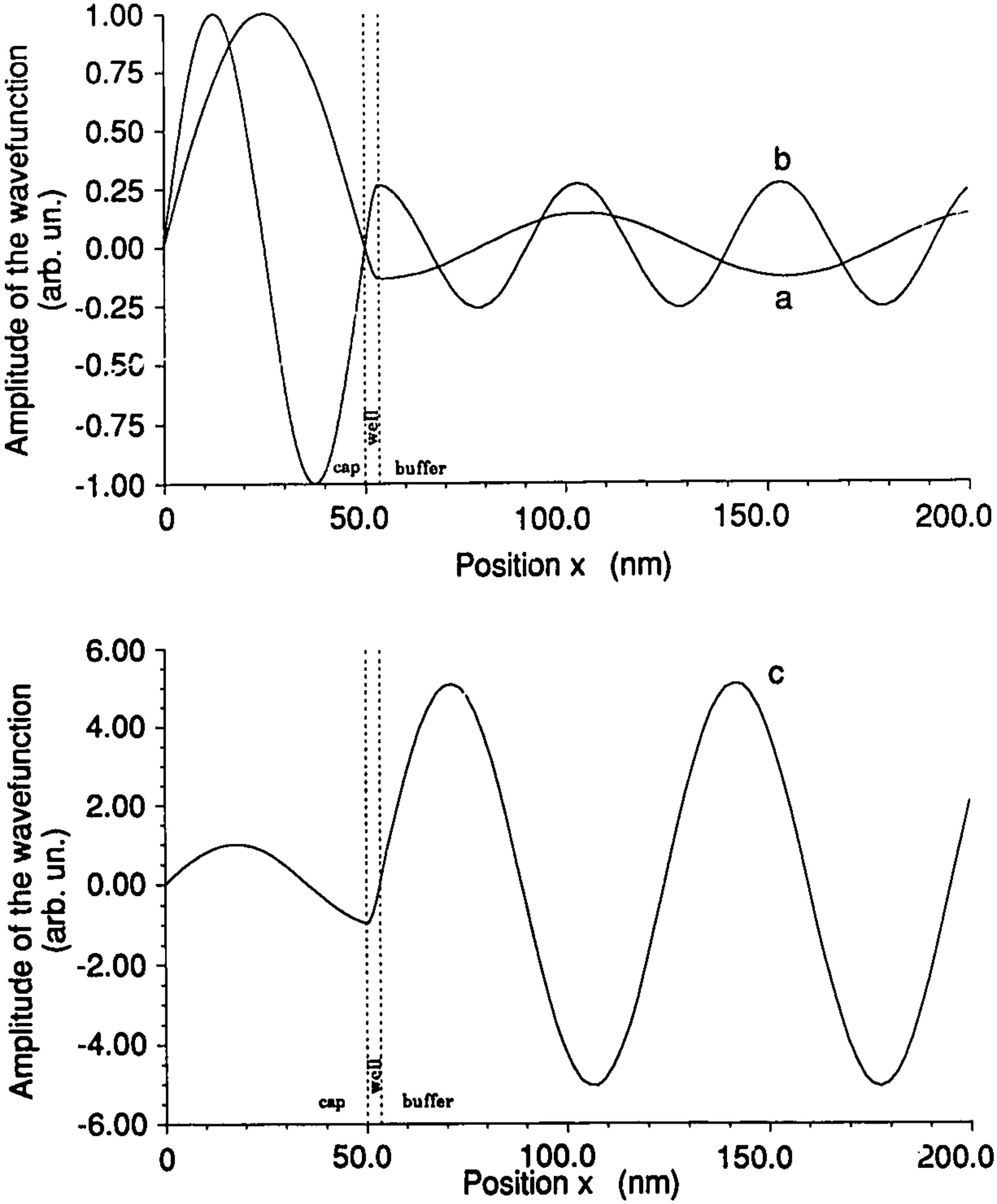

Fig. 1-6: Amplitude of the wavefunction throughout the device for the first two probability peaks in the cap layer and for an off-resonance situation for the example of fig. 1-5. a) is for the first peak at E = 2.25 meV, b) is for the second peak at 9.98 meV, and c) is for the off-resonance situation at E = 4.5 meV. The region between the two vertical dashed lines corresponds to the well of width L = 3.5 nm; to its left is the cap layer of thickness t = 50 .0 nm, and to its right the thick buffer.

situation, fig. 1-6c. The wavefunction for the first peak (at E = 2.25 meV; i.e. 2.25 meV above the continuum edge) has no node in the cap (x < 50.0 nm), whereas the wavefunction for the second peak (at E = 8.98 meV) has a node in the middle of the cap. The ratio of the amplitude of the wavefunction in the cap to the amplitude of the wavefunction in the buffer (x > 53.5 nm) is larger in the first "mode", giving a higher peak of probability in the cap. In the off-resonance case, fig. 1-6c for E = 4.5 meV, the wavefunction amplitude is much smaller in the cap than it is in the buffer.

The previous example satisfied the condition $k_w L = \pi/2$ for small E, in which case a good contrast in the probabilities is observed. Now to illustrate the case where $k_w L \lesssim \pi$ for small E (i.e. the case in which there would be a *resonant continuum state* for the *regular* SQW), one may calculate the probabilities for the heavy holes for the same type of well (i.e. L = 3.5 nm, t = 50.0 nm, buffer of 1.0 μm, and now V^{hh} = 60 meV, $m_w^* = 0.37\ m_o$, $m_b^* = 0.41\ m_o$). Indeed, the heavy holes in such a well satisfy the condition $k_w L \le \pi$ for small E. Results are shown in fig. 1-7 for the probability in the cap layer (fig. 1-7a) and in the well (fig. 1-7b). The probability for the buffer region is not shown, because it is easily deduced from fig. 1-7a, as explained in the previous example. Once again, probability peaks are observed, but the spacing between their extrema is decreased because of the larger effective mass of

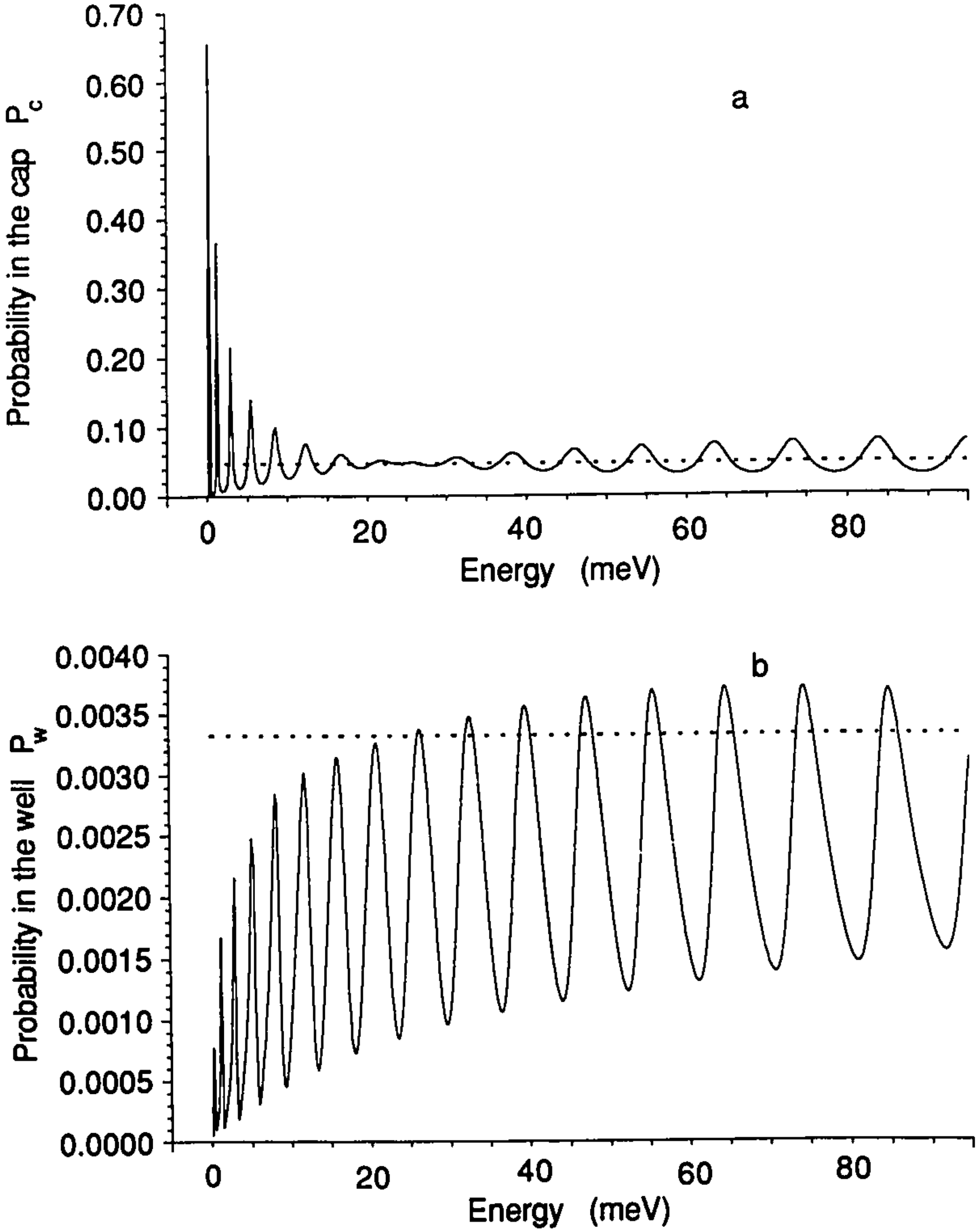

Fig. 1-7: Energy variations of the normalized probabilities of finding the heavy holes for the structure of fig. 1-5, for the cap a), and for the well b) regions. At E = 24 meV, $k_w L = \pi$.

the heavy holes (a larger m_b^* in eq. (1-13) decreases the spacing between the E_n). In fig. 1-7a for the cap layer, the first few peaks have probabilities much higher than the classical probability (65 %, 36 % and 21 % for the first three maxima as compared to 4.7 % for the classical probability). However, the contrast of probability is not as high as it was in the previous example, the probability minima having higher values here. The striking feature in fig. 1-7a is the node in the envelope pattern of the oscillations at around 24 meV. At this energy, $k_w L = \pi$, and the *regular* SQW would have a so-called resonant continuum state. This means that a particle incident on one side of the *regular* SQW has a probability of transmission to the other side equal to unity. Similarly, in the situation studied here, if the condition $k_w L$ is satisfied, the well forms an "*open channel*" for the carriers in the cap and buffer regions. Consequently, the classical values of probabilities are expected at this energy. Except for the smaller energy spacing between the peaks of the oscillations, the probabilities of finding the heavy holes in the well (fig. 1-7b) behave similarly to what was seen for the electrons (fig. 1-5b). Chapter 3 gives experimental evidence that for thinner cap layers, the contribution comes mainly from the heavy holes, whereas for a thicker cap layer the dominant contribution is from the electrons with their smaller effective mass.

Situations of good contrast of probability at low energy (as seen in fig. 1-5, first example), for the system of fig. 1-4, will be obtained for the heavy holes at $L \approx 2.0$ nm, 6.2 nm, 10.3 nm, etc (i.e. $k_w L = \pi/2$, $3\pi/2$, $5\pi/2$ respectively). For the electrons, good contrast is obtained for $L \approx 3.4$ nm, 10.2 nm, etc (i.e. $k_w L = \pi/2$ and $3\pi/2$). For larger well widths however, the argument $k_w L$ changes more rapidly with energy, reducing the energy range in which good contrasts are observed. A situation of *open channel* or *resonant continuum states* as seen in fig. 1-7 (second example), will be observed if the well width is slightly smaller than the width at which a new bound state appears (i.e. the usual condition to get the *resonant continuum state* in the *regular* SQW)

The depth of the potential well will influence the way in which ξ reaches unity as E increases. For a shallower potential, ξ is closer to unity for a given energy, and the system behaves more classically (as expected for a shallow potential), giving less probability contrast. The spacing between the extrema of probability is determined mainly by $\sin^2(k_b t)$ which has its extrema given by eq. (1-13). Consequently, if the product of the square root of the carrier effective mass and the cap thickness is large, the energy difference between two consecutive extrema of probability becomes small, approaching classical behavior in the limit of "high quantum numbers".

This section predicted shifts in the bound states for cap layer thinner than about 10 nm, and interesting oscillatory behavior of the continuum states for cap thicknesses as large as 100 nm, in the flat-band conditions (i.e. zero-field). Next section will focus on these oscillatory behaviors of the continuum states when an uniform electric field is applied to the structure.

1.4 Presence of a uniform electric field.

It was shown in sect. 1-3-1 that the bound states of a SQW would not be significantly affected by the surface potential if the cap layer is larger than about 10 nm. The study of the effect of an electric field on the bound states of SQW with such small cap layer certainly has an interest of its own. But for clarity, the theory related to that problem will not be developed here, since the thinnest cap layer studied experimentally was 50 nm thick. The effects of the electric field on the bound states of the samples studied could therefore be interpreted with the well-known Stark effect as mentioned in sect. 1-2.

In this section, the emphasis will be given on the continuum states in the potential depicted in fig. 1-8. An electric field (F) is applied to the SQW potential of fig. 1-3b; the polarity of the field is chosen such that the potential away

Fig. 1-8: Band diagram of a SQW with a capping barrier layer of finite size (as shown in fig. 1-3), when an applied electric field lowers the potential away from the surface. E_{edge} is the edge of the energy continuum.

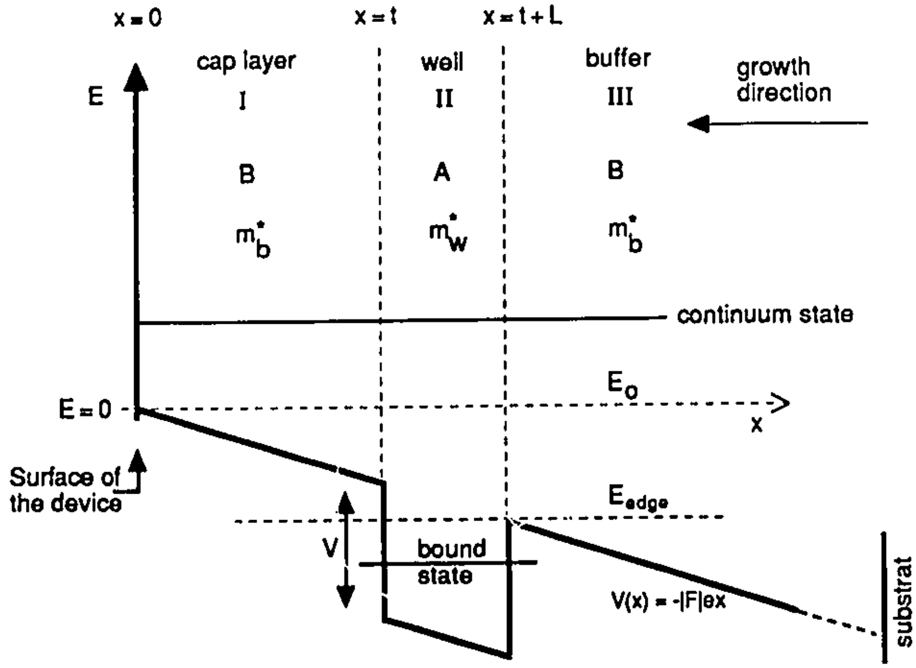

from the surface is lowered. The problem with the opposite field polarity reduces to that of a quantum well in a triangular potential (formed by the slope of the applied potential and the vertical potential at the surface). Trzeciakowski and al[TG91] have studied similar problems, but only in the case of barriers of quasi-infinite spatial extent. Trial calculations (results not shown here) taking into account the finite-size of the cap layer, for that polarity showed that the continuum states of the square quantum well becomes discrete, and are essentially the bound states of the corresponding triangular well. For small energies over the square well however, these bound states are displaced in energy depending on the depth and width of the well, the cap layer thickness, and the magnitude of the field. This problem will not be studied in details here, and for the remainder of this section, the continuum states of the potential of fig. 1-8 will be analyzed. Explicitly the potential is

$$V(x) = -|F|ex \qquad \text{for } x < t \text{ or } x > t + L,$$
$$\qquad -|F|ex - |V| \qquad \text{for } t \le x \le t + L.$$

The zero-energy line, $E = 0$, is as illustrated in fig. 1-8. After the proper substitutions, the Schrödinger equation with the above potential reduces to the Airy equation $\Phi''(u) - u\,\Phi(u) = 0$, with the Airy functions for solutions[AS64] in the various regions:

$$\Phi_{I}\ (x) = \Phi_{cap}[z(x)] = \alpha_1 \text{ Ai } [z(x)] + \beta_1 \text{ Bi } [z(x)], \qquad (1\text{-}14)$$
$$\Phi_{II}\ (x) = \Phi_{well}[\zeta(x)] = \alpha_2 \text{ Ai } [\zeta(x)] + \beta_2 \text{ Bi } [\zeta(x)],$$
$$\Phi_{III}(x) = \Phi_{buffer}[z(x)] = \alpha_3 \text{ Ai } [z(x)] + \beta_3 \text{ Bi } [z(x)],$$

where $z(x) = -x\ (2m_b^*|F|e/\hbar^2)^{1/3}\ [1 + E/(|F|ex)]$,
and $\zeta(x) = -x\ (2m_w^*|F|e/\hbar^2)^{1/3}\ [1 + (E + |V|)/(|F|ex)]$.

As before, the cap wavefunction must vanish at $x = 0$, and so α_1 and β_1 in eq. (1-14) may be chosen to obtain:

$$\Phi_{cap} \propto \text{Bi } [z(0)] \text{ Ai } [z(x)] - \text{Ai } [z(0)] \text{ Bi } [z(x)]. \qquad (1\text{-}15)$$

Furthermore, going through the procedure of sect. 1-3-2, one would obtain α_2, β_2, and α_3, β_3 of eq.(1-14), and the probabilities of finding the carriers in the various regions. The algebra is similar, except that the integrals involve Airy functions instead of sines and cosines:

$$\alpha_2 = \Pi\Big((Bi[z(0)]\ Ai[z(t)] - Ai[z(0)]\ Bi[z(t)]) \times Bi'[\xi(t)] - (m_w^*/m_b^*)^{2/3}\ (Bi[z(0)]\ Ai'[z(t)] - Ai[z(0)]\ Bi'[z(t)]) \times Bi[\xi(t)]\Big)$$

$$\beta_2 = \Pi\Big(-(Bi[z(0)]\ Ai[z(t)] - Ai[z(0)]\ Bi[z(t)]) \times Ai'[\xi(t)] + (m_w^*/m_b^*)^{2/3}\ (Bi[z(0)]\ Ai'[z(t)] - Ai[z(0)]\ Bi'[z(t)]) \times Ai[\xi(t)]\Big)$$

$$\alpha_3 = \Pi\Big((\alpha_2\ Ai[\xi(t+L)] + \beta_2\ Bi[\xi(t+L)]) \times Bi'[z(t+L)] - (m_b^*/m_w^*)^{2/3}\ (\alpha_2\ Ai'[\xi(t+L)] + \beta_2\ Bi'[\xi(t+L)]) \times Bi[z(t+L)]\Big)$$

$$\beta_3 = \Pi\Big(-(\alpha_2\ Ai[\xi(t+L)] + \beta_2\ Bi[\xi(t+L)]) \times Ai'[z(t+L)] - (m_b^*/m_w^*)^{2/3}\ (\alpha_2\ Ai'[\xi(t+L)] + \beta_2\ Bi'[\xi(t+L)]) \times Ai[z(t+L)]\Big)$$

(1-16)

After integration of the probability density ($|\Phi(x)|^2$), the unnormalized probabilities for the various regions are obtained by substituting the appropriate limits into the following integrated expression:

$$p_c = \left(z(x)\ \Phi_I^2\ [z(x)] - (\Phi_I'[z(x)])^2 \right) \Big|_{x=0}^{x=t}$$

$$p_w = (m_b^*/m_w^*)^{1/3} \left(\xi(x)\ \Phi_{II}^2[\xi(x)] - (\Phi_{II}'[\xi(x)])^2 \right) \Big|_{x=t}^{x=t+L}$$

$$p_b = \left(z(x)\ \Phi_{III}^2[z(x)] - (\Phi_{III}'[z(x)])^2 \right) \Big|_{x=t+L}^{x=x_{max}} \qquad (1\text{-}17)$$

Where the primes denote the derivative of the Airy functions with respect to their argument (the extra factors coming from the change of variables have been taken into account by the factor in front of p_w). The normalized probabilities are found from eq. (1-11).

To illustrate the influence of an applied electric field on the probabilities of finding the carriers in the various regions, calculations were performed for the SQW structure of the previous example (i.e.: t = 5.0 nm, L = 3.5 nm, and a buffer of 1.0 μm; V for the heavy holes is 60 meV; the zero-field results were in fig. 1-7). Results in fig. 1-9 show the evolution of the probabilities as the applied field F is changed, curve i to xi are the normalized probabilities of finding the heavy holes in the cap layer (fig. 1-9a), and in the well (fig. 1-9b) for electric field values between 0.0 to 10.0 KV/cm, in steps of 1.0 KV/cm. The horizontal axis

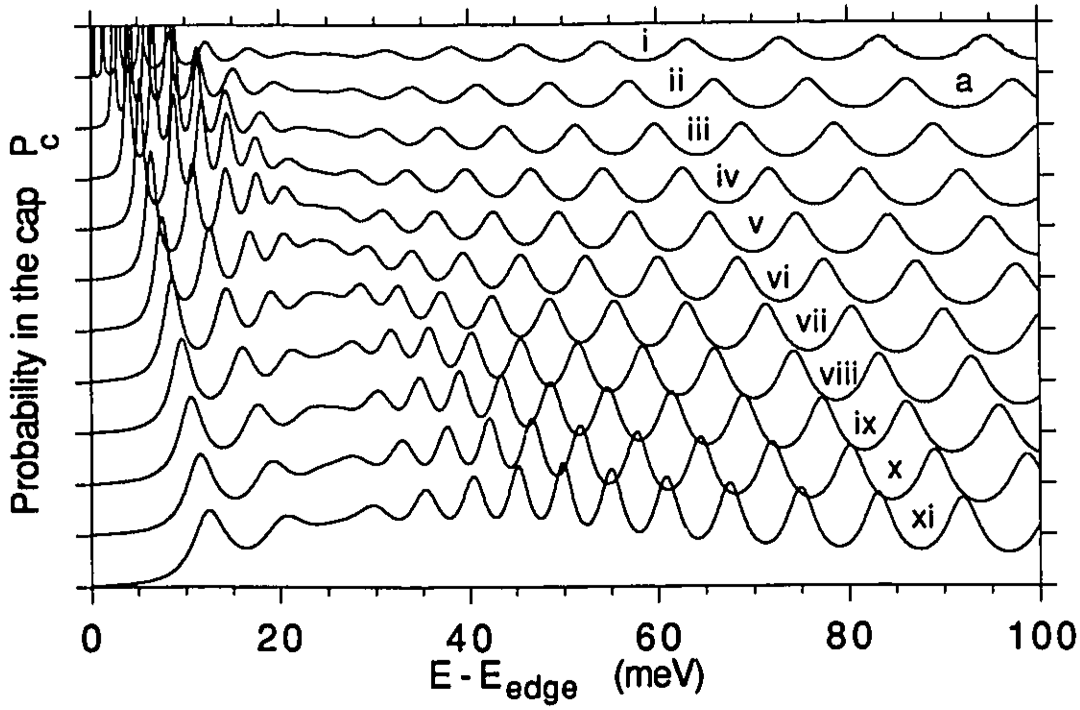

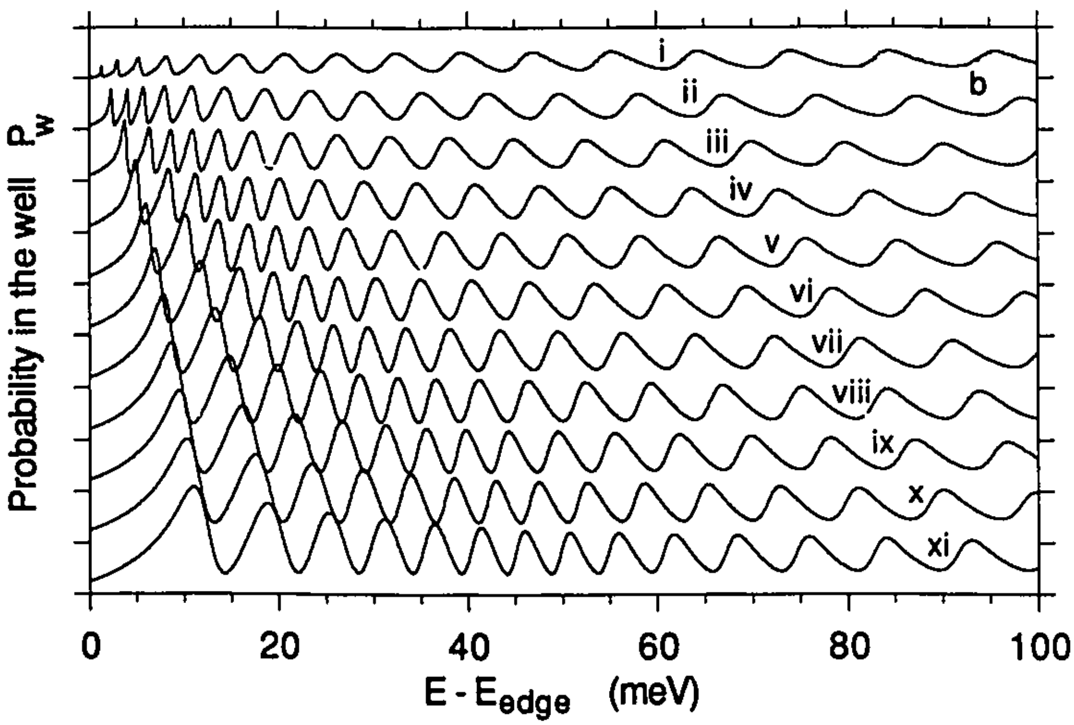

Fig. 1-9: Normalized probabilities of finding the heavy holes in the cap layer a), and in the well b), for a SQW like the one of fig. 1-7, for applied electric field from 0 KV/cm to 10 KV/cm in steps of 1.0 KV/cm corresponding to curves i to xi.

represents the energy measured from the lower edge of the well (see fig. 1-8). The probabilities oscillate with the energy as expected from the flat band results of previous section. It is now possible to follow the extrema of the oscillations as the electric field is varied. They are found to shift monotonically to higher energies as the electric field is increased. Similar shifts will be observed experimentally at various field in the Electroreflectance spectra which will be presented in sect. 3-3-2.

To gain more knowledge on these shifts, fig. 1-10 compares the 0 KV/cm (curve i) and the 5.0 KV/cm (curve vi) spectra of fig. 1-9b. Curve vi of fig. 1-10 was shifted in energy to show that the peaks at positive energies (those to the right of the vertical dashed line, labelled from 7 to 15) correspond to those of the zero-field situation; that is, the spacing between the peaks is preserved, but their positions are shifted in energy with the applied electric field. There are two contributions to that shift: the edge of the well is moved down in energy with increasing electric field, displacing the peaks upward by the same amount (here +5.35 meV/(KV/cm)), and also numerical analysis shows that the peaks are shifted down because now eq. (1-15) has to be used instead of eqs. (1-8). For the present example, the latter shift is found to be -2.49 meV/(KV/cm) from fig. 1-10, giving a net shift of +2.86 meV/(KV/cm). For $E \geq 0$, the vertical potential limits the left

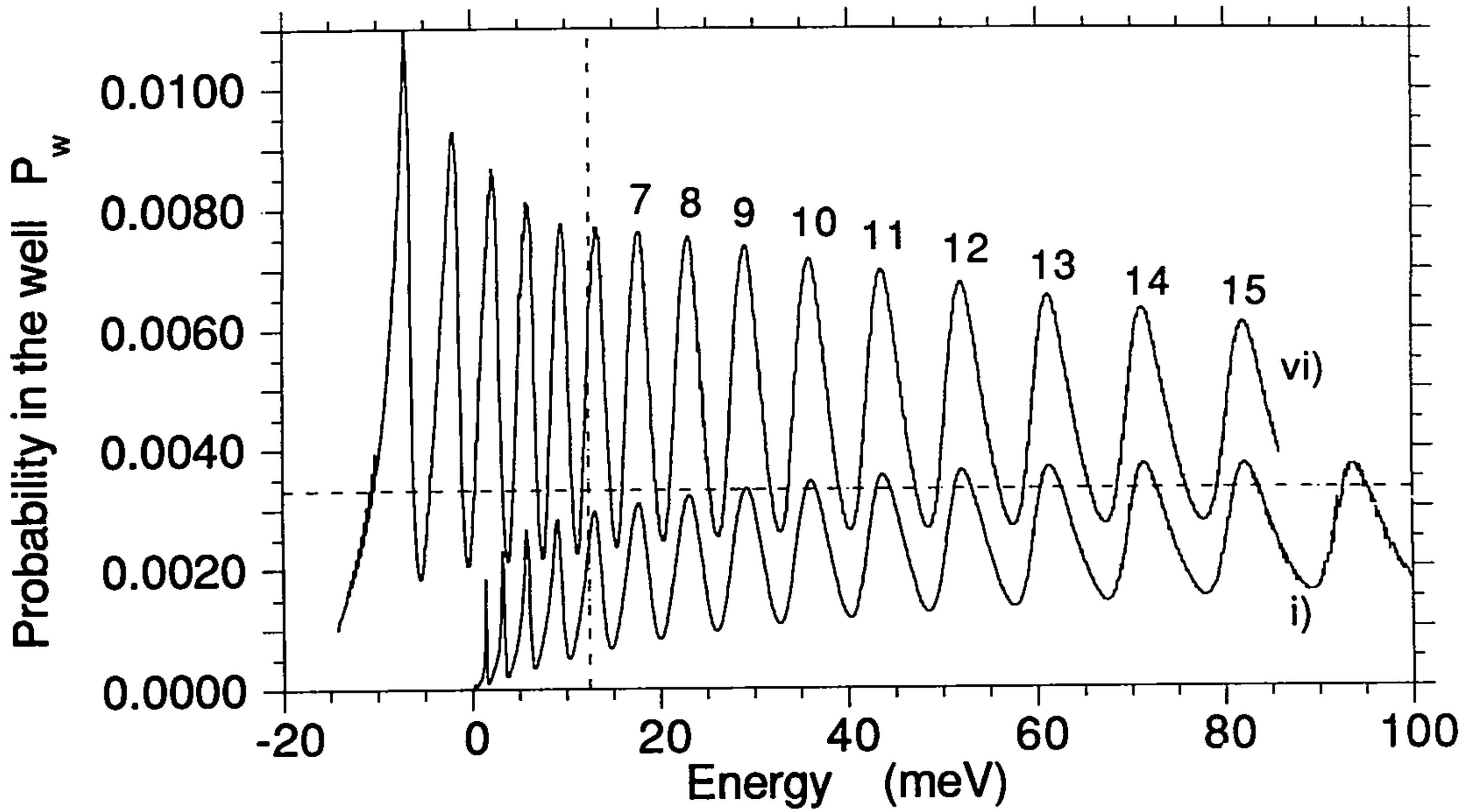

Fig. 1-10: Comparison between curve i (0 KV/cm) and vi (5.0 KV/cm) of fig. 1-9. Curve vi has been shifted in energy to align the peaks which were labelled from 7 to 15. The horizontal dashed line is the classical probability of finding the carriers in the well, and the vertical dashed line indicates the position of the E_o line for curve vi, as illustrated in fig. 1-8.

of the SQW band diagram in fig. 1-8, and this is why the peaks in probability for these energies are very similar to those found for the zero-field situation: the separation between the extrema increases as the energy is increased. However for E < 0, the left of the band diagram in fig. 1-8 is limited by the tilted linear potential (caused by the applied electric field), and then the spacing between the extrema of the oscillations in the probabilities diminishes as the energy is increased, as can be seen in fig. 1-10 curve vi, to the left of the vertical dashed line. Another remarkable feature induced by the applied electric field is the overall increase in the probability of finding the carriers in the well region at small energies. The zero-field probabilities of finding the carriers above the well were smaller than the classical probability (horizontal dashed line), but as shown in fig. 1-10 for 5.0 KV/cm, for example, the probabilities of finding the carriers in the well region for small energies are on average higher than the classical probability.

Chapter 1 has established the theoretical background necessary for the interpretation of the experimental results. Before the presentations of these results, the experimental techniques (from the sample preparation to the various spectroscopic techniques) used to obtained the results will be described in chapter 2.

CHAPTER 2

EXPERIMENTAL TECHNIQUES

2-1 Sample growth and preparation........................ 49

2-2 Photoluminescence (PL).............................. 53

2-3 Photoreflectance (PR) and Electroreflectance (ER).... 60

2-4 Photovoltage (PV) and Electroluminescence (EL)....... 68

This chapter details the samples studied, and the experimental techniques. Photoluminescence permits a quick determination of the energy of the ground state levels, and of the quality of the samples. It is therefore useful for a preliminary characterization. Photoreflectance, electroreflectance, or photovoltaïc effect will allow us to obtain more information about the intermediate levels in the QW structures. Electroreflectance is particularly adequate to quantitatively study the effects of the applied electric field. Because modulated reflectivity measurements are potentially more sensitive to the oscillations in the density of carriers near the surface than transmission or other possible type of modulation techniques, photoreflectance and electroreflectance will be used to observed the cap-related above-barrier oscillations described in chapter 1. Moreover, reflectivity spectroscopy is easily performed in contrast to other techniques such as transmission which may require etching of the substrate, especially at above-gap energies. Electroluminescence is a technologically interesting alternative to photoluminescence, the carriers being excited electrically instead of optically.

2-1 Sample growth and preparation:

In this work, the semiconductors used to construct the quantum wells are $In_xGa_{1-x}As$ for the adjustable low bandgap material, and GaAs for the barrier. The lattice mismatched between InGaAs and GaAs restricts the choice of the alloy concentration to X < ~0.25. For values of X larger than 0.25, dislocation in the crystalline structure may occur, relaxing the strain in the layers. To avoid relaxations of that lattice-mismatched induced strain, it is also necessary to keep the total thickness of the strain layers smaller than a critical thickness[BH90]. In practice, this will not impose any restriction on the thicknesses of SQW for the range of X mentioned above. Choosing a particular X value, and taking into consideration the strain induced shift in the InGaAs energy gap for that value, it is then possible (using the theoretical background of chapter 1) to predict the interband transitions of the SQW as a function of the well width as illustrated in fig. 1-2 or 1-4. Custom designed samples with the desired well width and composition are then grown by Metal-Organic Vapour Phase Epitaxy (MOVPE) on commercially-available GaAs substrates (fig. 2-1a). The substrate are oriented in the (100) direction, and Si doped to $n \simeq 1 \times 10^{18}$ cm^{-3} giving good electrical conductivity even at low temperatures. Fig. 2-1b sketches an undoped GaAs buffer layer grown by MOVPE on top of the above substrate. The epitaxy was done at the Institute for Microstructural Sciences at the National Reasearch Council of Canada (NRCC) by Dr. A.P. Roth and his group. The epitaxial material has a typical residual n-doping concentration in the range of 10^{14} cm^{-3}. More details on the growth technique are given elsewhere[RM87]. In the sequential study, buffers with thicknesses 0.5 and 2.0 μm were investigated order to test the relative response of the underlying substrate as the buffer thickness is changed. Fig. 2-1c represents (not to scale) the complete SQW having a buffer layer of thickness x_{max} and a cap layer of thickness t. The buffer and cap layers of the complete SQW sample are of the same nature as the buffer layer of fig. 2-1b, and they are grown on a substrate as in fig. 2-1a. Well widths between L = 2.0 and L = 12.0 nm have been grown. For convenience, the band diagram of the complete SQW is shown in fig. 2-1d where the labels bear their usual meaning: V^e and V^{hh} are the confining potentials for the electrons and heavy-holes respectively, e_i and hh_j are the energy levels (measured from the bottom of the well unless otherwise specified) for the confined electrons

Fig. 2-1: Component layers of a SQW to be studied sequentially:

a) Si-doped GaAs substrate,

b) undoped GaAs buffer, MOVPE grown on the substrate of a),

c) complete SQW,

d) corresponding band diagram.

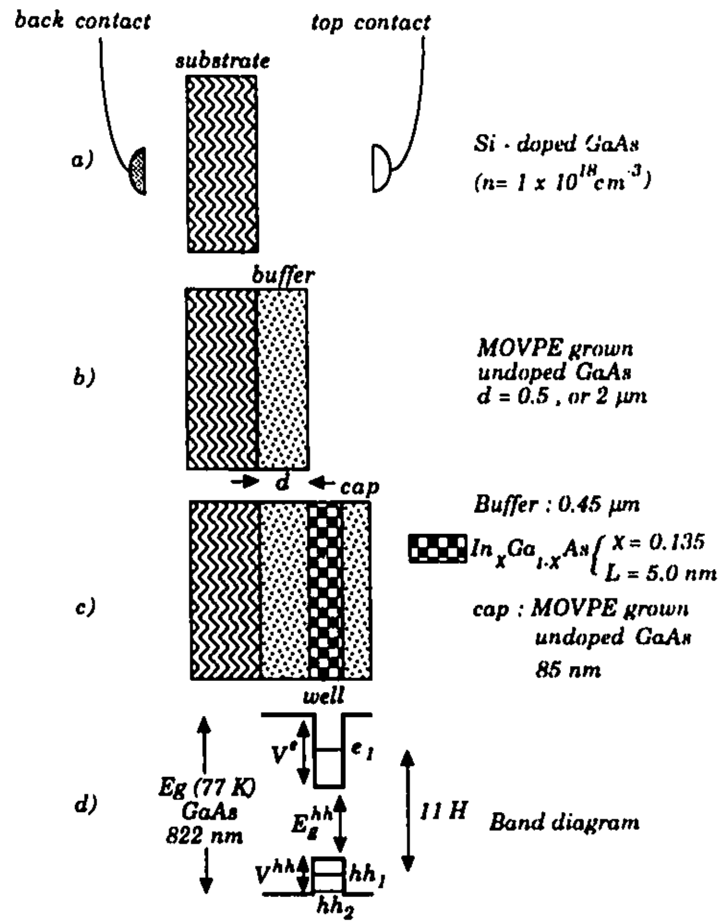

and heavy-holes respectively, ij H denotes the transition from the ith electron level to the jth heavy-hole level, E_g^{hh} is the strained heavy-hole band gap and E_g^{lh} would be the strained light hole band gap. E_g^{lh} is not shown here because it would be below the valence band of GaAs as explained in sect. 1-1.

For ER, EL, or PV, electrical contacts are needed to apply an electric field, or to create a built-in field to separate the photocreated carriers. To that effect, a semi-transparent gold thin film, a few mm^2 in area, could be evaporated (using

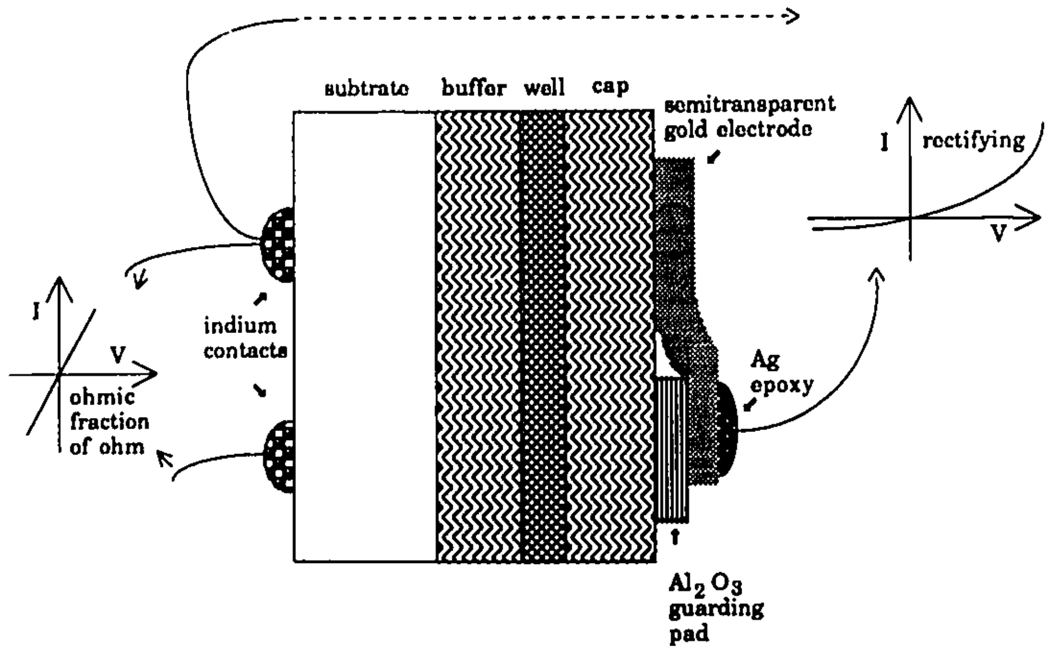

Fig. 2-2: SQW sample with electrical contacts.

a cryopumped evaporator) on the front surface of the sub strate, buffer, or complete SQW samples. Fig. 2-2 illustrates a complete SQW sample with such a gold barrier, with an Al_2O_3 guarding pad, and with indium contacts in the back of the sample. The guarding pad was evaporated before the deposition of the gold electrode to protect against short circuit near the position where the signal leads are bound with a thermally activated, electrically conducting epoxy. The ohmic contacts were formed on the (n-type) substrate by heating a small piece of indium at 300 ^{o}C for few minutes in an inert atmosphere. Ohmicity was always checked between the two indium contacts by tracing an I-V curve, whereas an I-V curve between the indium and the gold contacts would display typical diode-like rectification. The experiments described in this work have used the above type of Schottky configuration (i.e. a barrier on top, and an ohmic contact on the substrate layer in the back).

The component layers could be analyzed individually by performing experiments on the sequence shown in fig. 2-1, or series of complete SQW samples with different parameters could be studied, by using the various techniques described in the following sections.

2-2 Photoluminescence (PL):

Photoluminescence is the radiative process by which a material (bulk semiconductor, or QW structure in our case) emits a photons after recombinations of thermallized photo-created electron-hole pairs, or excitons. Consequently, PL and the techniques based on PL such as Time-Resolved PL, or PL Excitation, provide us with powerful tools for a quick characterization of the energy levels and an assessment of the quality of the samples studied, or for a detailed analysis of the dynamics of the carriers. The energy-spread in the width of the spectral lineshape will indicate the quality of the samples. For example, fluctuation in the alloy composition or the width of the well of a QW structure, would broaden the PL peak. In this work, only CW (continuous; i.e. not Time-

Resolved) PL will be used ,except for the results presented in fig. 3-6 and 3-7 which were obtained with a pulsed laser so that high intensity of excitation could be used without damaging or heating the samples. In that case, a boxcar integrator was used to measure the amplitude of the signal.

PL has the advantage that it does not necessitate any additional sample preparation since it does not need any electrical contact (if transparent electrical contacts are present, it is then possible to measure the PL as a function of the applied electric field as described in sect. 3-3). However, the results can be dependent on the choice of the wavelength of excitation. Indeed, the absorption coefficient of the semiconductor varies rapidly above the energy gap (~ 60 cm^{-1}/meV), consequently the penetration depth of the exciting beam of light will depend on the energy of the probing photons. To illustrate this effect, fig. 2-3 shows the transmission profile using Beer's law ($I_T/I_o = e^{-\alpha x}$) for values of α between 1×10^4 cm^{-1} to 1×10^5 cm^{-1}, for x between 0 and 1000 nm. For instance, for a probing wavelength in GaAs at 125 meV above the gap ($\lambda \approx 800$ nm at room temperature), $\alpha = 1.4\times10^4$ cm^{-1} *P85*; and at 650 meV above the gap ($\lambda \approx 600$ nm at room temperature), $\alpha = 4.7\times10^4$ cm^{-1}, corresponding approximately to curve i and v in fig. 2-3. The choice of the type of laser used to excite the PL, will determine the wavelength of excitation (λ_{ex}). Different wavelength of

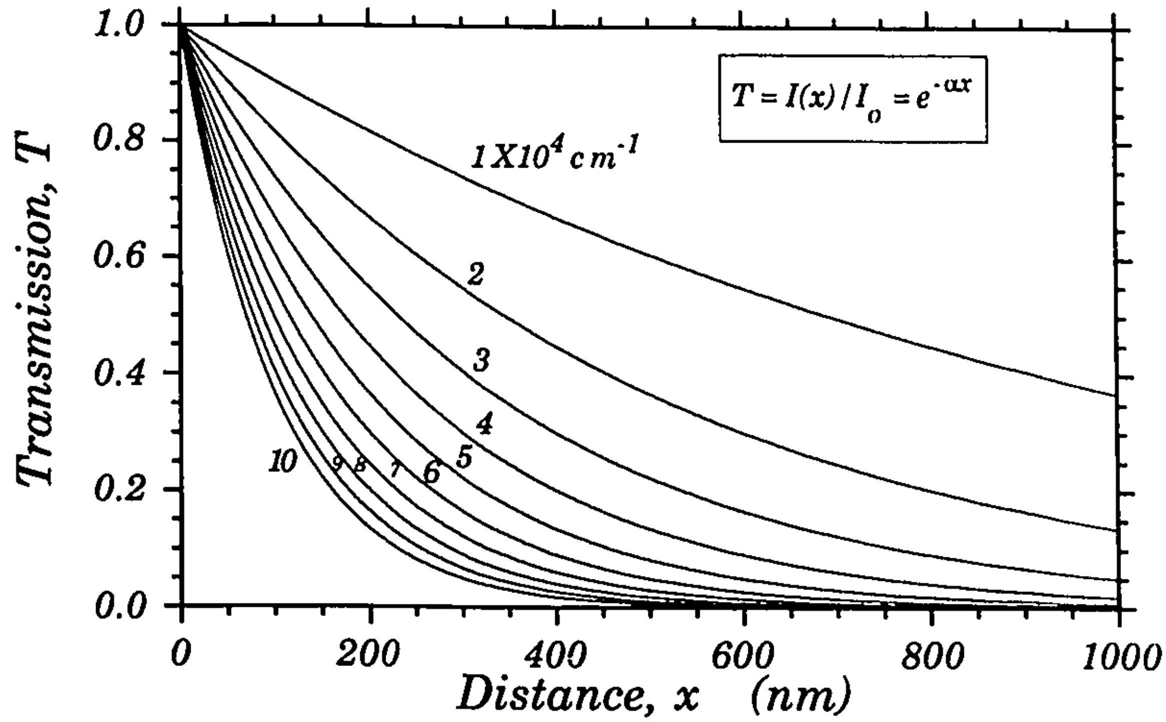

Fig. 2-3: Transmission profile in a (semiconductor) material for absorption coefficient values between 1 X 10^4cm^{-1}and 1 X 10^5cm^{-1}.

excitation will correspond to different absorption coefficient $\alpha(\lambda_{ex})$; and depending on $\alpha(\lambda_{ex})$, a significant fraction of the intensity of the probing beam reaches the underlying layers (such as the substrate in a quantum well sample). Part of the optical response obtained may then originate from these layers. Hence, a judicious choice of the excitation wavelength, or a sequential study as the one performed in chapter 3 may be necessary.

The experimental set-up for PL is shown schematically in fig. 2-4. The sample is placed in an optical cryostat which

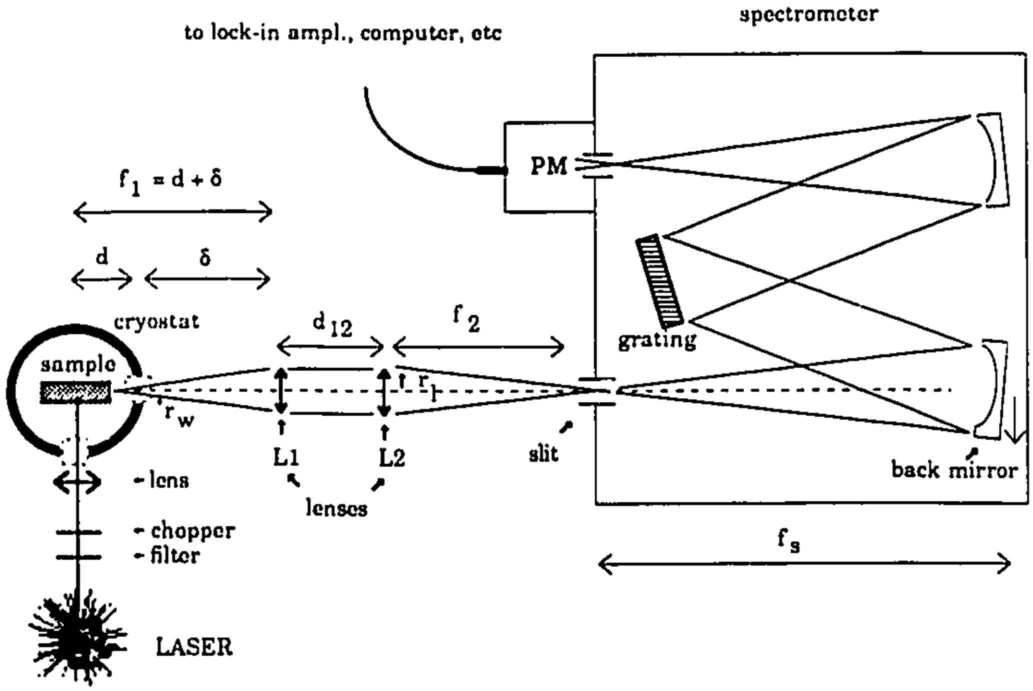

Fig. 2.4: Experimental set-up for PL experiments using two lenses to collect the emitted photons.

keeps its temperature constant, and is excited with a filtered laser beam at a wavelength λ, with a power P, focused on an area A, giving an exciting intensity I_{ex} = P/A. The laser light scattered from the sample it filtered-out, and the emitted PL is collected and passed through a spectrometer. The dispersed PL is then detected with an appropriate photomultiplier (PM) using standard synchronous methods. The signal is then digitized, stored, and analyzed with a computer. The typical apparatus consisted of: an optical liquid nitrogen cryostat (custom designed for routine measurements at T=77 K), or an optical liquid helium cryostat (for measurements between T ~ 1.8 K and T = 295 K); a CW Argon ion laser at λ_{ex}= 488 nm or 514.5 nm, or an HeNe laser at 632.8 nm, with the appropriate Fabry-Perot interference filter, or a prism, to isolate the laser line; a 1.0 m spectrometer equipped with a 1200 grooves/mm grating giving a dispersion of 0.8 nm/mm; and GaAs or InGaAs Hamamatsu PM detecting up to λ=1.0 μm, or in certain cases, a Si-detector which could be placed directly at the exit window of the cryostat if the spectral dependence of the PL needed not to be studied. The sample in the liquid nitrogen cryostat was mounted on a cold finger in thermal contact with the liquid; and the sample in the liquid helium cryostat could be immersed in superfluid pumped helium for measurements below the lambda point, or placed in a controllable flux of cold helium vapor for the higher temperature.

The efficiency of the detection will be very much affected by our ability to collect the PL emitted from the sample. The preferred method to collect the PL consists of two biconvex lenses (L1 and L2) positioned to optimized the signal reaching the PM as sketched in fig. 2-4. The formalism involved in the optimization of the PL collected is elementary, but leads to useful considerations, the lack of which could severely deteriorate the quality of the experimental results. To that effect, Appendix 1 gives a description on how to optimize the optics of such a two lenses system in order to maximize the amount of light collected in PL experiments. Other system, such as mirrors, can be used to collect the PL; they can be optimized using considerations similar to that of Appendix 1, or Appendix 2 which describes how to optimize the efficiency of a single mirror system in the case of a white light source with a monochromator. Furthermore, the angle at which the probing beam hits the sample may influence the PL spectra. For example for QW structures the direction of the propagation of the light and its polarization will influence the selection rules†. The angle at which the PL is collected will also influence the amount of light collected. Fig. 2-5 illustrates a laser beam hitting the sample at near normal incidence, and the PL being collected along the sample width. Semiconductor materials like GaAs have relatively high indices of refraction. Consequently, a large fraction of the probing beam will be reflected at the surface. For example at room temperature, light at λ=632.8 entering GaAs at normal incidence, with n=3.86 and k=0.20, will be reflected with R=35%. And part of the PL, at λ = 920 nm for example, trying to exit the crystal, with n = 3.6, will be reflected internally. At normal incidence R = 32%, but a large fraction of the PL (at a wavelength at which the sample is transmitting light) created beneath the surface may get trapped within the sample since the critical angle for total internal reflection will be small for such a

† *W87, p.52.;KS90*

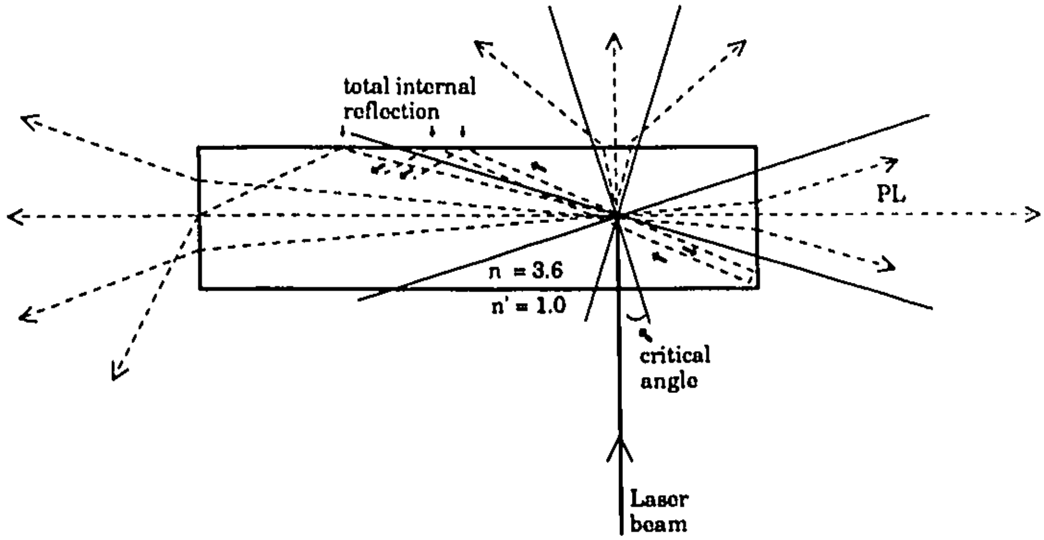

Fig. 2-5: Total internal reflection and critical angle in a semiconductor slab, with n = 3.6 ($\theta_c = 16^o$), in PL experiments.

high index of refraction; $\theta_c = \sin^{-1}(1/n) \approx 16^o$, as illustrated in fig. 2-5. This is why the choice of the angle at which the PL is collected will have a significant influence on the efficiency of the detection. Collecting the PL perpendicularly to one of the surfaces of the sample (i.e. from the edge or from the face) will optimize the amount of PL reaching the detection system. Collecting the PL from the edge is easier experimentally, and will have the additional advantage that if the material is transmitting well at the wavelength of emission, the sample may form a waveguide for the PL into the collecting system.

Even tough CW PL is a quick and very useful method for characterization of the sample, by its nature, it favors the transition having the lowest energy (11H transition for the QWs). Information about the higher lying energy levels is usually necessary for a complete characterization. Such information can be obtained by doing other type of experiments such as the Photoluminescence Excitation (which is experimentally more complex), or alternatively PR, ER or PV which are described in the next two sections.

2-3 Photoreflectance (PR) and Electroreflectance (ER):

Modulation spectroscopy is recognized has a powerful tool to study interband transitions in bulk semiconductors or intersubband transitions in quantum well heterostructures†. This section will describe the major two techniques, used here to modulate the reflectivity of our samples. In PR a secondary chopped beam of photons modulates the carrier concentration and/or the surface electric field (which modulate the dielectric constants) of the sample while a probing beam of DC monochromatic light is scanned. Together with a large DC component, the light reflected from the sample will contain a modulated component. The amplitude of the modulated component depends on the energy of the probing beam relative to the energy levels of the sample. As was the case for PL, contactless samples can be studied by PR. In ER the modulation is

† *A80, P91, RJ89, P88, RJ87, JD89, KS90, PG88, PC90*

achieved by applying an alternating voltage (which modulates the electric field) across the sample, through a semitransparent Schottky barrier (as described above in sect.i). There exists methods other than the Schottky configuration to apply the voltage in ER, such as immersing the sample into an electrolytic solution, but this method is obviously not suitable at low temperatures where most of the interesting data are obtained. While the small alternating voltage modulates the electric field, a bias DC voltage may also be applied to analyzed the properties of the sample at various values of the electric field. Therefore, PR has the advantage that it does not necessitate electrical contacts, whereas ER can be used to quantitatively control the electric field applied to the sample. PR or ER experiments on quantum well structures give spectra with typical derivative lineshapes associated to the intermediate transitions (such as 12H, 21H, 22H, etc) as well as to the more dominant transitions such as the 11H or the barriers energy gap (GaAs gap), or other intersubband transitions at above-barrier energies involving continuum states such as the ones described in sect. 1-3 and 1-4. For this reason, a large part of the experimental work (e.g. see sect. 3-3) will be based on results obtained with PR or ER.

Spectra obtained with bulk semiconductor material will display features associated with the interband transitions, achieved by applying an alternating voltage (which modulates the electric field) across the sample, through a semitransparent Schottky barrier (as described above in sect.i). There exists methods other than the Schottky configuration to apply the voltage in ER, such as immersing the sample into an electrolytic solution, but this method is obviously not suitable at low temperatures where most of the interesting data are obtained. While the small alternating voltage modulates the electric field, a bias DC voltage may also be applied to analyzed the properties of the sample at various values of the electric field. Therefore, PR has the advantage that it does not necessitate electrical contacts, whereas ER can be used to quantitatively control the electric field applied to the sample. PR or ER experiments on quantum well structures give spectra with typical derivative lineshapes associated to the intermediate transitions (such as 12H, 21H, 22H, etc) as well as to the more dominant transitions such as the 11H or the barriers energy gap (GaAs gap), or other intersubband transitions at above-barrier energies involving continuum states such as the ones described in sect. 1-3 and 1-4. For this reason, a large part of the experimental work (e.g. see sect. 3-3) will be based on results obtained with PR or ER.

Spectra obtained with bulk semiconductor material will display features associated with the interband transitions, present in the energy range scanned, such as the fundamental gap E_g. Oscillations associated with the Franz-Keldysh effect† are often observed at above-gap energies. These oscillations are very different from the ones related to the continuum states of a Quantum Well structure having a finite cap layer as described in sect. 1-3 and 1-4. The Franz-Keldysh oscillations follow the relation

$$E_n = E_o + \alpha\ (n - 1/2)^{2/3}, \tag{2-1}$$

where E_n is the energy of the n-th extremum, E_o would be the energy of the gap, and

$$\alpha = \left(\frac{3\pi e\hbar F}{4\,(2\mu)^{1/2}}\right)^{2/3}$$

is related to the electric field F, and to μ, the electron-hole reduced mass. A plot of the experimental values of E_n vs $(n - 1/2)^{2/3}$ gives an accurate measurement of the energy gap E_o, and of the electric field F. Furthermore, if the electric field F is changed by varying the voltage across the sample (V_a), then the electric field can be calibrated as a function of the applied voltage. Comparing these values of field with the equation $F = F_o + V_a/d$ (which would be valid for uniform field), would give information about the thickness (d) of the

† *A80, p.140, P91*

intrinsic region of the sample across which the voltage is dropped, and about the built-in field (F_o). The above procedure will be demonstrated with a GaAs epilayer in the sequential study (sect. 3-2). Franz-Keldysh oscillations may also be observed in spectra obtained with Quantum Well samples since they also contain a large fraction of bulk material[CC91,CV90]. Therefore the electric field and thickness of these samples can also be calibrated using the Franz-Keldysh effect (see sect. 3-3).

Because of the derivative nature of the lineshape and the sensitivity of the technique to almost all the transitions, the spectral features obtained with ER or PR of Quantum Well heterostructures can sometimes be complicated. So a careful analysis of the lineshape may be required to accurately determine the energy positions of the various transitions. A spectrum S(E), where E is the photon energy of the probing beam, may be fitted using[A80]:

$$S(E) = \mathrm{Re}\left[\sum c_j e^{i\theta_j} (E-E_j + i\Gamma_j)^{-m_j}\right]. \tag{2-2}$$

Where Re[ ] denotes the real part, and the summation is over all the transitions participating to the signal. E_j is the energy of the j^{th} transition, c_j is the amplitude, Γ_j is the broadening factor, θ_j is the phase, and m_j is related to the order of the derivative which is determined by the type of critical point. For example m_j=5/2 and m_j=3 would correspond to third derivatives of 3-D and 2-D critical points respectively, whereas m_j=1/2 and m_j=1 would correspond first derivatives of 3-D and 2-D critical points respectively[A80,Z91,T91]. First derivatives are expected for bound systems such as excitons, impurities or isolated (uncoupled) quantum wells when the electron/hole pair cannot be accelerated by the alternating field†. Nevertheless, many authors have analyzed quantum well structures with third-derivative lineshapes[Z91,G90]. For that purpose, the lineshape of a typical ER spectrum of the 11H transition obtained with a SQW was analyzed using various values of m_j. Results of the fit are shown in fig. 2-6 for m_j values between 1 to 3 by increment of 1/2. These values of m_j would cover various dimensionalities and different orders of derivatives. It is clear from that figure that the fit obtained with a third derivative of a 2-D critical point (m_j=3) is far better than the one obtained with a first derivative for such a critical point (m_j=1). The third derivative lineshape could be explained because the wells in the InGaAs/GaAs system are not very deep (shallower than about 100 meV for the heavy holes), therefore the electric field and the thermal energy may delocalize the carriers. In any case, the energies (E_j) obtained using either exponents are all quite comparable within a few tenths of meV (here E_{11H}

† *P91, PG88, G90, GS89, J89, HQ91*

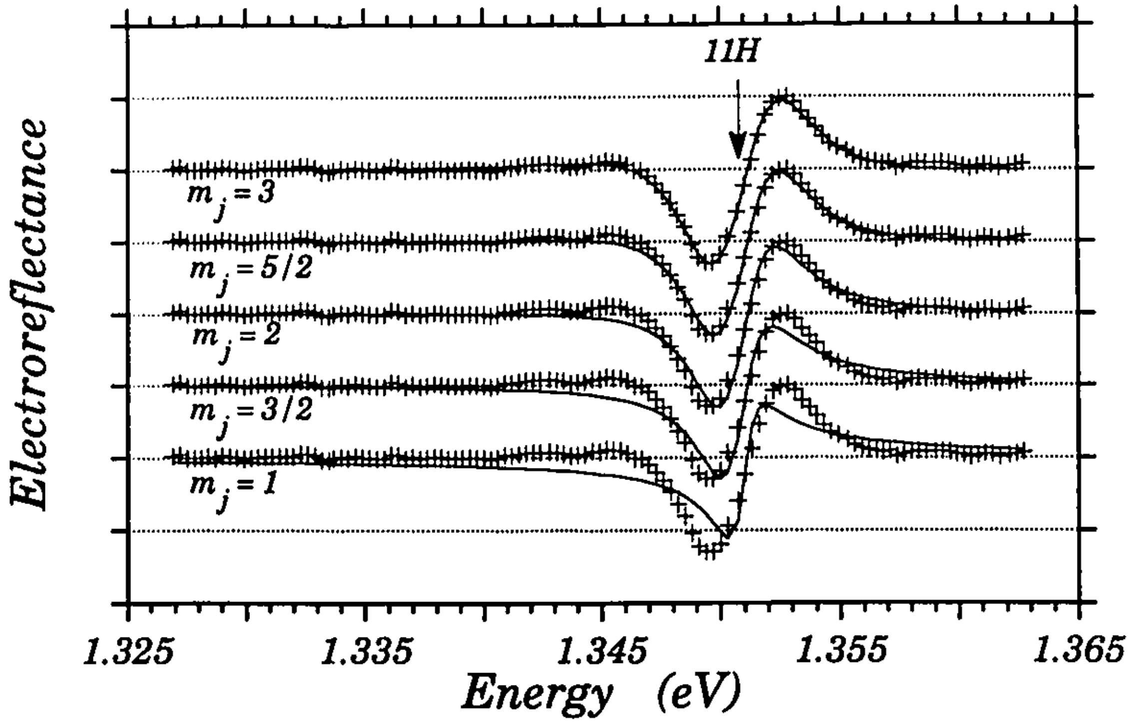

Fig. 2-6: Fit of the spectral lineshape obtained in ER for the 11H transition of a SQW at T = 77 K. The best fit (solid curve) obtained with different values of m_j in eq. (2-2) are compared for the same spectrum (crosses).

= 1.3508 ± 0.0001 eV), but the analysis yielded broadening values ranging from Γ_j=3.4 meV for m_j=3 to Γ_j=0.7 meV for m_j=1, in agreement with the findings of others[Z91].

The experimental set-up used for the PR or the ER is schematically represented in fig. 2-7. The required beam of monochromatic light is obtained by dispersing the light emitted by a 30 Watts quartz iodine source with a spectrometer such as the one described for the PL in sect. 2-2. The visible and infrared (IR) photons emitted by the tungsten filament are collected and directed to the entrance slit of the

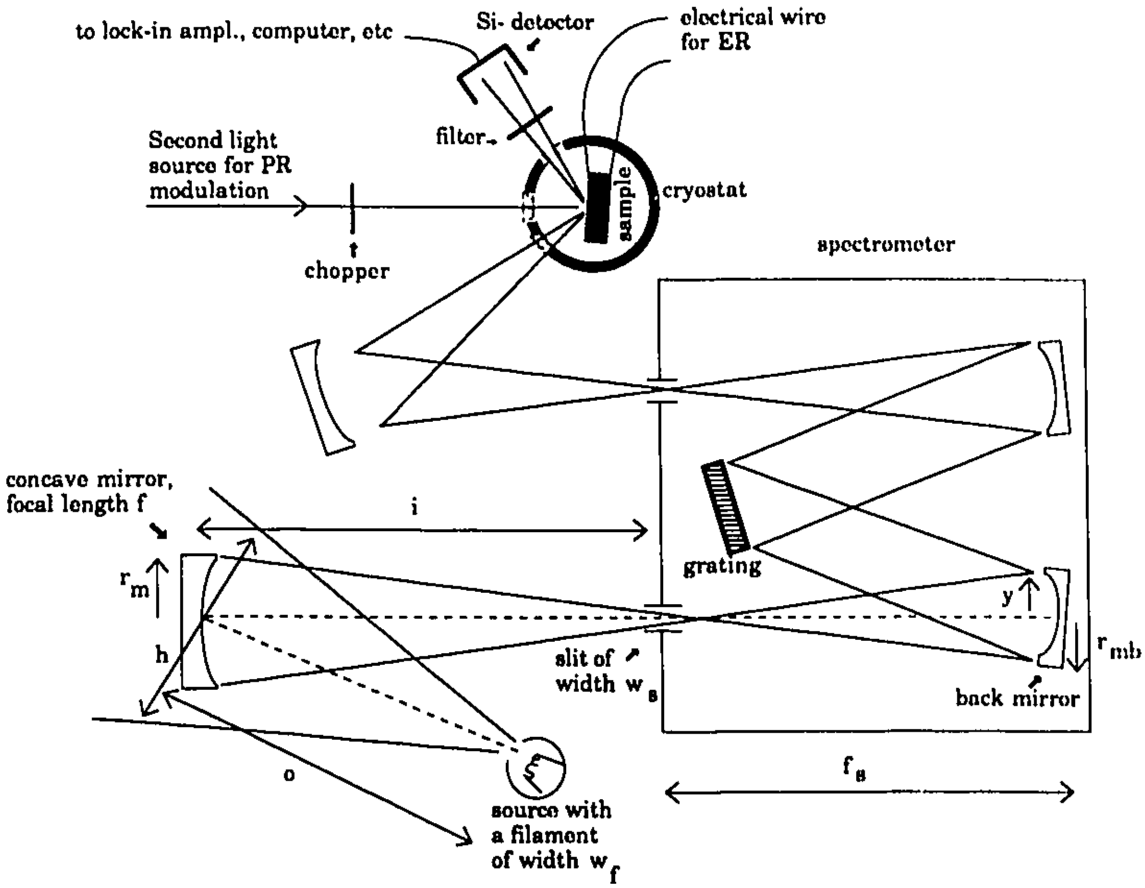

Fig. 2-7: Monochromator using a single mirror to collect the white light emitted from a tungsten source, and set-up used in PR and ER experiments.

spectrometer with a single concave mirror. Appendix 2 describes how to maximize the amount of light collected with such a system. The monochromatic beam exits the spectrometer, and is reflected, with another concave mirror, on the sample through one of the optical windows of the cryostat. The sample inside the cryostat is positioned in such a way that the reflected light is directed on a silicon detector placed outside the exit window. For PR, the modulating light was mechanically chopped, and could be introduced by a third window situated between the entrance and the exit windows. A filter was placed in front of the detector to cut the scattered modulating light. The PR modulation source was either a second monochromator operated at a fixed wavelength or an attenuated argon-ion or HeNe laser. The energy of the modulating photons was larger than the energy gap of the barrier (GaAs), and larger than the energy of the probing beam as well. Within the above conditions, the spectra were not affected significantly by the choice of the energy of the modulating light. In ER, a small alternating voltage was applied to the sample contacts (the Schottky configuration used is described in sect. 2-1), simultaneously with an adjustable DC bias. The PR or the ER signal from the detector was measured with a lock-in amplifier, digitized, stored and analyzed with a computer.

Even though PR and ER experiments provide valuable information for the characterization of the energy levels, their possibilities of practical applications are limited. Spectra obtained with other optoelectronic techniques such as PV or EL also provide useful information about the energy levels, and have definite possibilities for practical application such as energy selective detectors and emitters. These techniques are described in the next section.

2-4 Photovoltage (PV) and Electroluminescence (EL):

Samples with a Schottky barrier, as described in sect. 2.1, can also be studied by PV or EL techniques. PV, as for ER or PR, will be sensitive to the intermediate transitions in quantum well heterostructures. PV may also be used to study electric field effects. Unlike the modulation techniques, which give derivative-like lineshapes, PV will be sensitive to direct changes in the optical properties due to modification in the absorption coefficient related to the various energy levels. EL, as for PL, will favor the lowest transition, but the carriers are pumped electrically instead of optically.

PV uses a set-up very similar to the one described in the previous section for ER. The light from the spectrometer is chopped, and sent through the gold electrode; the sample is used as a light detector, the PV being measured by standard synchronous techniques. For EL, the sample was biased with small-duty-factor pulses of forward voltage, and the light emitted through the semi-transparent gold contact was dispersed with the spectrometer and detected with the PM as described in sect. 2-2. for PL. The signal from the PM could be measured with a boxcar integrator, or if the duty factor of the pulse permits (i.e. if it is not too small), with a lock-in amplifier. In order to obtain a larger signal-to-noise ratio, a spectrometer with a larger aperture (and hence a lower resolution) having a focal length f_s = 25 cm could be used to disperse the EL.

Combining the information provided by the individual techniques of the above sections may allow for a better to understanding of the physical processes giving rise to the various spectral features. Alternatively, instead of analyzing a sample with various techniques, a specific technique may be used to study sequentially the component layers of a multi-layers sample. This may provide valuable information about the origin of the spectral feature. In any cases, the techniques chosen here, luminescence, PR or ER, and PV, complement well each other, and may in some ways be inter-connected. For example, a sample in a PV configuration can be used to study the effect of an electric field on the PL.

It is known that[SC91a,MB82] the QW luminescence intensity quenches rapidly with the electric field, and that the quenching rate is dependent on the excitation intensity. For example, fig. 2-8 illustrates typical results obtained at T = 77 K with a SQW (L = 12.0 nm, X = 0.165, t = 65 nm; see fig. 1-4). To show how the PL is quenched with an applied electric field, the logarithm of the wavelength-integrated PL signal is plotted as a function of the voltage which was applied to the sample through the Schottky barrier, for various intensities of excitation from ~ 1 W/cm^2 to ~ 10 mW/cm^2. The corresponding spectra (not shown) would show a narrow (typically ~ 5 meV of FWHM at about 1.350 eV) 11H peak in the flat band condition, which would be broadened, slightly shifted in energy, and quenched by increasing the electric field[MB82,KY86,MC84]. Of interest here, is the total amount of PL emitted by the QW as shown in fig. 2-8: the curves are characterized by two plateaus where the amount of PL emitted is not very much dependent on the applied voltage, joined together by a threshold region where the quenching occurs. For the plateau in the region of the positive voltages (forward bias near the flat band condition) the SQW emits up to almost 20 times ("ON state") more light than in the "OFF state" (i.e. the plateau in the region of negative voltages; larger electric field). It is also remarkable how the threshold is displaced toward higher electric field as the intensity of excitation is increased. In other words, the more PL there is, the larger the electric field it takes to quench the PL, as mentioned above for excitation intensity dependent quenching rate. The quenching has been attributed[SC91a] to the enhanced dissociation of the excitons into free carriers under the influence of the electric fields and/or carrier density. Srivinas *et al*[SC91a] also found that at low excitation, the photoluminescence process is excitonic, and at high excitation and high field, the process is bimolecular. Bimolecular recombination between free carriers in parallel with a strong nonradiative decay mechanism have been often associated with slopes around values of 2 on a

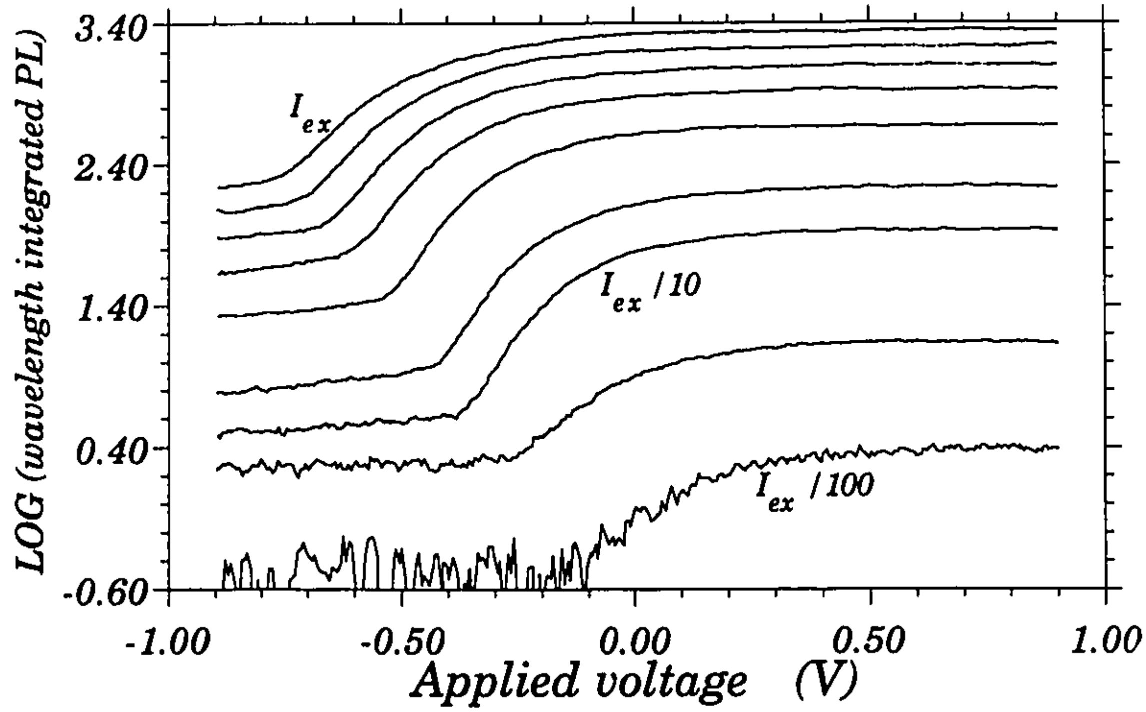

Fig. 2-8: Quenching of the PL of a SQW with an applied voltage for various intensities of excitation, at T = 77 K. I_{ex} ~ 1 W/cm^2.

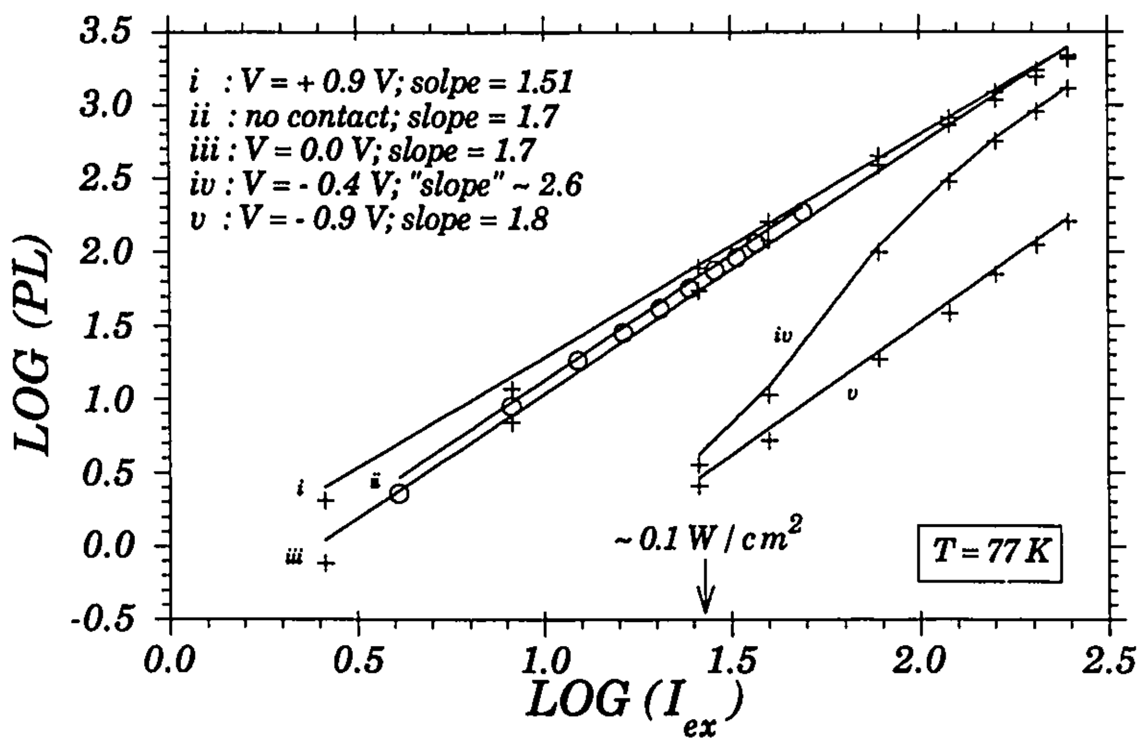

Fig. 2-9: Dependence of the wavelength integrated PL signal on the intensity of excitation for different values of applied voltages (crosses) from fig. 2-8, and for a contactless sample (circles).

logarithm plot of the photoluminescence versus excitation intensity[FS85,FB86]. Other authors[OF90,MK86,M86] have found interesting periodic variations of the indices m of the $I_{pl} \alpha I^m_{ex}$ relationships with the well width of the QW samples. They have analyzed and correlated these periodic variations of this index with the carrier trapping efficiency of the well. It is therefore interesting to plot the dependence of the PL intensity on the excitation intensity for the results of fig. 2-8. To that effect, fig. 2-9 shows logarithmic plots of the PL vs I_{ex} for various values of applied voltages (i.e. vertical cuts through the curves of fig. 2-8), and the corresponding plot for a virgin sample (i.e. without electrodes). The $I_{pL} \alpha I^m_{ex}$ relationships for the "ON" and the "OFF" plateau, for the case with no applied voltage and for the sample with no electrode, all have values of m between 1.5 and 1.8, as found from the slope of the lines in fig. 2-9. But for an applied voltage of -0.4 V, which is just in the (shifting) threshold region, the "slope" is much higher, reaching about 2.6 (actually it is clear that the relationship $I_{pl} \alpha I^m_{ex}$ does not hold for that situation since the logarithmic plot is not linear). From fig. 2-8 and 2-9, it is clear that the electric field favors the non-radiative processes, resulting in an onset region for the PL, which can affect the PL vs I_{ex} relationship significantly. It is also clear that samples prepared in a PV configuration may have interesting practical applications, as electrically or optically switchable monochromatic light emitter.

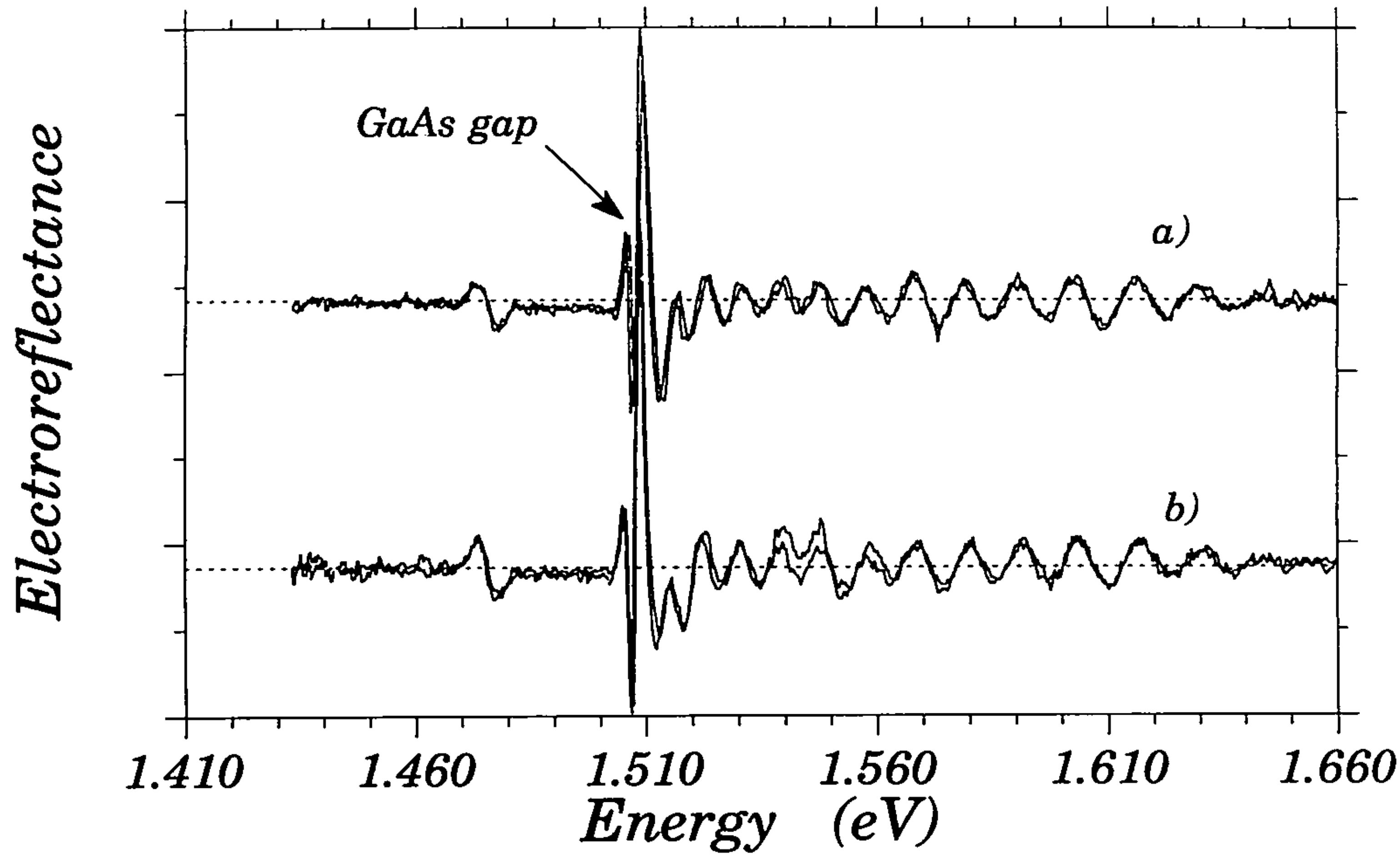

Fig. 2-10: ER spectra of a SQW at T = 77 K. In a) the modulating voltage is applied with an external power supply ($\bar{V}_a$ = 0.1 V). In b) the modulating voltage is generated internally with the PV effect by illuminating the sample with a chopped beam of light with the appropriate intensity.

As a second example of how the techniques discussed in the present chapter may be inter-connected, it is possible to show that the actual the mechanism responsible for the PR is the surface photovoltaïc effect[P91]. This is shown by shining a chopped secondary light beam, as in PR, on a sample with a Schottky barrier. The alternating voltage created by the the PV will induce an ER signal of a probing DC monochromatic beam. The ER spectrum generated in this way will not differ significantly from the usual ER spectrum obtained by applying an alternative voltage with an external power supply. To conclude this chapter, fig. 2-10 illustrates this particular example by comparing an ER spectrum excited with a voltage applied externally with a power supply, in curve a); and an ER spectrum excited with the PV obtained from illumination of the sample with a chopped beam with the appropriate intensity, in curve b). The next chapters will present and discuss the experimental results for the influence of the surroundings, and of the well parameters on the energy levels of QW structures, as studied with the techniques mentioned in the present chapter.

CHAPTER 3

INFLUENCE OF THE SURROUNDINGS, AND OF THE WELL PARAMETERS ON THE ENERGY LEVELS

3-1 Sequential study of the influence of the substrate and buffer layers.................................... 76

3-1-1 Substrate.................................... 77

3-1-2 Buffer.................................... 79

3-1-3 Complete SQW.................................... 83

3-2 Influence of the cap.................................... 98

3-2-1 Without an electric field.................... 98

3-2-2 With an electric field....................... 107

Most of the experimental results are contained in this chapter. It is partitioned in two main divisions. Section 3-1 describes the results obtained in a sequential study which was performed to determine the influence of the substrate and buffer layers on the response of complete SQWs. Sect. 3-2 deals with the results obtained with SQWs having various cap layer thicknesses and/or well widths. The latter section gives the experimental evidence of the influence of the finite-size of the cap layer on the continuum states of SQWs described theoretically in chapter 1. Unless otherwise specified, all the results presented were obtained a T = 77 K. The sequential study in sect. 3-1 was performed on an $In_{0.135}Ga_{0.865}As/GaAs$ SQW with a nominal well width L = 5.0 nm, and its component layers. The energy levels of this SQW can be found from fig. 1-2. The five samples studied in sect. 3-2 had a composition X = 0.165, and are listed with their parameters in table 3-1. Their bound states can be found by inspection of fig. 1-4, and also the continuum states of sample 1 had been studied theoretically in sect. 1-3 and 1-4, fig. 1-5 to 1-10.

Table 3-1: Paramaters of the samples studied in sect. 3-2.

sample #	1	2	3	4	5
well width (nm)	3.5	3.5	3.5	12.0	8.0
cap thickness (nm)	50	65	100	65	65

3.1 Sequential study of the influence of the substrate and buffer layers:

The component layers of the SQW to be studied sequentially and systematically were sketched in fig. 2-1. The details about the sample growth and preparation was given in sect. 2-1, and the details about the experiment techniques were given in the other section of chapter 2.

3-1-1 Substrate:

The optical response of the substrate was investigated in the spectral range of interest using PV, EL, and PL ($\lambda_{exc.}$ = 632.8 nm) : see fig. 3-1*a*, *b*, *c* respectively. Clearly two dominant features are present, indicating the intrinsic (peak I) and extrinsic (peak II) nature of the substrate. Peak I at 822 nm (1.508 eV) is associated with band-to-band recombinations across the GaAs gap (1.508 eV at 77 K). Peak II at about 838 nm is related to the introduction by the Si dopant of an acceptor level 35 meV above the valence band[LB86], Si being an amphoteric dopant in GaAs[KD68]. The difference in relative amplitude between peak I and II from one technique to another is attributable to different degrees of reabsorption. In the case of PV, for energies larger than the gap, the signal increases monotonically because, as the wavelength is decreased, the absorption coefficient increases and more light is absorbed in the very narrow active depletion width.

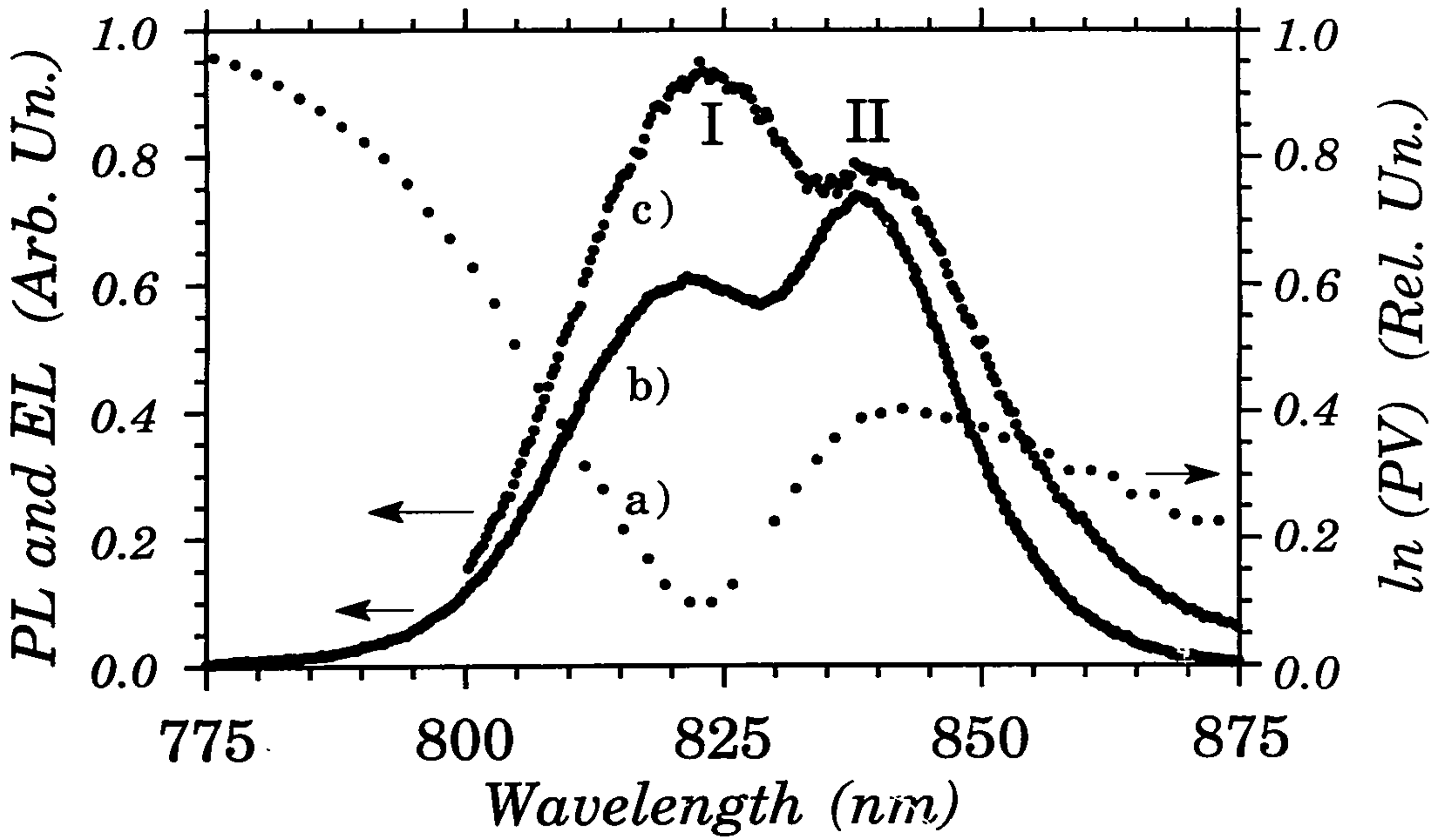

FIG. 3-1: Spectra obtained with the Si-doped GaAs substrate at T = 77 K: a) PV with a gold electrode on top; b) EL with a gold electrode on the top; c) PL excited with $\lambda_{exc} = 632.8$ nm.

3-1-2 <u>Buffer and substrate</u>:

Results obtained with a 2 μm thick buffer layer grown epitaxially on the substrate are shown in fig. 3-2. Curve *a* is a PV spectrum having a natural logarithmic vertical axis to highlight small-amplitude features at long wavelengths. Curve *b* is a PL spectrum with $\lambda_{exc.}$ = 514.5 nm. Curve *c* and *d* are EL spectra with a barrier and an ohmic contact on the buffer layer respectively. The ohmic contact was a semi-transparent thin film of evaporated AuGe[HM85]. Note that spectra *c* and *d* are broader due to the use of a low-resolution spectrometer, given that the signal-to-noise ratio was small in the configuration studied. The impurity related "peak" originating from the substrate (peak II of fig. 3-1) is weakly-apparent or non-apparent in PV, PL and in EL spectrum *c*, the gap-related peak being the dominant feature. In EL spectrum *d*, the impurity-related peak originating from the underlying substrate is the dominant feature: in this case the n/n^+ barrier present at the epilayer-substrate homojunction generates the EL, explaining the predominance of a peak of substrate origin in spectrum *d*. Also, in the latter situation, a PV spectrum (not shown) showed the impurity peak and the gap peak having roughly the same relative magnitude, whereas for a barrier on the buffer (fig.3-2 *a*) the relative amplitude of these peaks was ≈ 1:200. Band-to-band EL is not observed in *d* because of reabsorption through the GaAs buffer layer. The impurity-

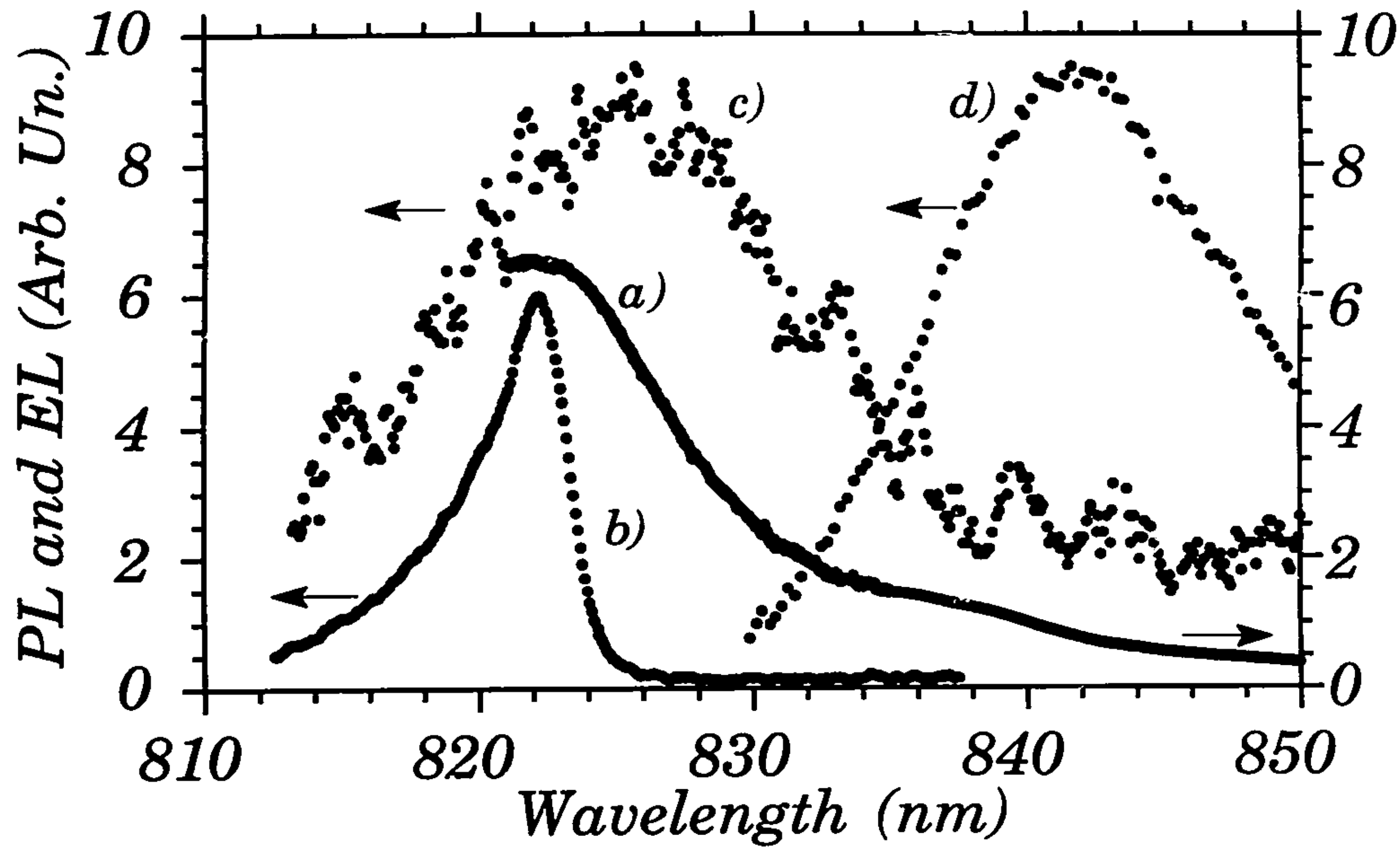

FIG. 3-2: Spectra for a 2.0 μm GaAs buffer on top of the Si-doped GaAs substrate at T = 77 K: a) PV; b) PL with λ_{exc} = 514.5 nm; c) EL with a gold barrier on top; d) EL with ohmic contact on top.

related peak of the substrate is not observed here in PL: using the known absorption coefficient[P85], one estimates that only $\approx 10^{-5}$ % of the exciting light at 514.5 nm goes through the 2 μm buffer layer.

For a thinner buffer layer however, it is possible to see the impurity-related substrate peak in PL, as shown in fig. 3-3 for a buffer 0.5 μm thick. Curve *a* is for $\lambda_{exc.}$ = 514.5 nm, in that case, 2 % of the exciting light reaches the substrate; and curve *b* is for $\lambda_{exc.}$ = 632.8 nm. In the latter case about 15 % of the exciting light is transmitted through the buffer, resulting in a more prominent impurity peak from the substrate (as seen previously in fig. 3-1, peak II).

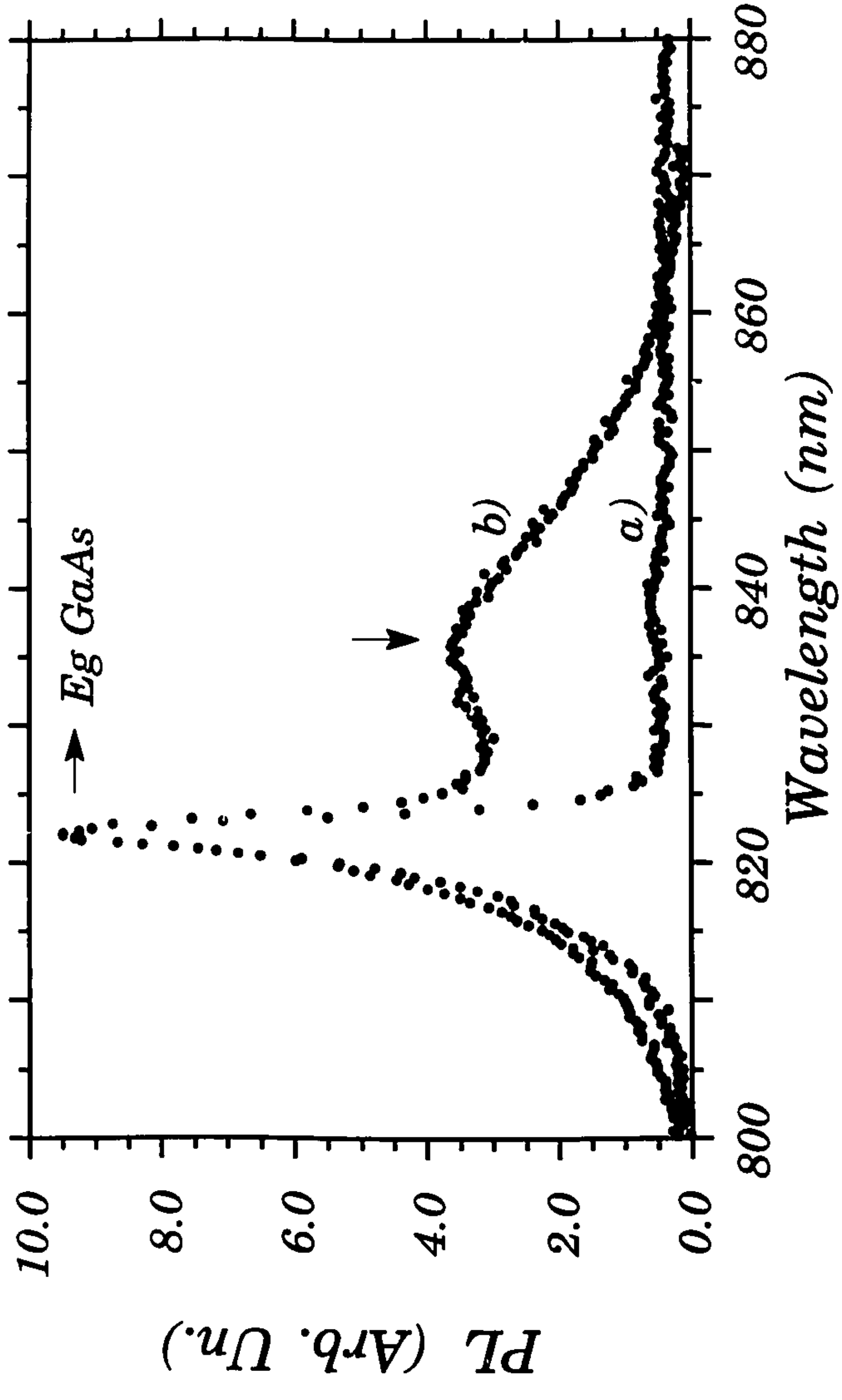

FIG. 3-3: PL spectra for a 0.5 μm GaAs buffer on top of the Si-doped GaAs substrate at T = 77 K. a) λ_{exc} = 514.5 nm; b) λ_{exc} = 632.8 nm.

3-1-3 Complete SQW:

Fig. 3-4 shows PV (curve *a*) and PL (curves *b* and *c*) results obtained with the complete SQW sample having a buffer of 450 nm, a well with X = 0.135 and L = 5.0 nm, and a cap with t = 85 nm. Curve *b* is for $\lambda_{exc.}$ = 514.5 nm and curve *c* is for $\lambda_{exc.}$ = 632.8 nm. The 11H transition in the QW at λ = 864.5 nm, the impurity-related substrate peak and/or peak(s) related to an intermediate transition in the QW, and the GaAs gap are clearly visible in PV. PV shows all the peaks because the sample is profiled in depth as the wavelength is scanned and the absorption coefficient is changed, and it would be sensitive to intermediate QW transitions such as 12H. In PL, $\lambda_{exc.}$ = 632.8 nm excites throughout the stacking down to the substrate, and so in addition to the 11H peak, the impurity-related peak from the substrate is observed. Also the small dip in curve c) around 820 nm is an indication of the resonant reabsorption in the over-layer at the GaAs gap. The situation is quite different for excitation at 514.5 nm; most of the absorption/recombination occurs above the substrate (in the cap, QW and buffer layers), and so the impurity-related peak originating from the substrate region is not observed. The GaAs band-to-band recombinations are not prominent in the complete SQW sample because photocarriers are efficiently captured by the quantum well and they relax to the confined energy levels (emitting LO phonons[B84]), giving rise to the 11H

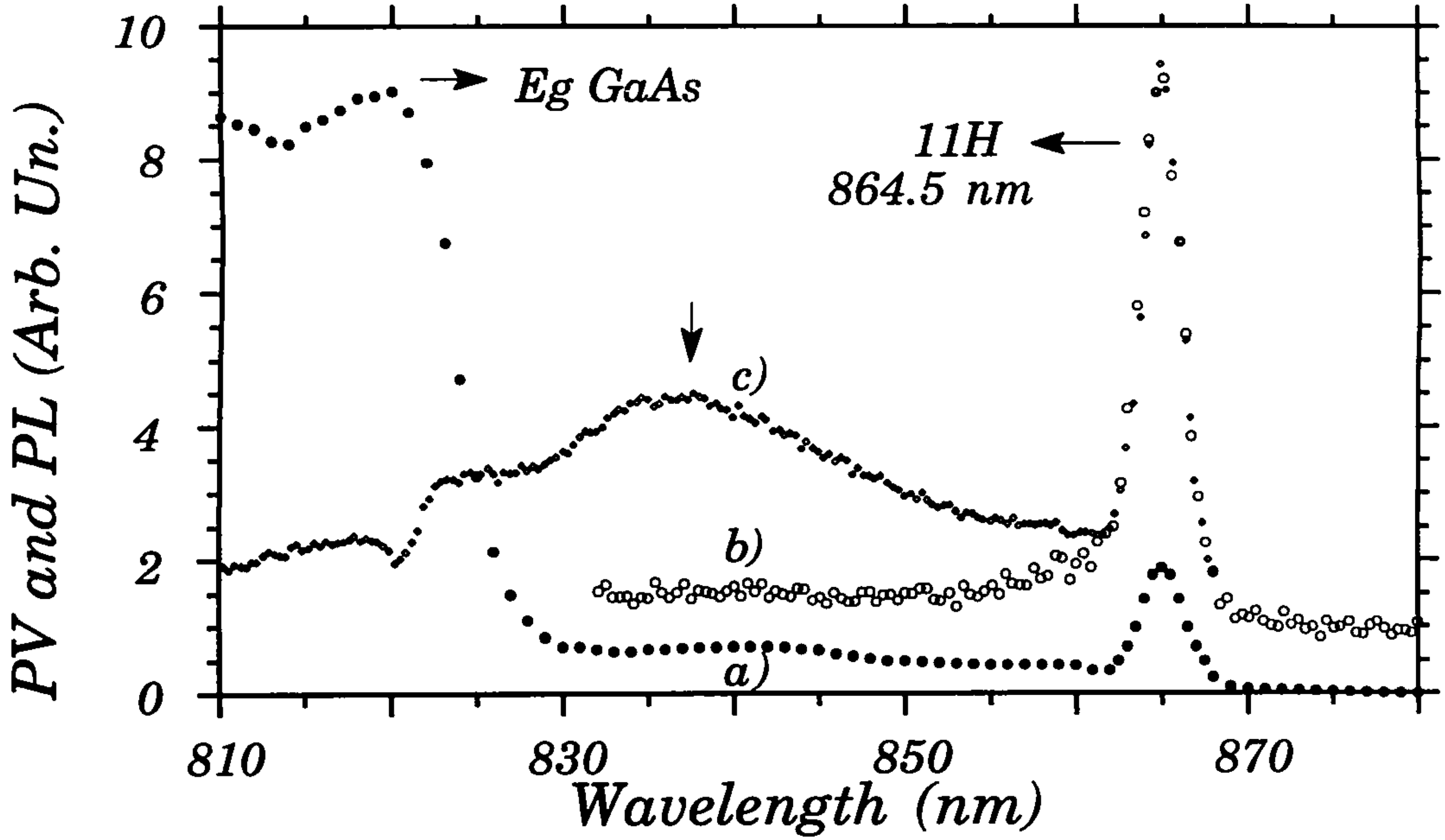

Fig. 3-4: Spectra for the complete stacking (as in fig. 2-1c) at T = 77 K: a) PV with a gold barrier on top; b) PL with λ_{exc} = 514.5 nm; c) PL with λ_{exc}= 632.8 nm. 11H is the transition from the first bound electron state (e_1) to the first bound heavy-hole state (hh_1).

transition.

While trying to predict which transitions could produce the higher energy peak(s), observed around 838 nm, in the PL spectrum excited at longer wavelength (curve *c* of fig. 3-4), one finds that the higher levels in the QW could give transitions in the vicinity of λ = 838 nm (see calculation in sect. 1-1, fig. 1-2). However, non-equilibrium photocarriers in the QW region relax non-radiatively into the fundamental electron and heavy hole levels, giving rise to the 11H transition, and unless either the e_1 or the hh_1 level begins to saturate, carriers in the higher energy levels would normally not recombine radiatively to give such peaks in PL. Estimates based on the density of carriers, and on the density of states in the QW suggest that neither the e_1 nor the hh_1 levels were saturated with the (low) intensity used to excite spectrum *c* of fig. 3-4. And so, the higher energy features of that spectrum are not of QW origin, but rather originate from the substrate, as seen before in sect. 3-1-1 and 3-1-2. To confirm this assessment, the PL results of the buffer alone can be compared with those of the SQW sample. To that effect, fig. 3-5 reproduces the low-intensity PL results of fig. 3-3 and fig. 3-4. The same broad feature is observed with the buffer alone and with the SQW when excited with 632.8 nm (fig. 3-5 *b* and *d*), whereas no such feature is seen with $\lambda_{exc.}$ = 514.5 nm in either case (fig. 3-5 *a* and *c*). Similar comparisons should

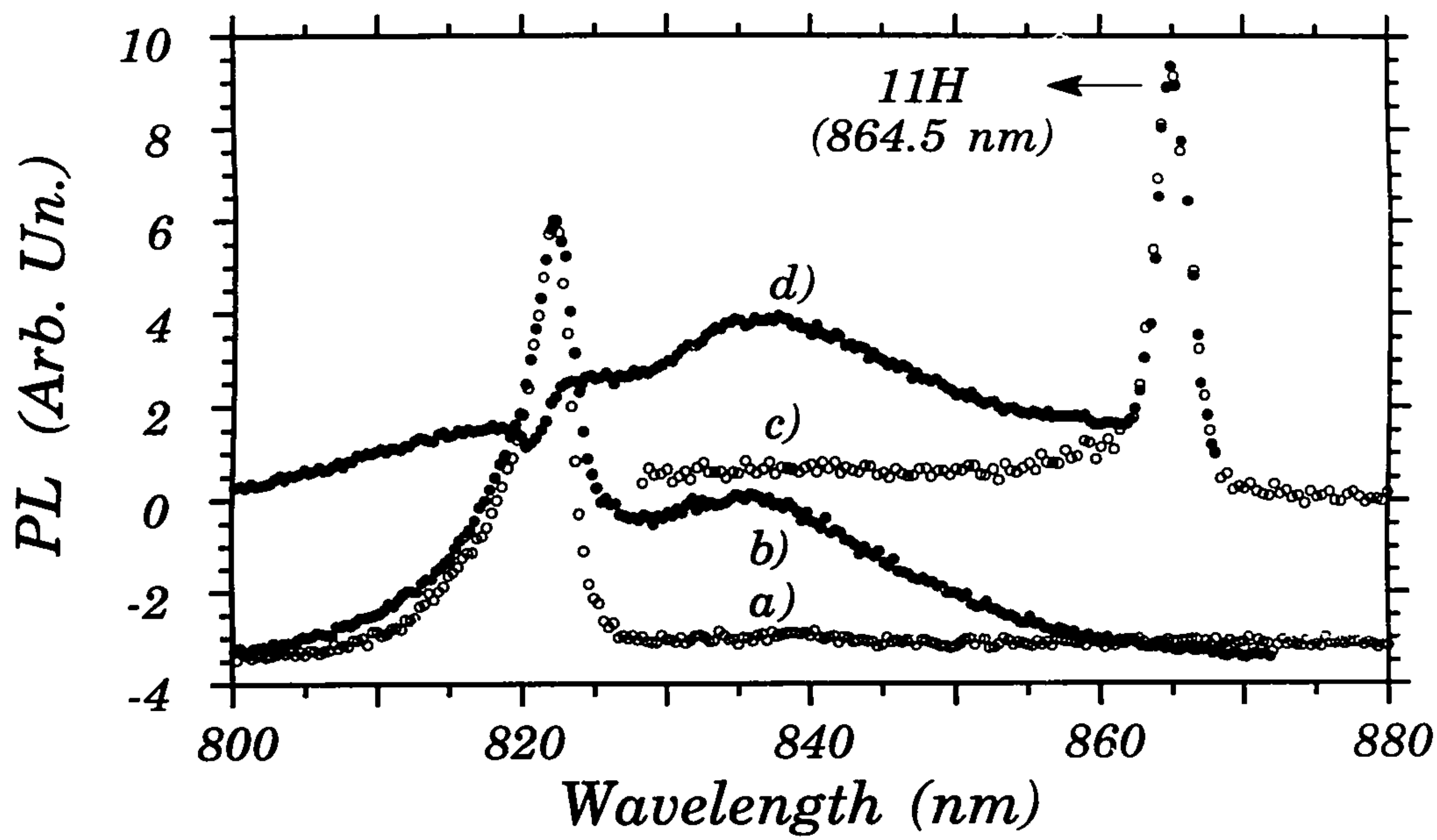

Fig. 3-5: Direct Comparison (at T = 77 K) of the PL results obtained in fig. 3-3 for the 0.5 μm buffer sample and in fig. 3-4 for the SQW sample: a) and b) are for the 0.5 μm buffer, c) and d) are for the SQW; a) and c) are excited with λ_{exc}=514.5 nm; b) and d) are excited with λ_{exc}= 632.8 nm.

be made to verify the origin of ambiguous transitions (i.e., observable QW transitions having the same energies as other possible transitions in the cladding layers) as was the case for the PV curve a) of fig. 3-4, or in the case of high-intensity PL measurements on samples using optically-active substrates like the one used here[FH89a].

Fig. 3-6 give an example of high intensity PL measurements excited with a pulsed dye laser at λ = 600 nm obtained for three intensities of excitation at T = 5 K[FH89a]. Results at T = 77 K were similar, the peaks being shifted by about 5 nm towards longer wavelengths. The spectra show the 11H peak, and as the intensity of excitation is increased, a peak at higher energies becomes prominent. Because of the higher intensity of excitation used here (I_{ex} up to ~ 10^5 W/cm^2), the peak at energies higher than the 11H peak could be associated with the saturation of the 11H transition, so that a peak involving an excited level such as the 12H transition would appear. However, studying a corresponding buffer layer (i.e. a 0.5 μm GaAs buffer layer grown on a Si-doped substrate, as in fig. 2-1b) under the same conditions leads to spectra such as those shown in fig. 3-7. Fig. 3-7 shows the PL excited with a pulsed YAG laser at λ = 532 nm obtained for three intensities of excitation at T = 77 K. For the lowest intensity, only the PL related to the GaAs gap is observed, but has the intensity is increased, the impurity-related peak originating from the

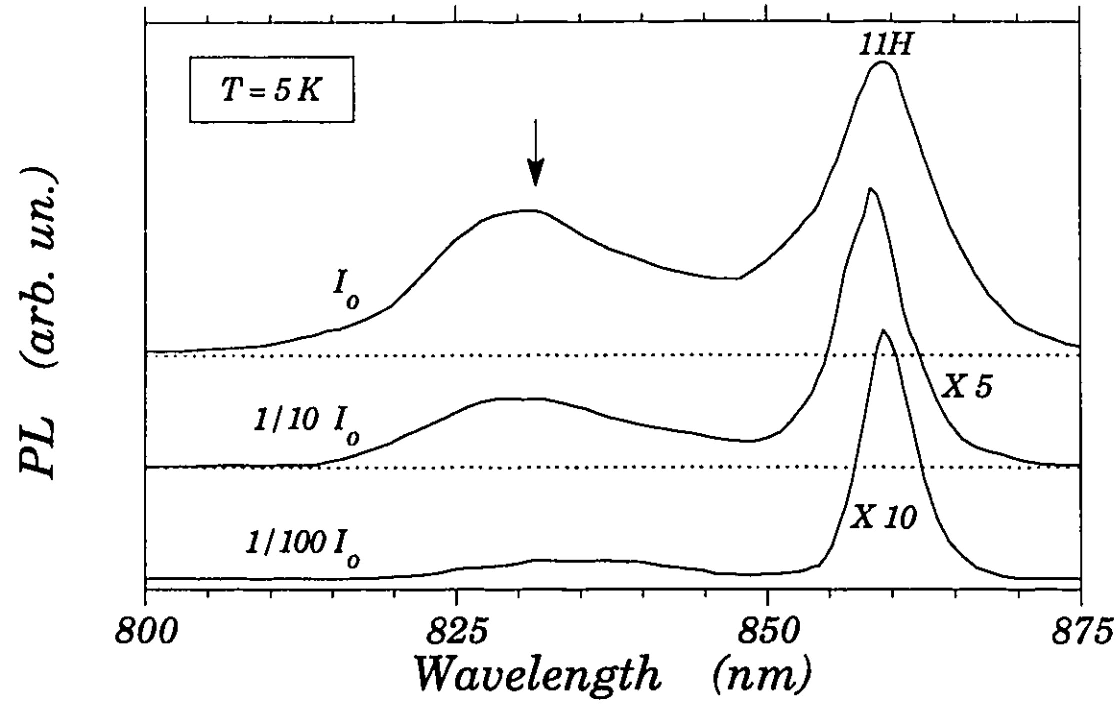

Fig. 3-6: PL spectra of a 5.0 nm InGaAs/GaAs SQW at T = 5 K for high intensities of excitation. $I_o \sim 10^5 W/cm^2$, and the SQW is grown on a 0.5 μm buffer.

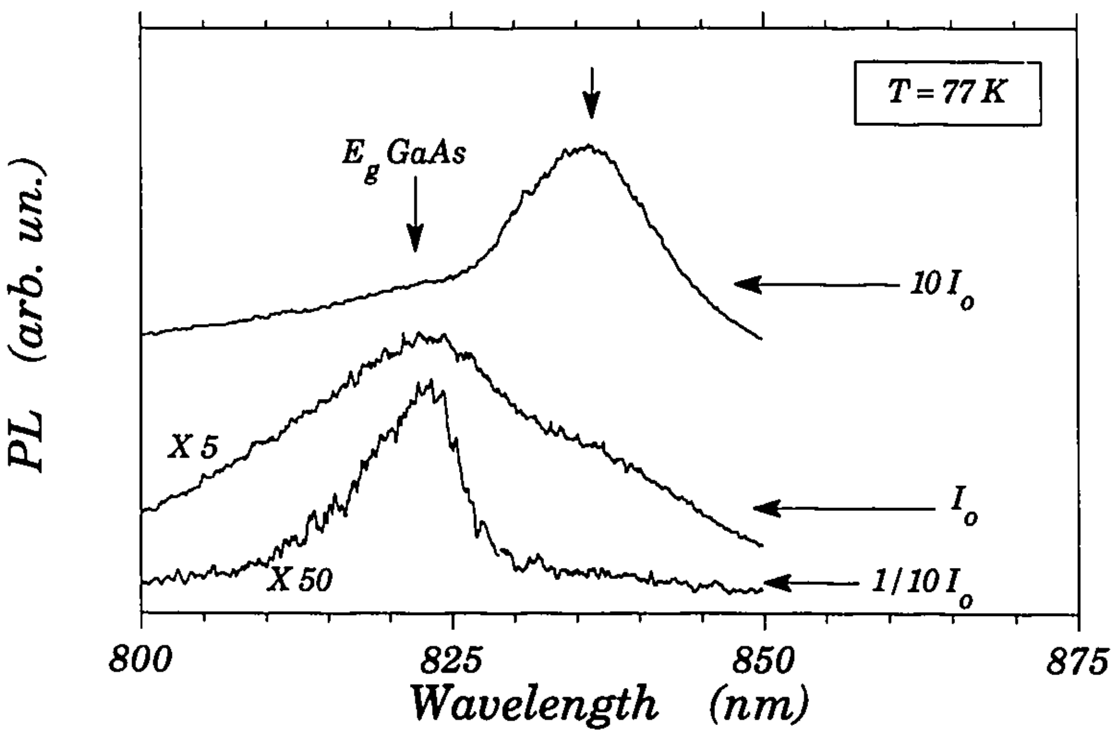

Fig. 3-7: PL spectra at T = 77 K for a 0.5 μm buffer for high excitation intensities ($I_o \sim 10^5 W/cm^{-2}$).

substrate becomes prominent. Comparing the results of fig. 3-6 and 3-7, it is clear that at least part of the peak observed with the SQW in fig. 3-6 was attributable to the impurity-related peak originating from the substrate. And so it is clear that in high-intensity PL measurements, such impurity peaks may be present even when short excitation wavelengths are used. In such a situation, a significant amount of the exciting light is transmitted through the buffer layer into the substrate (even though the percentage of light transmitted may be small); and because of the high concentration of carriers photocreated at the surface, carrier diffusion away from the surface will enhance the response of the substrate at the expense of the QW transition(s). These substrate peaks can be misinterpreted for, or superimposed on, QW transitions, which could appear as the QW ground states begins to saturate[FH89a].

Depending on experimental conditions, it is also possible to observe substrate-related peaks in EL as shown in fig. 3-8. Curve *a* is obtained when a semi-transparent gold barrier is deposited on the cap layer of the SQW sample and low voltage pulses are applied (current up to 20 mA here). Only the 11H transition is observed, indicating that recombination occurs at the top of the sample in the depletion region created by the gold Schottky barrier, which extends into the QW region. However, when the current is increased above a given value

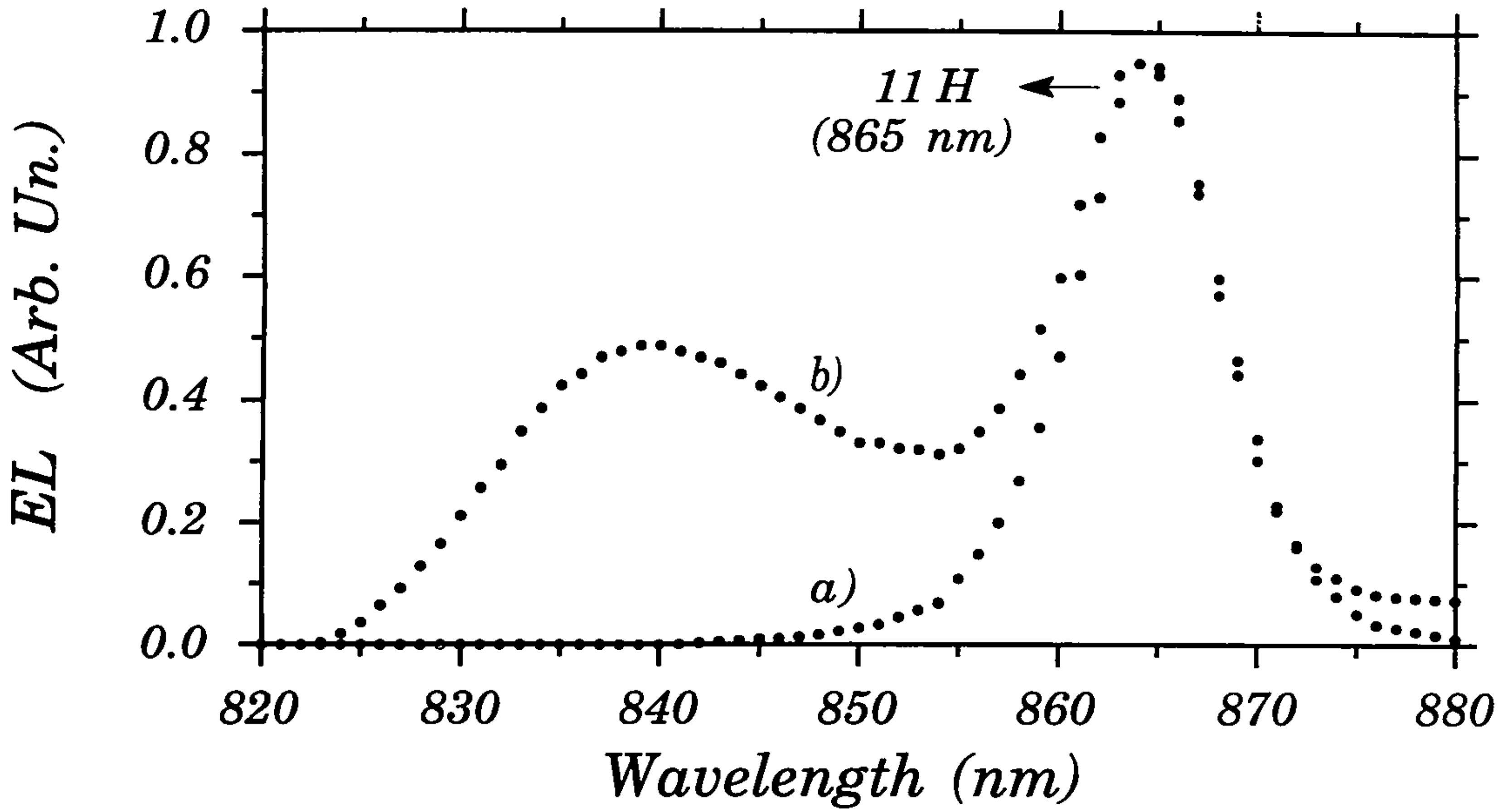

Fig. 3-8: EL spectra of the SQW sample at T = 77 K. With a gold barrier on the cap layer, only the QW related EL is observed: curve a). With a quasi-ohmic contact on the cap layer, a weaker QW related EL is observed as the EL originating from the homojunction displays the substrate related impurity peak, curve b).

(≃ 25 mA in this case), irreversible changes occur, leadingto a spectrum with a broad feature in the vicinity of 840 nm: see curve *b*. Further increases in voltage/current produce a relative decrease in amplitude of the 11H peak with respect to the broad peak. Finally, only the broad peak was observed, even at low current. The explanation may be that after the application of relatively high voltage/current pulses, the top gold contact became ohmic and the resultant EL was then generated at the substrate-epilayer homojunction barrier, displaying the impurity-related peak of the substrate. Similar "contact formation" was also observed with the buffer-substrate alone leading to EL spectra similar to fig. 3-2 *c* and *d*.

The calculations based on the model of sect. 1-1 (see fig. 1-2), predicted the following possible transitions for the 5.0 nm sample studied above:

11H at E = 1.434 eV; 864.5 nm(excitonic),
12H at E = 1.470 eV; 843 nm,
ec-1H at E = 1.480 eV; 838 nm,
e1-cH at E = 1.470 eV; 843 nm,

where ec-1H means a transition from the electron continuum edge to hh_1, and similarly e1-cH is a transition from e_1 to the heavy-hole continuum edge. The last three transitions have energies close to the energy of the broad feature observed in the PL spectra excited at 632.8 nm. And so, one could have been tempted to assign one of these transitions or combination of them to that broad peak. The sequential study showed that this peak originated from the substrate and not from the QW. The only peak of QW origin observed in PL here was the 11H. The other transitions calculated above are more commonly observed with other techniques such as PLE, PR, or ER.

In conclusion to the sequential study, it was shown that when GaAs substrates highly doped with Si are used as the building block of the QWs, care must be taken in the interpretation of the results of spectroscopic studies performed on the complete QW sample. This type of substrate, which is often used to get good electrical conductivity even at very low temperatures, has an energy level in the gap associated with the dopant impurity. This impurity level may produce a peak which happens to occur at an energy where other QW transitions could have been observed. The sequential study was used to demonstrate that the peaks observed around these energies were not of QW origin, or at best they could be a convolution of the QW and the substrate peaks. In PL when experimental conditions allow the exciting light to reach the substrate (long wavelength of excitation, thin buffer layer, or high-intensity excitation), one may get a peak originating from the substrate of amplitude comparable to that of the peak originating from the fundamental QW transition (the 11H peak). Therefore, a judicious choice of the wavelength of excitation and/or a sequential study may be required if some QW transitions are thought to be observable and might be coincident with peaks originating from the cladding layers. This could avoid misinterpretation of the physical origin of the peaks observed in PL spectra obtained on such QW devices. For characterization purposes, it is therefore essential to use wavelengths of excitation having a high absorption coefficient, and compare these results with those obtained on a sample having the corresponding buffer without the QW. It was also shown that the use of a relatively thick buffer layer may help to isolate the QW from substrate influence, but this is likely to introduce some conductivity problem in electrically-active devices.

Using graphs such as fig. 1-2 to predict the well width dependence of the energy levels as a guide, and some caution to avoid the presence of unwanted peaks originating from the cladding layers, SQWs of different well widths and cap layer thicknesses will be studied in the next sections in order to understand better the physics of transitions involving continuum states. In particular, oscillatory behaviors, as predicted in sect. 1-3 and 1-4, will be observable with ER and PR techniques. And so before presenting these results in next sections, it is desirable to study the response of a buffer layer, grown on a Si-doped substrate, by PR and ER for future comparison with the results obtained with the SQWs. Fig. 3-9a shows a PR spectrum obtained on a 0.5 μm thick buffer layer. Fig. 3-9b shows ER spectra for various values of applied DC bias. The PR spectrum displays typical lineshape which is associated with the gap of GaAs, and some F.-K. oscillations due to the built-in field. These F.-K. oscillations are becoming more prominent as the applied voltage increases the electric field in the ER spectra of fig. 3-9b. The extrema follow eq. (2-1), and a plot of the experimental values of E_n vs $(n - 1/2)^{2/3}$ gives the values of the electric field applied to the sample. Fig. 3-10 shows these plots for the spectra of fig. 3-9b. The values of the electric field are calculated from the slope of the lines of fig. 3-10; and the lines intercept the y-axis at the value of the energy gap. Fig. 3-11 plots these values of electric field as a function of the applied voltage: the slope gives the thickness of the intrinsic (undoped) buffer region, and the intercept gives the built-in field. Values of 0.57 ± 0.03 μm and 29 KV/cm were obtained here respectively. This is in good agreement with the actual thickness obtained from the growth parameters of 0.5 μm. Similar calculations can be performed to obtain the values of the electric field on SQW samples if F.-K. oscillations are present in their ER spectra.

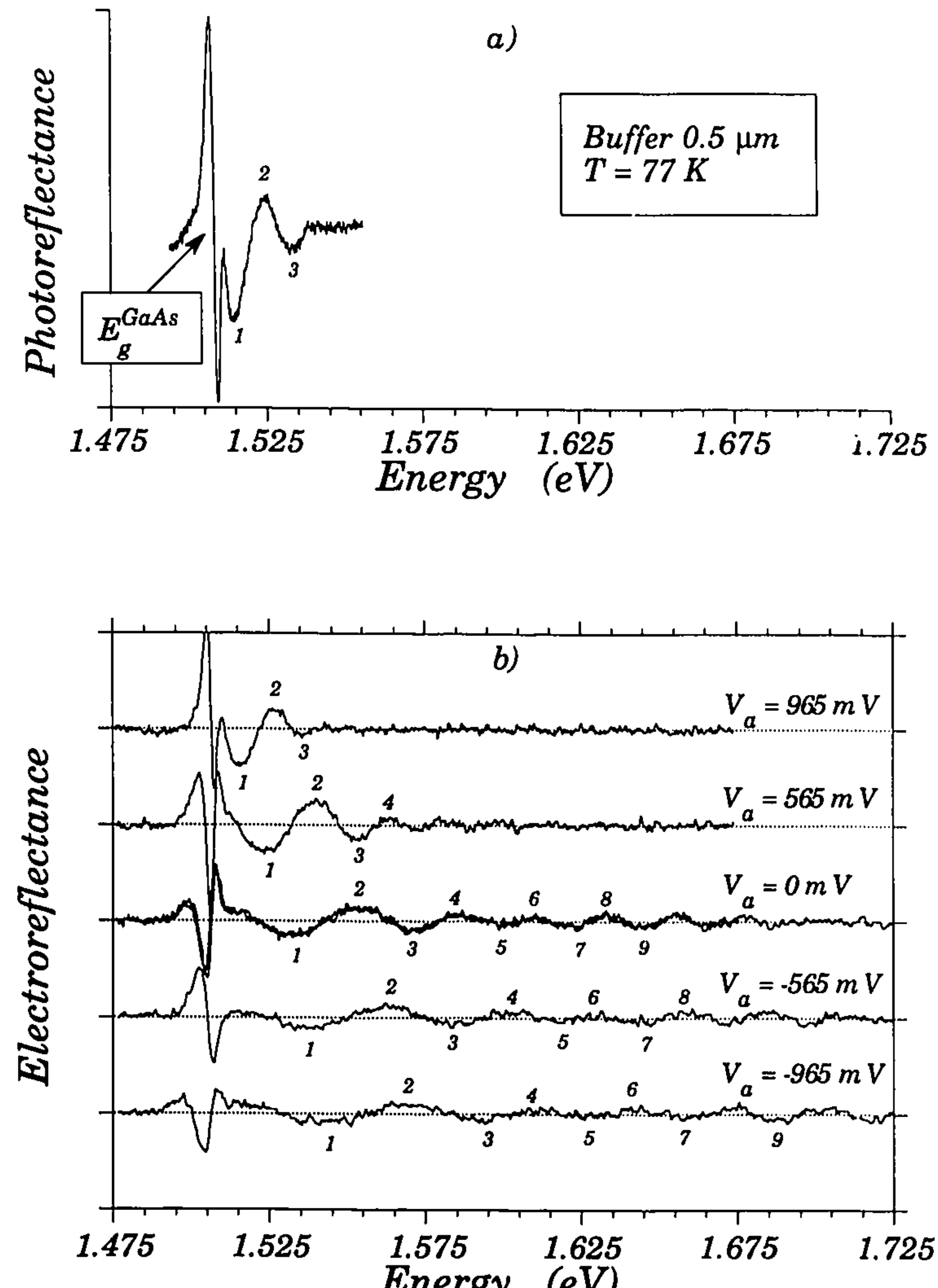

Fig. 3-9: Spectra obtained with a 0.5 μm buffer layer at T = 77 K. a) PR, b) ER for various bias voltages, showing F.-K. oscillations at above gap energies. The integers correspond to the indices (n) of the peaks used in fig. 3-10.

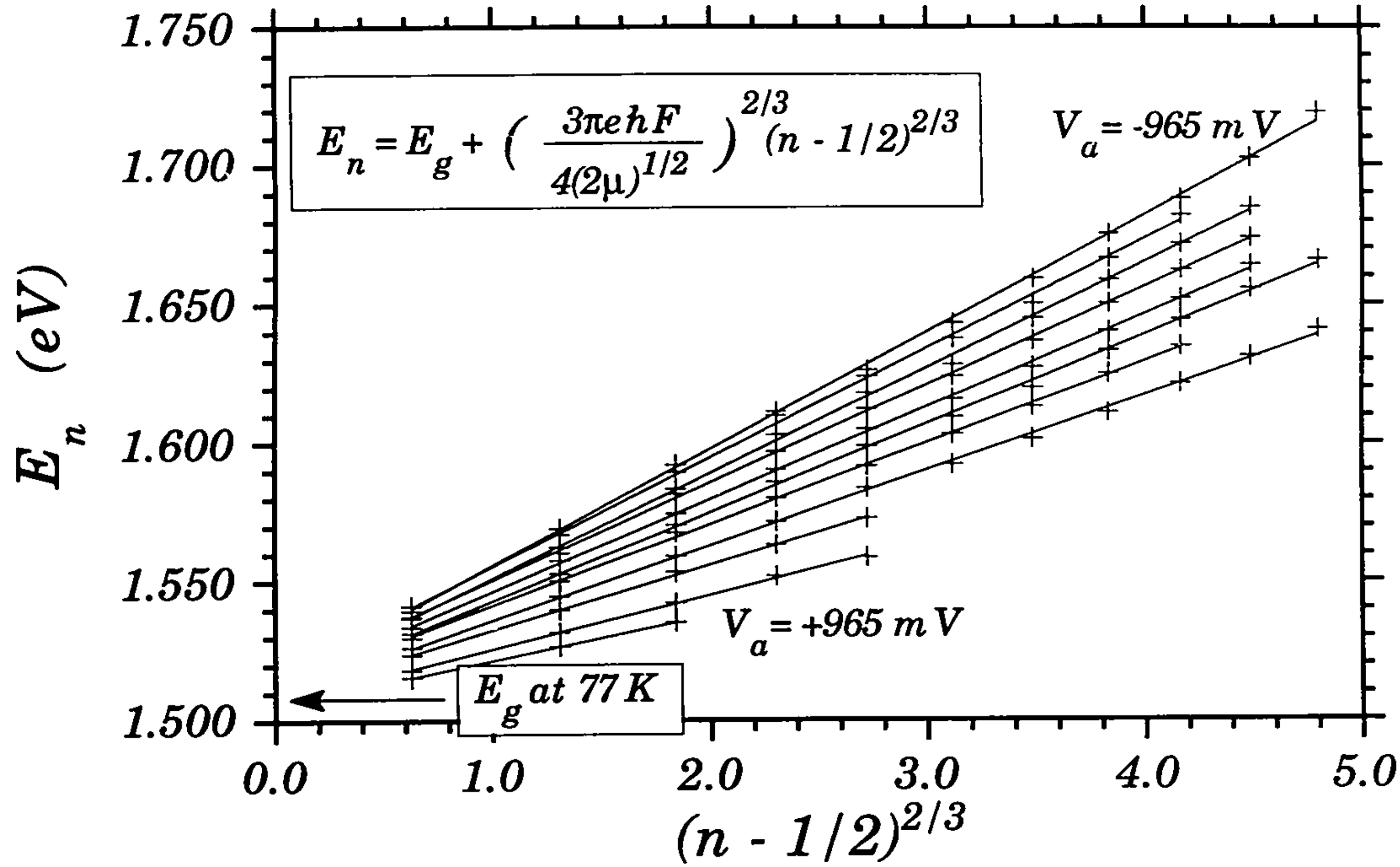

Fig. 3-10: E vs $(n-1/2)^{2/3}$ relationship for the Franz-Keldysh oscillations for a 0.5 µm buffer at T = 77 K, for various bias voltages (V_a) between -965 mV and +965 mV.

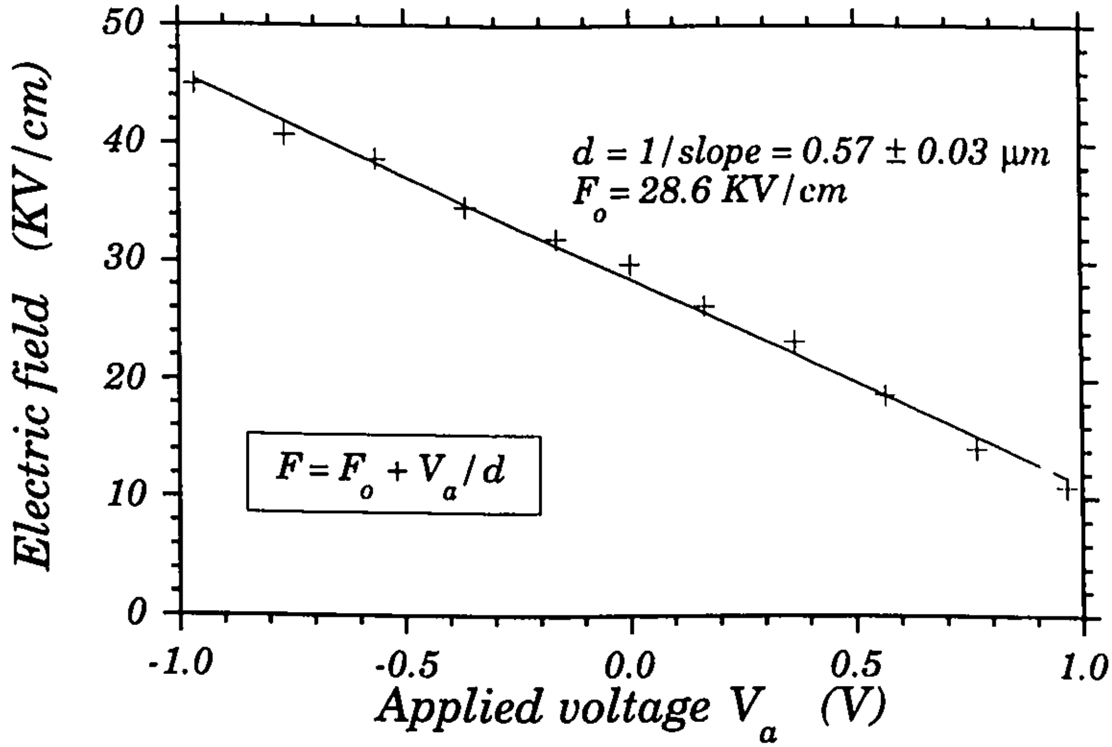

Fig. 3-11: Calibration of the electric field with the applied voltage, as found in fig. 3-10 from the F.-K. oscillations. The thickness of the buffer is found from the slope.

3-2 Influence of the cap:

Unlike the substrate or buffer layers, the cap layer cannot be studied without a well. The interesting properties of the cap layer are due to the presence of the well. And so in order to verify the influence of the cap layer, several samples having various cap layer thicknesses, or well widths, will have to be compared. It was shown theoretically in section 1-3 and 1-4 that the continuum states of a SQW would be significantly affected by the finite size of the cap and the presence of the high potential at the surface. The well occupancy, or the probabilities to find the carriers in the adjacent layers (cap and buffer), will oscillate depending on the energy of the carriers. Section 3-2 will show that PR an ER spectra display above-barrier oscillations which are related to the cap layer thickness. Section 3-2-1 describes PR results which will be valid to study the case with no electric field as in section 1-3. Section 3-2-2 presents ER results obtained to study of the influence of the cap layer in SQW in the presence of an electric field as described in section 1-4.

3-2-1 Without an electric field:

Because the epitaxial material is undoped, the band curvature at the external surface of the contacless samples should be minimum, so that PR (using low-intensity of excitation) will be an appropriate technique to study a near flat band condition as in fig. 1-3b. The modulating beam will vary slightly the electric field, and the test beam will create photocarriers which will have to redistribute among the various regions according to their most likely positions predicted by the probabilities of finding the carriers in the various regions. It was shown in sect. 1-3 that for the flat band condition the oscillations in the probabilities of finding the carriers in the various regions would vary with the energy. The energy variations were determined mainly by $\sin^2 k_b t$ which has its extrema given by eq. (1-13). It is also expected that for a given t, the spacing between adjacent extrema will depend on the value of m_b^*, so that for large enough t, the oscillations due to the heavy holes which have a large effective mass, will be very dense and therefore difficult to detect experimentally, while the electrons will still give observable oscillations because of their smaller effective mass. Hence, the type of carriers causing detectable oscillations is expected to change from the heavy holes to the electrons as t is increased. It was also shown that the contrast in the oscillations would be better for thin wells, and so as a first example, sample 1 has a well width of 3.5 nm for X = 0.16, and a cap layer of 50 nm. The bound states for such a SQW can be found from fig. 1-4: such a well has one electron and one heavy hole bound state. The corresponding experimental 11H peak is identified in fig. 3-12, curve a,

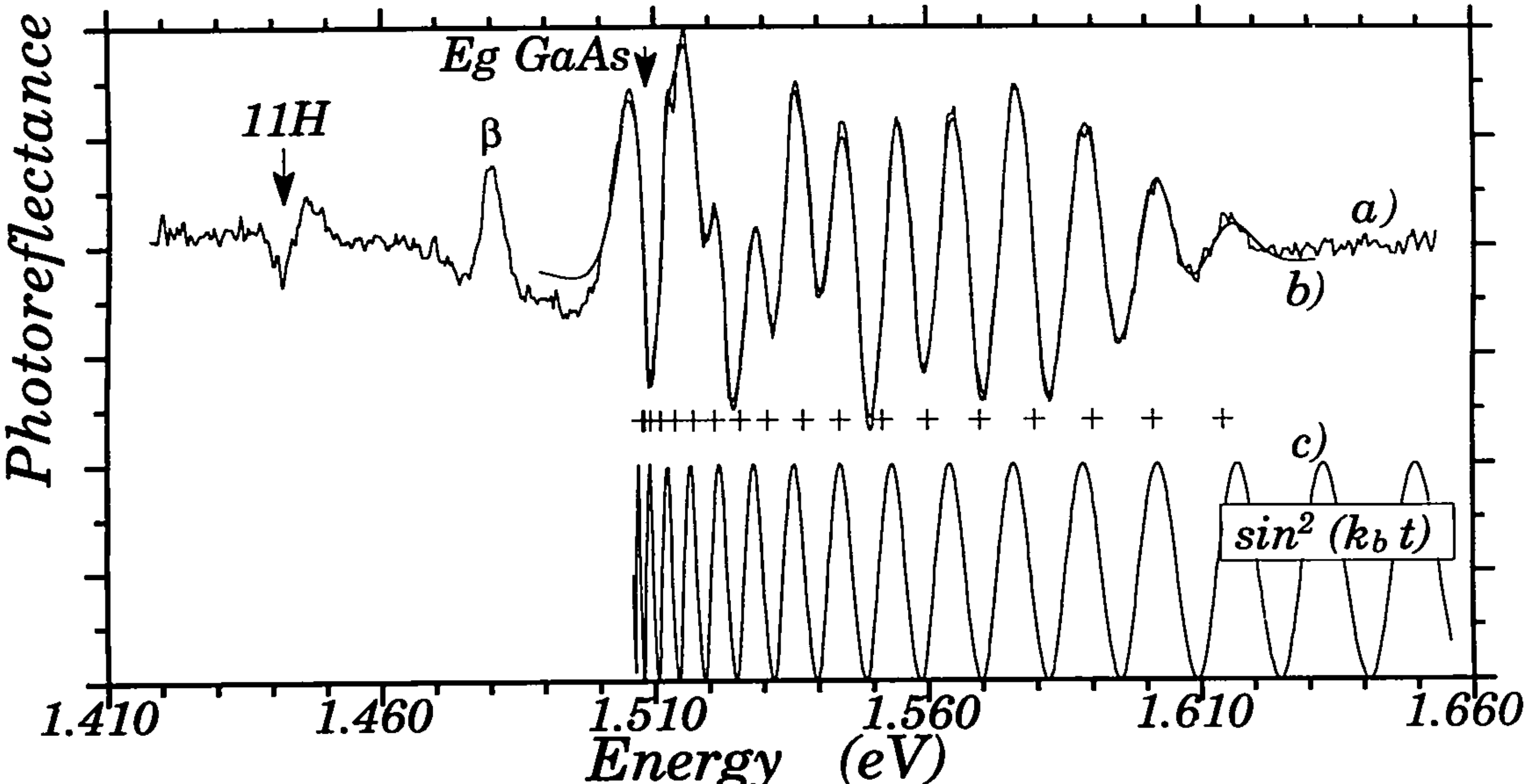

Fig. 3-12: a) PR spectrum at T = 77 K showing above barrier oscillations for an $In_{0.16} Ga_{0.84} As/GaAs$ SQW with a well width of 3.5 nm, a cap layer thickness of 50 nm, and a buffer of 1 μm. b) fit of the above gap PR oscillations using eq. (2-2) with the calculated transition energies marked by the crosses. c) $\sin^2(k_b t)$ for t = 44 nm and using the effective mass of the heavy hole ($m^*_b = m^*_{hh} = 0.37\ m_o$); $k_b = [2m^*_b(E-E_g^{GaAs})/\hbar^2]^{1/2}$.

which shows a 77 K PR spectrum. For energies below the band gap, an other feature labelled β is observed. It will be clear from the ER spectra of sect. 3-2-2 that this feature originates from two transitions involving the above bound states and some unbound (continuum) states (to be discussed with fig. 3-15 below). For energies above the GaAs gap (above the barrier), a series of oscillations appears. If one uses the model of a barrier of infinite spatial extent on each side of the SQW, the only quantum-well-related feature which could occur at above-gap energies would in this case correspond to a transition from the resonant continuum state of the heavy holes to the GaAs electron band edge at about 30 meV above the GaAs gap. The spacing between the extrema of oscillations is increasing as the energy increases. This is very different from the F.-K. oscillations, in which case the spacing between the extrema decreases as the energy increases (as seen previously in fig. 3-9). If one numbers the extrema consecutively as it is usually done for the F.-K. effect (see for example fig. 3-9 and 3-10 of sect. 3-1-3), instead of a $E_n = E_0 + \alpha\ (n - 1/2)^{2/3}$ dependence, one obtains a fit of the form $E_n = E_0 + \alpha\ n^2$: see fig. 3-13 curve i). If the heavy holes are mainly responsible for the oscillations, the slope obtained from this graph would correspond to a cap layer thickness of t = 44 nm according to eq. (1-13) which predicts $\alpha = \left(\frac{\pi^2\hbar^2}{8t^2m_b^*}\right)$ for the flat band condition. It is interesting to compare the results to a $\sin^2(k_bt)$ plot, for t = 44 nm, and where the heavy hole

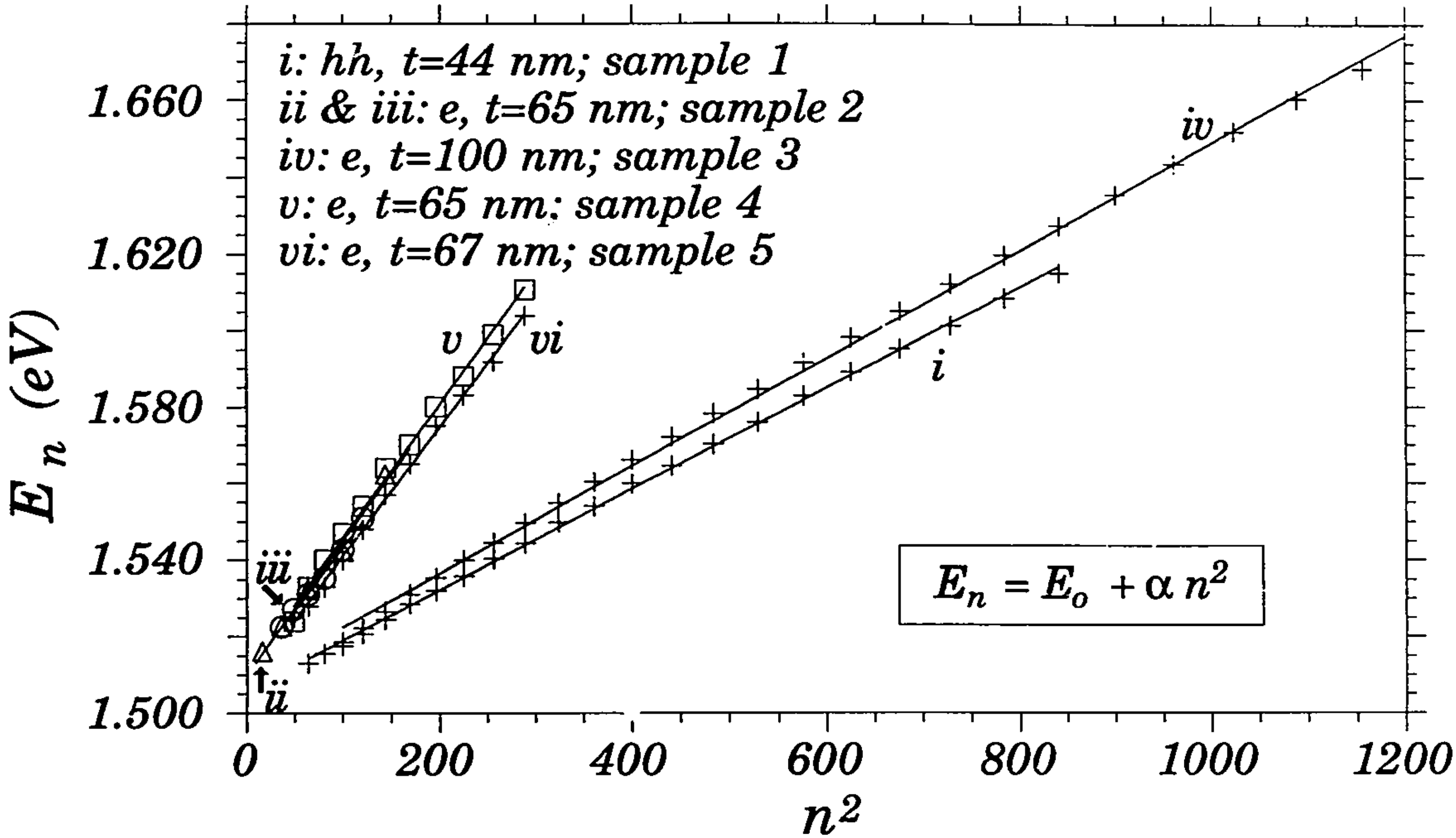

Fig. 3-13: Quadratic relationship between the energy positions (E_n) of the extrema and their index number (n) when the minima and maxima of the above-gap oscillations are numbered in a F.-K. fashion. The lines correspond to various samples as labeled on the figure. e = electrons; hh = heavy holes.

effective mass of GaAs enters in k_b: see curve c) of fig. 3-12, and compare with curve a). Considering the simple assumptions used in this simplified model, it reproduces quite remarkably the minima and maxima of the experimental PR spectrum throughout the range of oscillation; near the GaAs gap, the oscillations of curve c) of fig. 3-12 are very dense, and therefore may not have been resolved experimentally, or may be convoluted with weak FK oscillations resulting from a small residual electric field, or slightly modified by this small field through eq. (1-15). Furthermore, the apparent irregular variations in the oscillation pattern for energies around 20 meV above the gap may be associated to the node seen in the pattern of the oscillations of the probability of finding the heavy holes in the cap layer as seen in fig. 1-7a when $k_w L = \pi$ (i.e. where the regular SQW would have a resonant continuum state). Also the first few peaks of the oscillations of the electron continuum states (as seen in fig. 1-5) may be convoluted to those of the heavy holes.

The $\sin^2 k_b t$ factor modulates the probabilities of finding the carriers in the various regions, and thus it is expected to yield the positions of the extrema; the amplitude of the oscillations in the probabilities is found to decrease as the energy over the well increases as seen previously in fig. 1-7. However, the oscillations in the PR spectrum of fig. 3-12 seem to vanish more rapidly than predicted by the calculations.

This may be partly related to the penetration depth of the probing light which varies rapidly in this spectral range. The cap layer thickness found from the slope of a E_n vs n^2 plot is slightly different from the nominal value (also verified with SIMS measurements); this is likely a consequence of neglecting the actual line shapes in the PR spectrum when numbering the extrema. The exact positions of the calculated peaks of the well occupancy of the heavy holes predicted by eq. (1-10b) were shown in fig. 1-7. The corresponding energies are marked by the crosses in fig. 3-12, where the above-barrier transitions are from the peak of the oscillations of the well occupancy of the heavy hole continuum to the band edge of the electron continuum (or to the single electron bound state; however this can be ruled out since it would also result in oscillations at energies below the gap, which have not been observed). The PR line shape was fitted using eq. (2-2) with these values of energies (marked by the crosses) for the E_j's. To fit the data, the energies (E_j) and the order of the derivative ($m_j = 2.5$) were fixed, and the amplitudes (c_j), broadenings (Γ_j) and phases (θ_j) of the transitions were left as fitting parameters. The fit obtain with the E_j's calculated for a value of t = 50 nm is in excellent general agreement with the experimental spectrum: compare curve b) with curve a) of fig. 3-12.

As explained above, for larger t, it is expected that the contribution to the oscillatory spectrum should shift from the heavy hole to the electron continuum. To illustrate this case, sample 2 has a cap layer thickness of 67 nm and the same well width as sample 1. Fig. 3-14a displays the above-barrier PR results for this SQW sample (the below-gap results -not shown- were comparable to those obtained in fig. 3-12a, as expected for bound states related transitions). As in fig. 3-12, the crosses in fig. 3-14 show the theoretical positions, similarly to fig. 1-5b but for t = 67 mn, for the transitions which were used in eq. (2-2) to fit the line shape of the PR spectrum (see curve b). The E_n vs n^2 fit for this sample (fig. 3-13, curve ii), gives a slope which corresponds to a 67 nm cap layer if one uses the electron effective mass in eq. (1-13). As well, curve c) of fig. 3-14 showing a $\sin^2(k_b t)$ plot with k_b containing the electron effective mass, and t = 67 nm, can be compared to the experimental results of fig. 3-14 curve a. The agreement with the actual thickness confirms that for larger t, the type of carriers responsible for the observable oscillations changes from the heavy holes to the electrons.

Sect. 1-3 showed that, for barrier terminated samples (as is the case for the InGaAs/GaAs system), the contrast in the cap related quantum interference will be more pronounced for thin wells (such as the well width of samples 1, 2 and 3). The reason why the oscillations shown here are so strong (their amplitudes are even larger than the amplitude of the

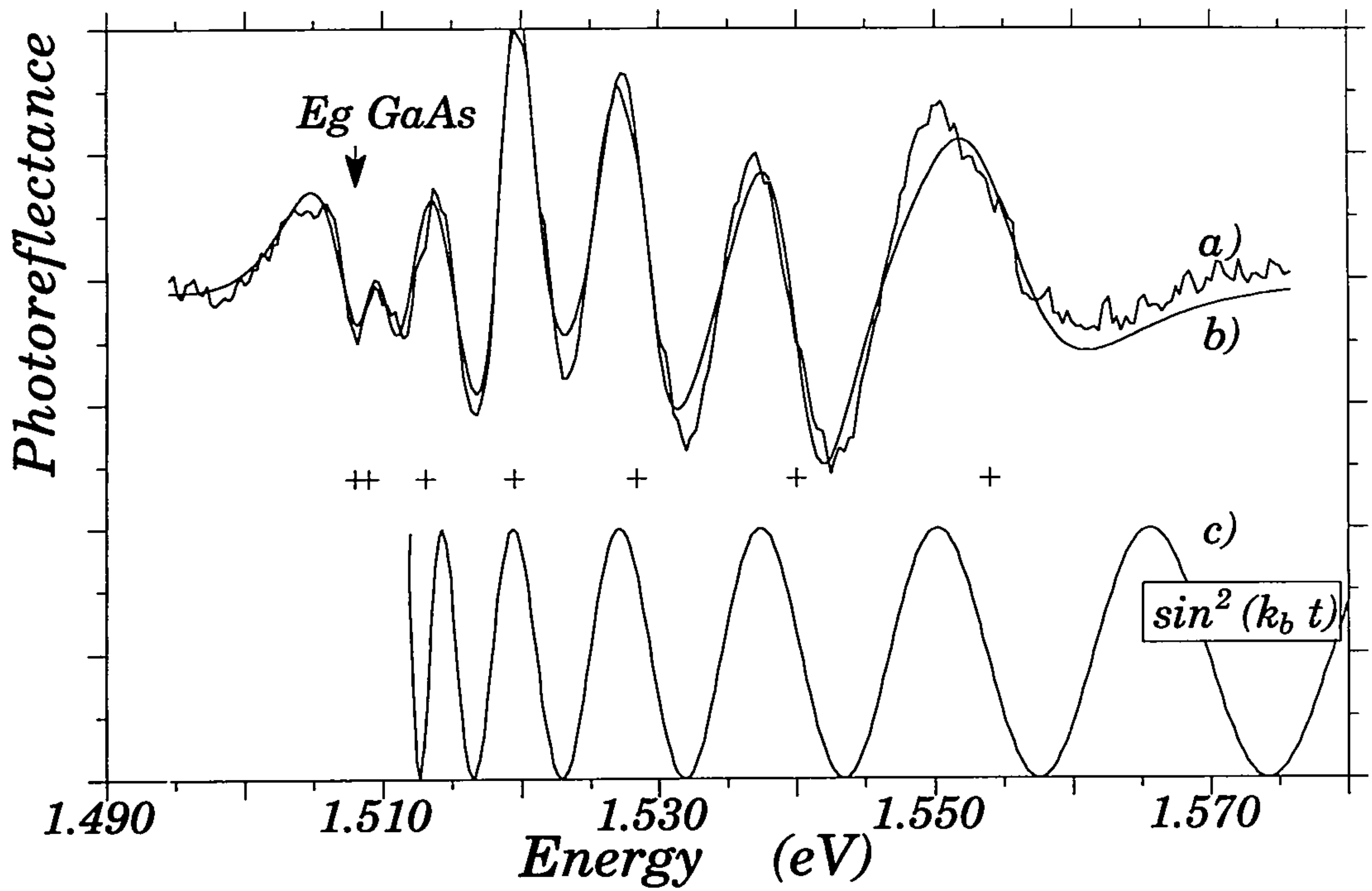

Fig. 3-14: Same as fig. 3-12 but for a cap layer of thickness of 67 nm; in c) t = 67 nm is used togetner with the electron effective mass ($m_e^* = 0.0665\ m_o$).

transitions involving bound states) is therefore a favorable combination of cap and well thicknesses, as well as the low intensity of the modulating light. Fig. 3-13 also shows the E_n vs n^2 plots obtained with samples having other well widths and/or cap layer thicknesses: the above-barrier oscillations in the PR spectra obtained with these samples were smaller in amplitude, and the ER results will be clearer, so that the cap-related oscillations obtained with these samples will be discussed more extensively in the next section.

3-2-2 With an electric field:

To study the influence of an applied electric field on the above-barrier oscillations attributed to the finite-size of the cap layer, ER experiments were carried out. The results for sample 1 are in fig. 3-15 for bias voltages from +1400 mV to -1400 mV by step of 200 mV in curves i to xv respectively. For positive bias the sample approaches the flat band condition, since the built-in field caused by the presence of the Schottky barrier at the surface is canceled by the applied voltage. Comparing the ER spectra of fig. 3-15 at positive biases with the PR spectrum of sample 1 in fig. 3-12, it is clear that the near flat band condition (as encountered in PR) occurs between curve v or curve vi, at a bias voltage of about +0.5 V. The spectra display features associated with the 11H peak, some intermediate transitions (previously labelled β in

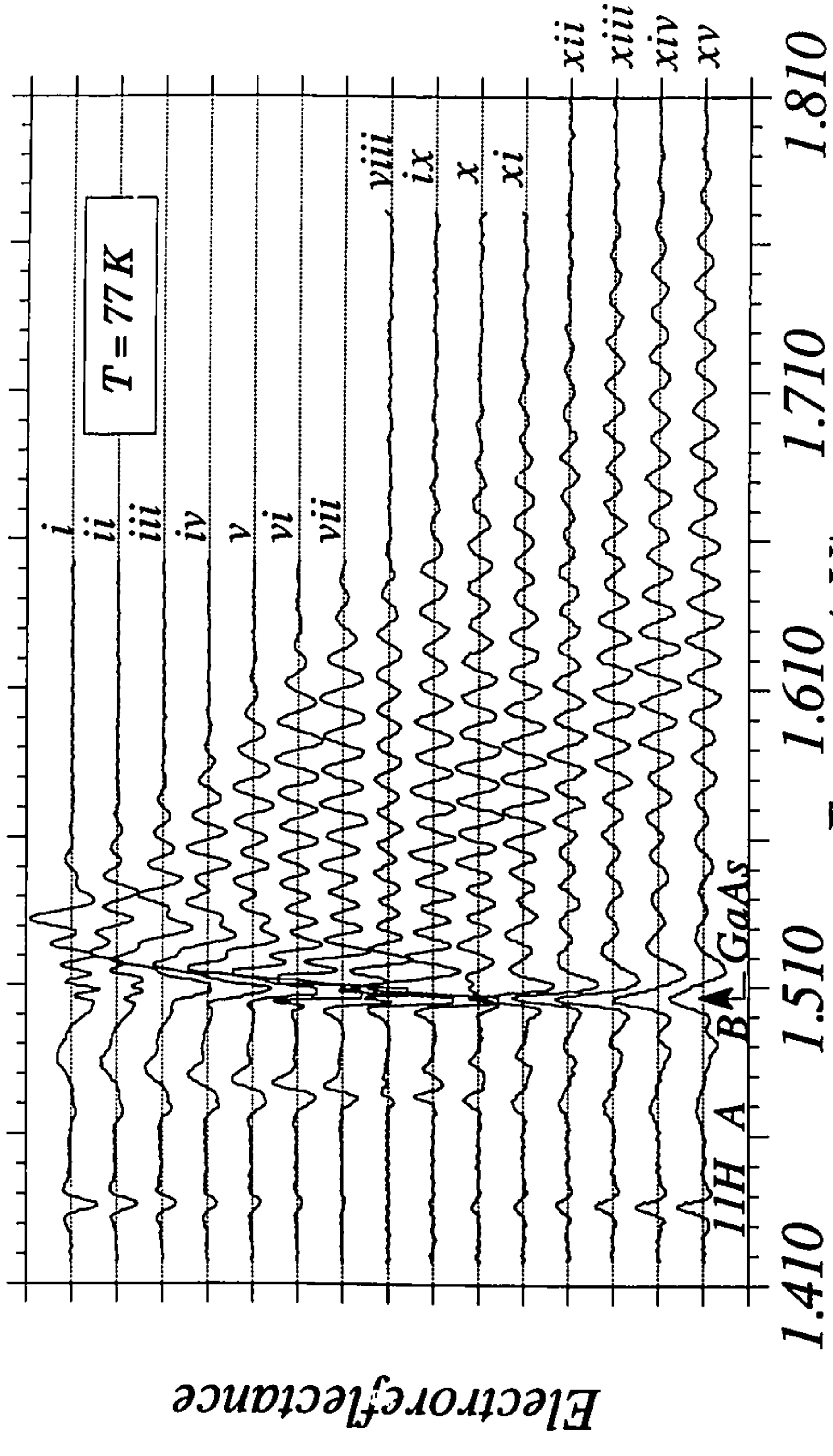

Fig. 3-15: ER spectra of sample 1 (with a cap of 50.0 nm), at T = 77 K, for bias voltages between 1.4 V (curve i) and -1.4 V (curve xv) by increment of 0.2 V.

fig. 3-12) labelled A and B , the GaAs gap, and the cap-related above-barrier oscillations. As the field is increased, the 11H peak is Stark shifted. The Stark shift for this sample is small because the well is narrow. Also the amplitude of the 11H peak evolves from a maximum at both extremities of applied voltages to a minimum for an applied voltage near 0 V. This could be explained by the leakage of the carriers from the well into the adjacent layers as the electric field tilts the bands. Also, from the gradual displacement with the applied voltage of the peak A and B in the ER spectra of fig. 3-15, it is clear that the intermediate feature labelled β observed in PR spectrum (fig. 3-12) was composed of at least two transitions (labelled A and B in fig. 3-15) which are separated with the electric field. From calculations, A is associated with the real-space indirect, bound-unbound 11L transition; and B, which is shifting towards higher energies as the field is increased, is associated with the e1-cH transition. The extrema of the cap-related above-barrier oscillations in fig. 3-15 are shifted with the electric field, and also the spectral energy range for which the experimental oscillations are visible increases with the electric field. This can be directly related to the electric field dependence of the cap-related oscillations in the probabilities of finding the carriers in the various regions as seen in fig. 1-9. Indeed, fig. 3-15 for the experimental results and fig. 1-9 for the calculations display similar behaviors: for example, for a fixed energy above the barrier, the amplitude of the oscillations of fig. 1-9 becomes larger for the stronger electric field; and the displacements in the extrema of oscillations are shifted towards higher energies. The latter shift for the well occupancy was found to be +2.9 meV/KV/cm in sect. 1-4 (see fig. 1-10). The shift predicted by calculations is slightly smaller than the value found experimentally, from fig. 3-15, ≈ 4.3 meV/KV/cm, probably because the actual potential configuration is not exactly that shown in fig. 1-8 due to non-uniformity in the field related to band bending near the surface.

For the same sample, it is interesting to compare the theoretical prediction of the variation of the well occupancy (P_w) as a function of the applied electric field for a fixed energy above the well, to the experimental results. Fig. 3-16a shows the calculated P_w as a function of the electric field for four different energies: 8, 9, 10, and 11 meV above the edge of the well. This is compared to the experimental ER signal obtained at fixed wavelength (fixed energy above the well) as the bias voltage is varied (fig. 3-16b). It is difficult to compare the two quantitatively because the actual values of electric field are not known since the built-in field cannot be evaluated for this sample; nevertheless it is clear that qualitatively the experimental results vary as theoretically expected.

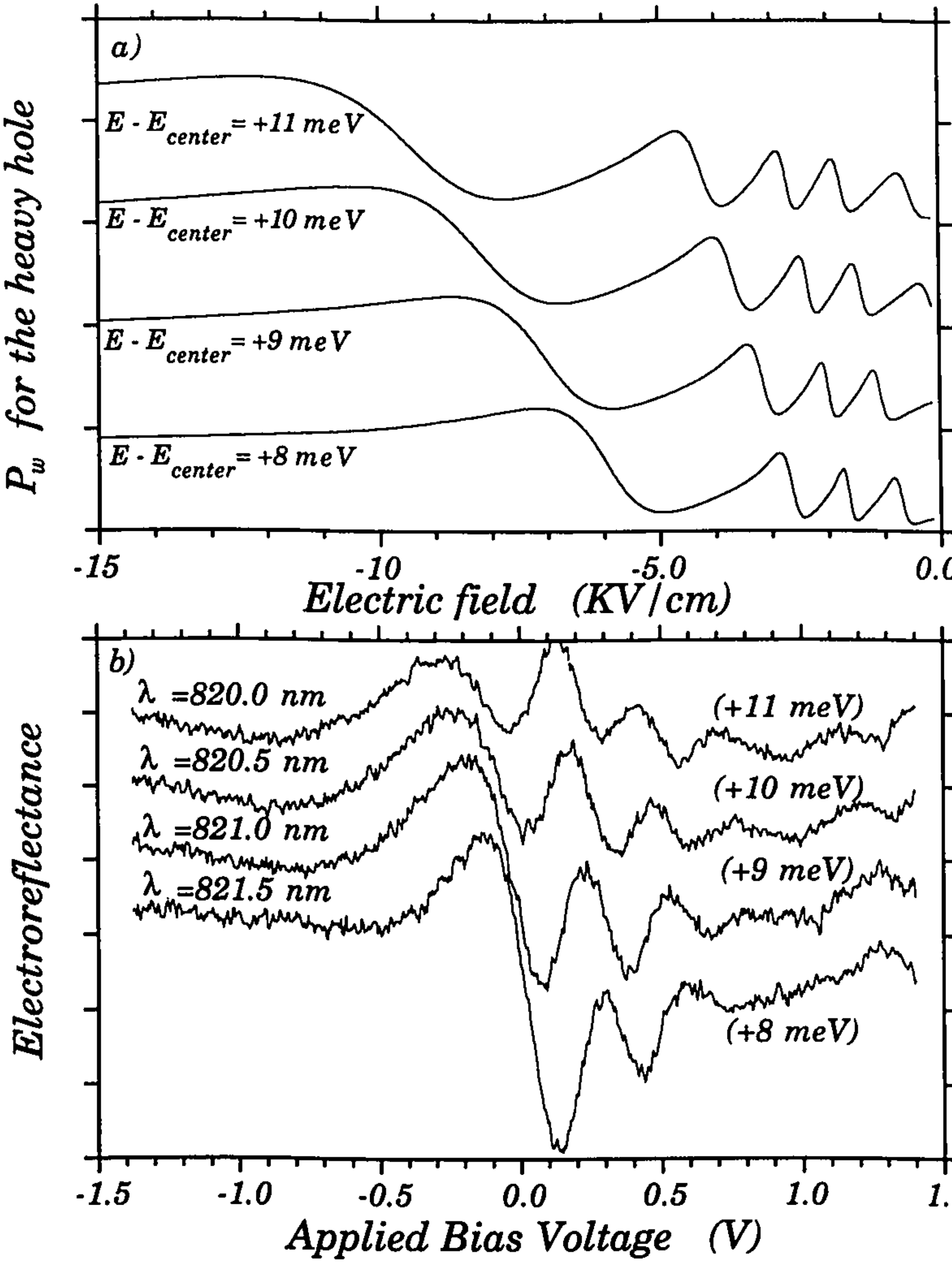

Fig. 3-16: a) Calculated electric field dependence of the well occupancy (P_w) for a fixed energy above the center of the well (8, 9, 10, and 11 meV). b) ER measured at fixed wavelengths (8, 9, 10, and 11 meV above the barrier) as a function of the applied bias for sample 1.

Since the non-Franz-Keldysh above-barrier oscillations are related to the size (thickness) of the cap layer, they are not expected to be strongly influenced (i.e. shifted in position relative to the other spectral features) by the temperature. Fig. 3-17 shows the ER results of sample 1 obtained at various temperatures, for a bias voltage of -1.0 Volt (i.e. curve xiii of fig. 3-15); the horizontal axis represents the energy measured from the 11H peak. The 11H peak itself was shifting as expected with temperature[HQ91,V67]. It is clear from fig. 3-17 that as expected the temperature does not affect substantially the positions of the peaks.

The ER results obtained with sample 2 are shown in fig. 3-18 for bias voltages from +1400 mV to -1400 mV by step of 200 mV in curves i to xv respectively. As expected, for energies smaller than the gap, the spectra are similar to that of fig. 3-15 for sample 1 which had the same well width. However, the above-barrier oscillations are very different from those of the previous sample which had a different cap layer thickness. The PR spectrum of fig. 3-14 had demonstrated that as expected the carriers contributing to the observable oscillations changed from the heavy holes to the electrons as the cap layer thickness is increased. This was expected from the m_b^* dependence of eq. (1-13). The ER spectra of fig. 3-18 also show the spectral oscillations which are related to the variations in the well occupancy due to the electrons for a

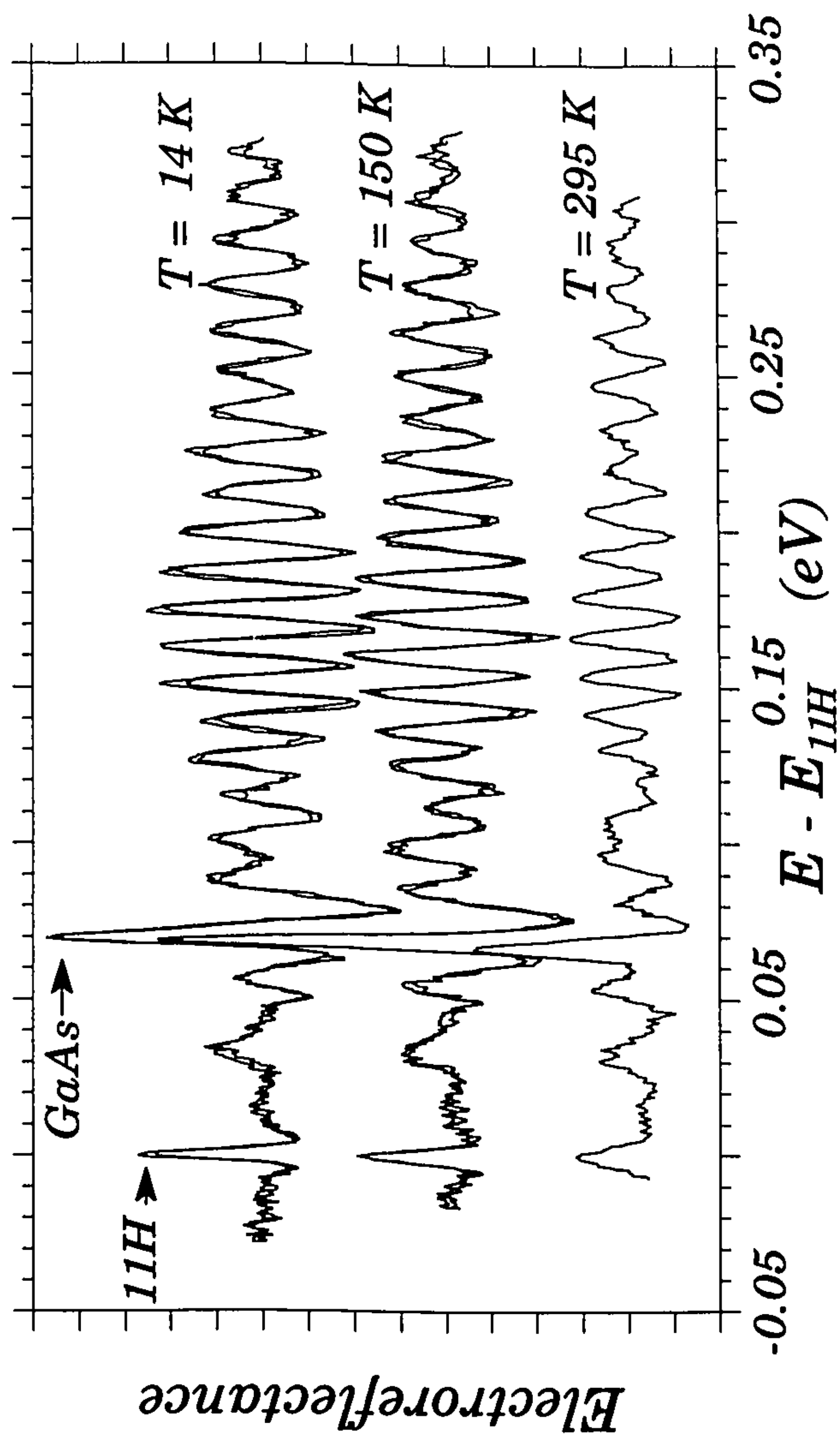

Fig. 3-17: ER spectra of sample 1 (L = 3.5 nm, t = 50 nm) for different temperatures. The horizontal axis is the energy measured relative to the 11H peak. The spectra were all obtained at a bias voltage of -1.0 V. The first two spectra have been scanned twice, the bottom one is the average of several scans.

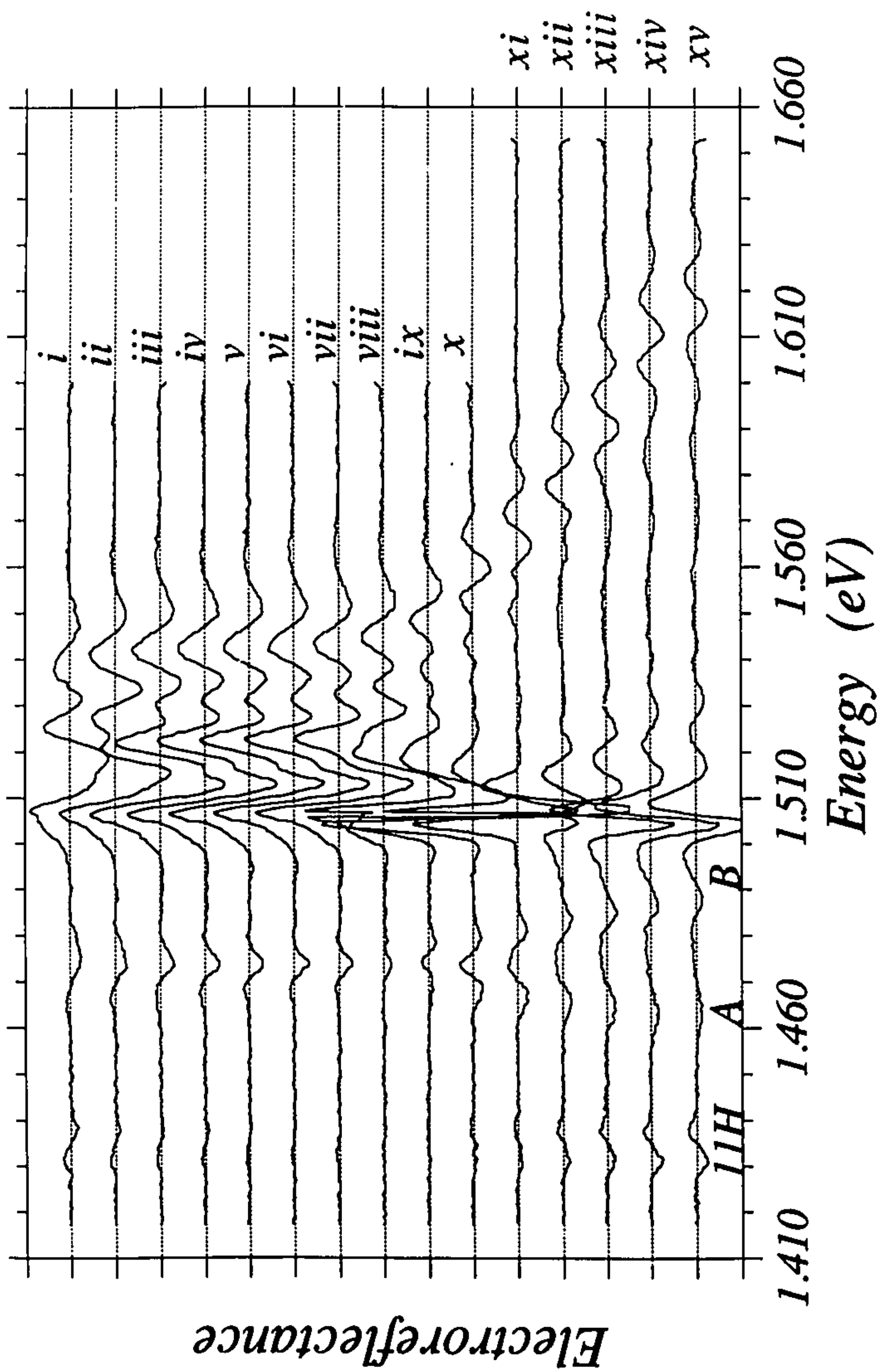

Fig. 3-18: ER spectra of sample 2 (with cap of 65.0 nm), at T = 77 K, for bias voltages between 1.4 V (curve i) and -1.4 V (curve xv) by increment of 0.2 V.

cap thickness of 65 nm: Fig. 3-13 curve iii) shows the E_n vs n^2 plot for this sample, obtained from the ER spectra curve v) of fig. 3-18 (at a bias voltage of +600 mV near the flat band condition). The values of the cap layer thickness obtained from the slope are in good agreement with the growth parameters and with the one found from the PR spectrum of fig. 3-14. As the voltage is changed toward the negative biases, the extrema of oscillations are shifting quite rapidly with the increasing electric field (≈ 6 meV/KV/cm). Indeed, from sect. 1-4 a larger shift is expected for a thicker cap layer (for example, for that sample, the edge of the well would be displaced by 6.9 meV/KV/cm).

Sample 3 (same well width as sample 1 and 2) which has a cap layer thickness of 100 nm will further verify that according to eq. (1-13), the oscillations of the continuum states will depend on the cap layer thickness t. The ER results of sample 3 are shown in fig. 3-19, for bias voltages between +1200 mV and -1400 mV by step of 200 mV, corresponding to curve i to xiv respectively. Once again the below gap results are similar to those obtained with the other two samples having well widths of 3.5 nm. The ER spectra obtained near the flat band condition, give oscillations which correspond to the electrons for a cap layer thickness of 100 nm. For example, the energy positions of the extrema of oscillations for that sample are plotted in a E_n vs n^2 in fig. 3-13 curve iv), and

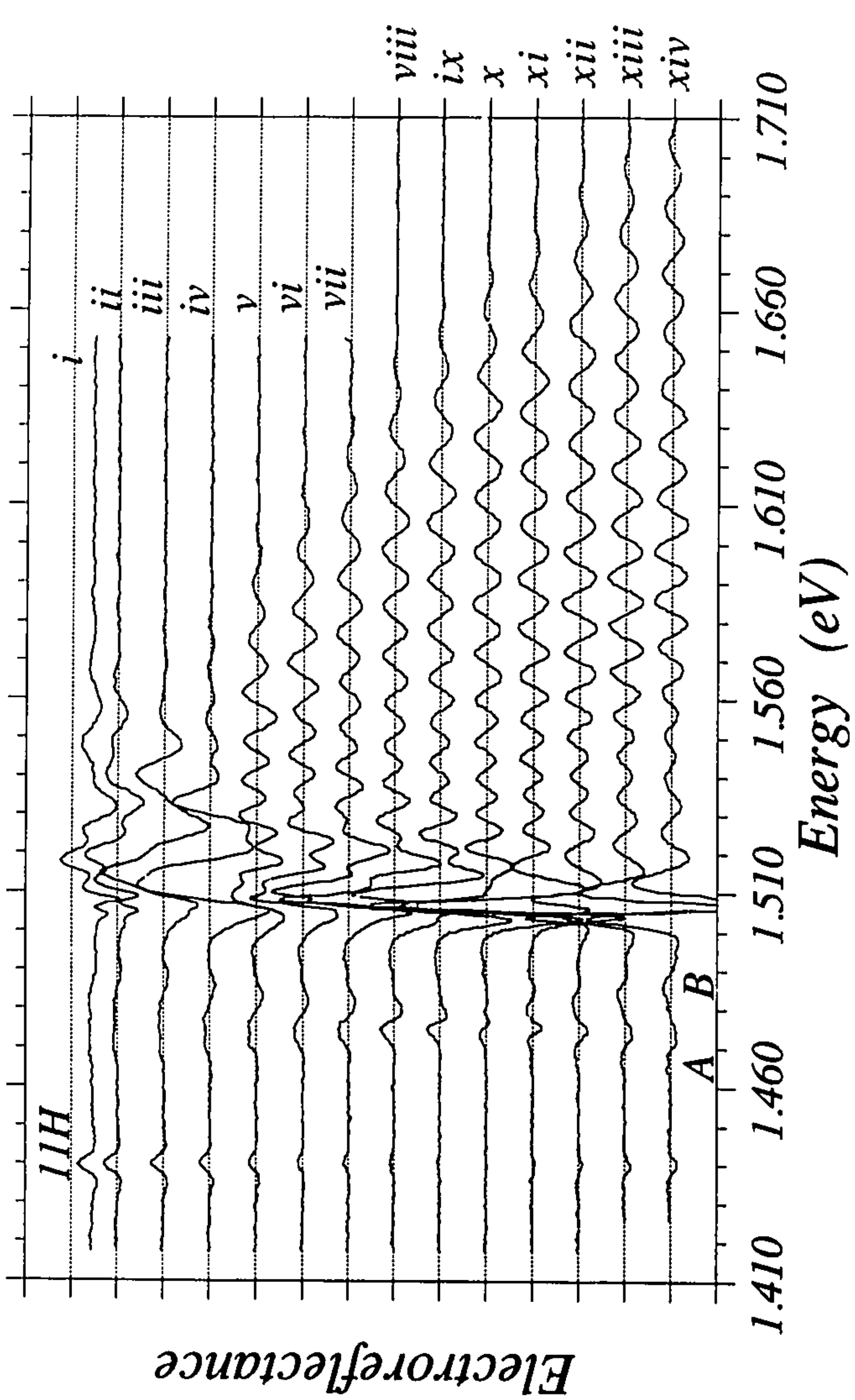

Fig. 3-19: ER spectra of sample 3 (with a cap of 100.0 nm), at T = 77 K, for bias voltages between 1.2 V (curve i) and -1.4 V (curve xiv) by increment of 0.2 V.

the slope obtained is in good agreement with a cap layer thickness of 100 nm for an electron contribution. However, for this sample the shift of the extrema of oscillations with the electric field is quite different from what would be expected for the potential configuration shown in fig. 1-8. The extrema are displaced by ≃ 3.5 meV/KV/cm, whereas for example, the edge of the well would be shifting quite rapidly (10.4 meV/KV/cm), and so one would expect a larger shift than the one observed. Also, the spectra at large positive bias seem to have a structure in the vicinity of 30 meV above the barrier, which could be associated to the usual resonant continuum states of the heavy holes. This seems to indicate that for large enough cap layer thicknesses, the usual resonant continuum states become more significant, whereas for thinner cap layers, the quantum interference created by the finite size of the cap layer would dominate the spectra under certain conditions.

The first three samples, which had a well width of 3.5 nm, gave strong cap-related above-barrier oscillations as expected for narrow wells. The last two samples studied here have larger well widths, and gave above-barrier oscillations which were weaker relative to the other spectral features. Sample 4 has a nominal well width of 12.0 nm and a cap layer width of 65 nm. According to fig. 1-4, this sample would have two bound electron levels, and three bound heavy hole levels. The ER spectra are shown in fig. 3-20, curve i to xiv are for bias voltage from +1200 mV to -1400 mV by step of 200 mV respectively. As usual, the peak labelled 11H is the transition between the first level of the electrons and of the heavy holes, and the feature associated with the gap is labelled GaAs. This sample shows only very weak cap-related above-barrier oscillations, not visible at first observation; however it will be shown below (in fig. 3-24) that these oscillations are actually present. For energies above the GaAs gap, the spectra of the last two samples are dominated with Franz-Keldysh oscillations, especially for the negative biases. From a E_n vs $(n - 1/2)^{2/3}$ plot obtained with the F.-K. oscillations, one can calculate the electric field for the different bias and use these values to calibrate the field as a function of the applied bias, as was done in sect. 3-1 fig. 3-9 and 3-10;for example curve xiv in fig. 3-20 at -1400 mV, corresponds to an electric field of 20.7 KV/cm. Furthermore, the dependence of the electric field on the applied voltage gives a direct measurement of the thickness of the undoped regions across which the voltage is applied, and of the built-in electric field (as was done in sect. 3-1 fig. 3-11). It is found from fig. 3-20 that the electric field varies linearly with the applied voltage correspondingly to a 0.8 μm undoped region (the difference with the thickness expected from the growth parameters (1.08 μm) is probably due to non-uniformity in the applied field); the built-in electric

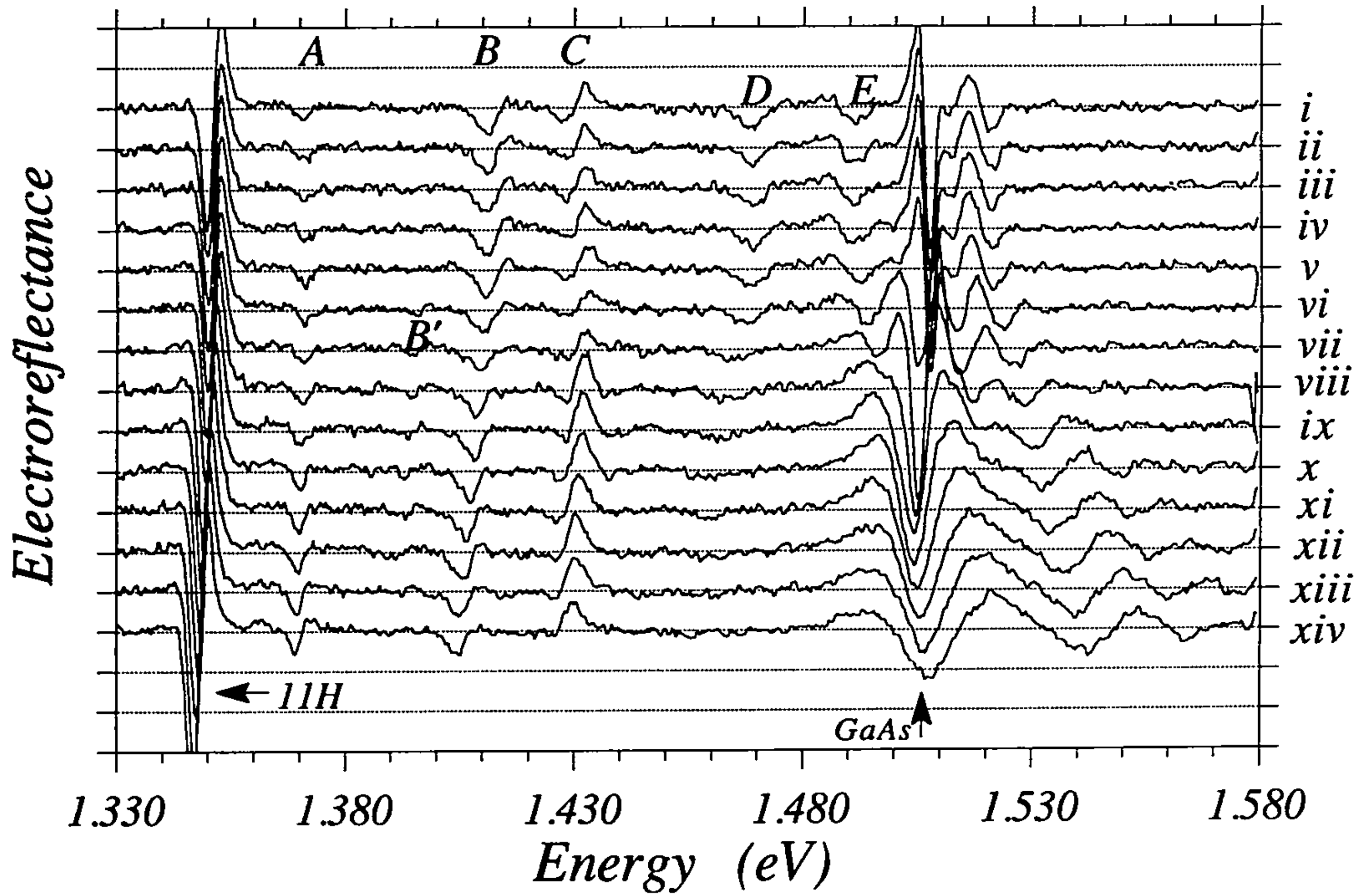

Fig. 3-20: ER spectra of sample 4 (with L = 12.0 nm, and t = 65.0 nm), at T = 77 K, for bias voltages between 1.2 V (curve i) and -1.4 V (curve xiv) by increment of 0.2 V.

field is 3.0 KV/cm, which means that the electric field should be zero at ≈ 240 mV, i.e. between curve vi and curve v.

Several features are observed between the 11H peak and the GaAs gap. From standard calculations, the labelled peaks could be assigned to: A: 12H, B′: 13H, B: 11L and/or 21H, C: 22H, D: 21L and/or 23H, and E: ec-3H. Where as usual, ijH denotes the transition between the i-th electron state to the j-th heavy holes states; i1L here denotes a transition between the i-th electron state and the unconfined light holes at the GaAs valence band edge in the cap or buffer regions; and finally ec-jH would be a transition between the GaAs conduction band edge and the j-th heavy hole level. One also notes that the various peaks are Stark-shifted as the electric field is changed. For example, fig. 3-21 displays the shift of the 11H peak position (found from lineshape analysis as described in sect. 2-3) as function of the applied voltage.For the range of electric field studied here, the total shift in energy of the 11H peak is 3.5 meV, and seems to behave as expected in a quadratic fashion[BB91] as shown by the solid line in fig. 3-21. The energy variations of the other peaks of fig. 3-20 are less pronounced, except "E" which seems to shift in a peculiar way: it is strongly displaced toward higher energies as the magnitude of the electric field is increased. The behavior of this feature will be discussed further in connection with similar peaks observed with the next sample. Also the amplitude of

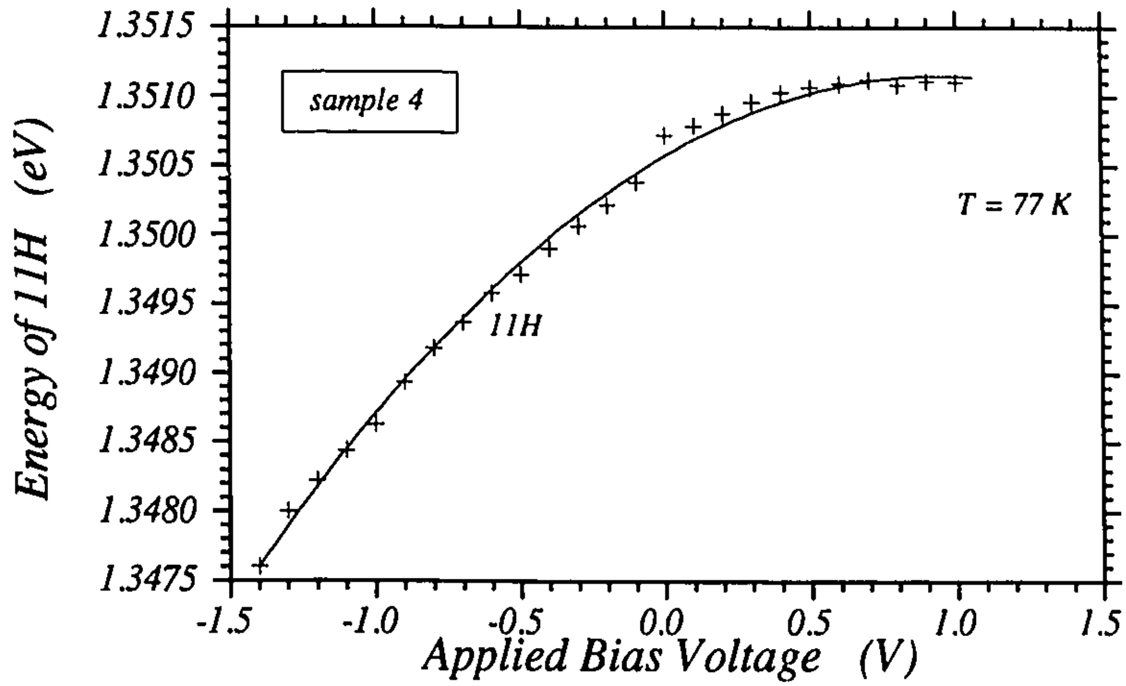

Fig. 3-21: Stark shift of the 11H transition for sample 4. The crosses are the values obtained using eq. (2-2) to fit the lineshape of the ER spectra of fig. 3-20, and the solid line shows the quadratic relationship.

some features is changing with the applied electric field: for example "A" which is associated with a transition forbidden in absence of field (12H is odd-even parity), seems to strengthen as the magnitude of the field is increased (i.e. toward negative applied voltages); and peak B' which is allowed in zero-field (13H odd-odd parity) is weak, and almost only observable for applied voltage close to the zero-field situation. All these amplitude variations related to the parity of the transitions are expected from symmetry consideration of the carriers wavefunctions[W87].

Sample 5 has a nominal well width of 8.0 nm, and a cap layer thickness of 65 nm (same as sample 4 and 2). According to fig. 1-4, this sample should have two electron and two heavy hole bound states. The ER results for this sample are shown in fig. 3-22; curve i to xv are for bias voltages from +1400 mV to -1400 mV by step of 200 mV respectively. The results are similar to those of the previous example except that fewer transitions are observed in the energy range between the 11H peak and the GaAs gap, as expected since this sample has two instead of three confined heavy hole levels. Here again the spectra are dominated by the Franz-Keldysh oscillations at above-gap energies especially for negative biases, but it will be seen below (fig. 3-24) that this sample also contains some weak cap-related above-barrier oscillations. As with the previous sample, the F.-K. oscillations were used to calculate the electric field values for the different applied voltages, and from the dependence of the electric field on the applied voltage, it was found with this sample that the undoped region was 1.2 μm thick (again compare with the nominal value of 1.07 μm); and that the net built-in electric field was 1.0 KV/cm. And so for example, the electric field is 12.5 KV/cm for curve xv at -1400 mV, and would be zero at $V_a \simeq 120$ mV (i.e. between curve vii and viii). The below-gap assignment for the features at energies above the 11H peak, is as follow: A: 12H, B: 11L,: C: 21H and/or ec-1H, D: 22H. As before, the amplitudes change with the electric

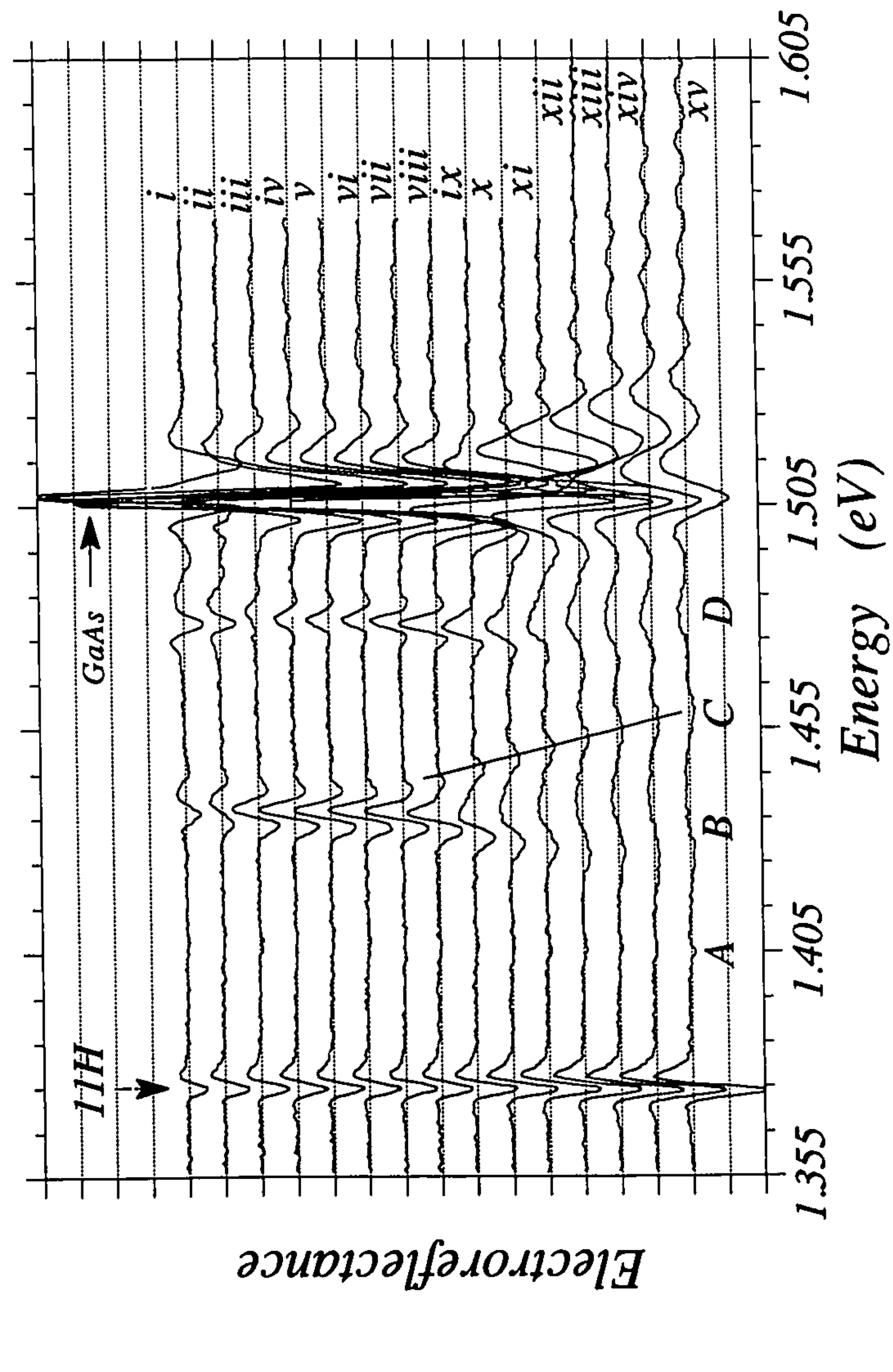

Fig. 3-22: ER spectra of sample 5 (with L = 8.0 nm, and t = 65 nm), at T = 77 K, for bias voltages between 1.4 (curve i) and -1.4 (curve xv) by increment of 0.2 V.

field, and the peaks are shifted in energy. Once again, peak A (12H), strengthens as the electric field is increased, and peak D (22H) is stronger near the zero field situation, following the selection rules. The shifts in energy of the 11H, B, and C peaks with the electric field are plotted in fig. 3-23. The total shift (1.0 meV) of the 11H peak is not as large as the one obtained with sample 4, because of the smaller range of electric field covered, and because of the different well width giving a different Stark shift, but the functional relationship seems to be quadratic here again. Peak B is also shifting towards smaller energies in a similar fashion, and becomes convoluted with peak C for positive bias. It is quite remarkable to observe the peculiar shift of peak C, which is similar to the one observed with the previous sample (peak E, fig. 3-20). When compared to the usual Stark shifts, it shows a much stronger displacement (here 21 meV) toward *increasing* energies (instead of decreasing), and it is *linear* (instead of quadratic) with a slope of 1.5 meV/KV/cm before saturating as the electric field approaches to zero. This type of shift is too large and has the wrong functional field dependence to be accounted for by the Stark effect alone. It could be argued that the peak B and the shifting peak C are just a single transition which broadens with the electric field, but this is unlikely because the broadening would be asymmetric, and exaggeratedly large (no such broadening has been observed with other transitions). It could

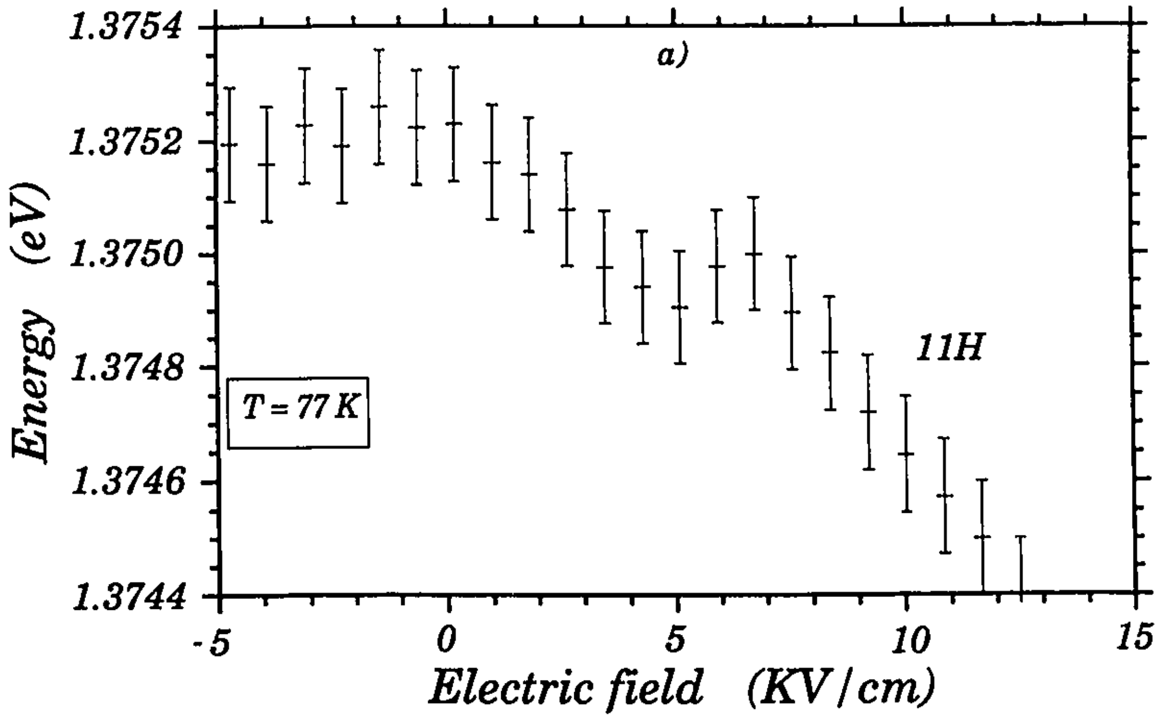

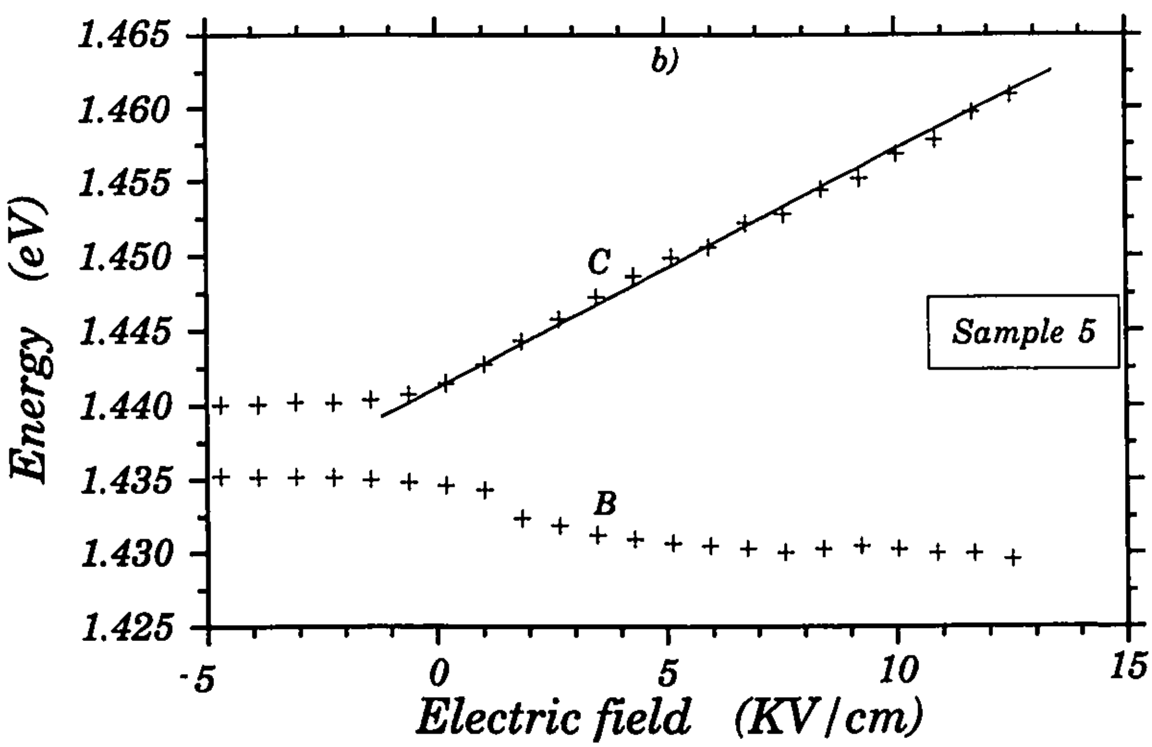

Fig. 3-23: a) Stark shift of the 11H transition , b) shift in energy of the intermediate transitions labeled B and C in fig. 3-22; for sample 5 at T = 77 K.

also be argued that the shift is in reality an exchange of amplitude between two transitions as the electric field is varied, but the continuity of the gradual displacement between consecutive spectra and the quality of the lineshape fit (not shown) obtained using eq. (2-2) with just a single transition favor the hypothesis that "C" is the result of just one transition with a strong positive shift. Moreover, the transitions which are believed to give the peaks with the peculiar shifts involve continuum states in all cases: the electron continuum states for peak E of fig. 3-20 (sample 4) and for peak C of fig. 3-22 (sample 5), and the heavy holes continuum states (e1-cH) for peak B of fig. 3-15, 3-18 and 3-19 for samples 1 to 3. These large positive shifts may be understood recalling that the continuum states are strongly affected by the finite-size of the cap layer and the high potential at the surface. The carriers in the continuum states should relax to the first peak of the well occupancy (or equivalently, of p_t/p_{box}) which is shifting toward higher energies as the field is increased, and so the transitions involving the continuum states would be displaced accordingly. Calculations based on eq. (1-12) and (1-11), (or see fig. 1-9) showed these large, positive and quasi-linear shifts with the electric field: ~1 meV/KV/cm, and 1.4 meV/KV/cm for electron continuum states for a cap layer thickness t = 65 nm and well widths of 12.0 nm and of 8.0 nm respectively. The value of the shift obtained experimentally with sample 5 (1.5 meV/KV/cm) compares particularly well with the calculated value of 1.4 meV.

The last two samples (4 and 5) having a larger well width, with a cap layer thickness of 65 nm, did not show strong cap-related above-barrier oscillations. Nevertheless, it should be possible to observe the oscillations corresponding to a cap layer of 65 nm for the electrons for these samples. Indeed, repeated slow scan at higher sensitivity of the positively biased ER spectra showed these oscillations. Fig. 3-24 displays the results obtained with sample 4 and 5, together with spectra v) of fig. 3-18 for sample 2, for comparison. It is clear from fig. 3-24 that all the sample having a cap layer thickness of 65 nm, sample 2, 4 and 5, gave oscillations with extrema at similar energies, only the amplitude of the oscillations of the samples having wider wells is smaller. The E_n vs n^2 plot for the oscillations extrema of sample 4, 5 are plotted in fig. 3-13 curve v, and vi respectively. It is clear that all samples with a cap width of 65 nm have similar slopes, which correspond to oscillations due to the electrons.

It is interesting to consider the amplitude of the 11H peak, relative to the other spectral features, for all 5 samples (see fig. 3-15, -18, -19, -20, and -22). The first 3 samples having a well width of 3.5 nm had small 11H peak, and the amplitude seems to increase as the well width is

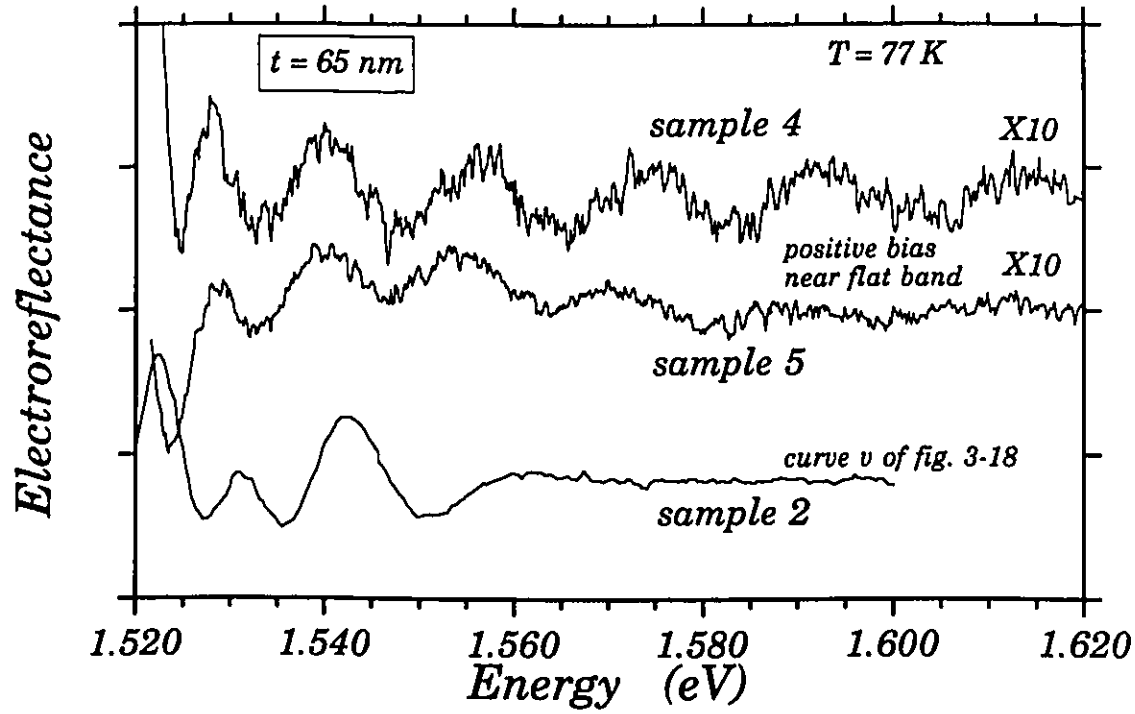

Fig. 3-24 ER spectra at high sensitivity of sample 4 and 5 (compared with spectrum of sample 2 which has the same cap layer thickness) showing the cap-related above-barrier oscillations.

increased. Sample 4 with L = 12.0 nm has the largest 11H peak. Indeed, for an equal well depth, it is plausible that the capture efficiency of the well improves if the well are wider[HQ91]. This seems to indicate that there is a well width dependent trade off between the continuum states and the bound states: narrow wells display strong continuum states features and weaker bound states related transitions, whereas the opposite is true for larger well.

In sect. 3-2, PR and ER have proven to be excellent techniques to verify the theoretical model of chapter 1 for the SQWs having cap layers of finite extent, in the flat band condition and with an applied electric field respectively. These techniques are not significantly influenced by the underlying substrate layer, as may be the case for the luminescence which may necessitate a sequential study as in sect. 3-1. To complete the study, chapter 4 will extend the SQW model of chapter 1 to deal with MQW and will present experimental results obtained with a MQW sample.

CHAPTER 4

MULTIPLE QUANTUM WELLS (MQWs)

4-1 Theory for the bound states.......................... 131

4-2 Theory for the continuum states...................... 141

4-3 Experimental results................................. 146

The case of a SQW is studied theoretically in chapter 1, and experimental results obtained with SQW samples are presented in chapter 3. The main conclusion from these chapters was that the SQW continuum states were very much affected in structures having relatively thin cap layers. The physical properties of MQWs are generally enhanced by the presence of the additional wells. And so, there is a great interest for devices based on MQWs for practical applications, and for the study of the basic physics involved in such structures. Therefore, chapter 4 will extend the model of the SQW of chapter 1 to deal with MQWs. The theory developed here for the bound states will consider a finite MQW structure with a finite number of wells, and with a cap layer of finite size. For the continuum states, similar to what was done in chapter

1, a particular attention will be given for structures with finite cap layers. Finally, chapter 4 will present experimental results obtained with a MQW sample having the same well width, alloy composition, and cap layer thickness as sample 5 of chapter 3. And so it will be possible to directly compare the experimental results obtained with the MQW, with those of the SQW. Such a comparison will help to understand the changes induced by the presence of additional wells on the cap-related quantum interference in the continuum states.

4-1 Theory for bound states:

It is a common practice to apply the known theory of superlattices to MQWs having only few wells, even though one of the assumptions at the basis of the theory of superlattice is that there is an "infinite" number of wells so that the cyclic boundary condition is satisfied. Therefore, at the beginning of the present section, the superlattices theory will be applied to an InGaAs/GaAs system to give an example of what type of results are expected in the case of superlattices for that system. The theory for MQW structures with a finite number of wells an a finite cap layer thickness will then be presented; and examples will be given on the evolution of the bound states as the number of wells and/or the cap layer thickness are changed. It is then possible to compare the exact results expected for a MQW with those obtained assuming a superlattice.

Let us consider a MQW composed of n (n > 1) wells (width L, depth V) separated with barriers of thickness d, or the corresponding superlattice (i.e. $n \to \infty$). Depending on the value of d (and of the effective mass of the semiconductor forming the barrier) the wavefunctions of the individual wells may overlap with the wavefunction of the adjacent wells. For large enough d (typically few ten nanometers), the overlap is not significant, and the MQW will have n degenerate bound states having the same energy as the corresponding SQW. For thinner d, the degeneracy is lifted, and the MQW or the superlattice will accommodate n bound states having different energies, in the vicinity of the energy of the SQW bound state. The thinner the barrier is, the larger the energy difference will be between the lowest and the highest of these n levels. This gives rise to mini-bands[MDW90,MDR90] (and therefore mini-band gaps) in the case of superlattices (i.e. $n \to \infty$). The width of the superlattice mini-band can be evaluated theoretically using Bastard's equation[W87,BB91] (i.e. an equation from a Kronig-Penney model[L80]):

$$\cos k_w L \cos k_b d - 1/2\ (\xi + 1/\xi) \sin k_w L \sin k_b d = \cos q(L+d) \tag{4-1}$$

where k_w, k_b, and q are the well, barrier, and superlattice wavevectors respectively, and $\xi = k_b m^*_w / k_w m^*_b$. The mini-band

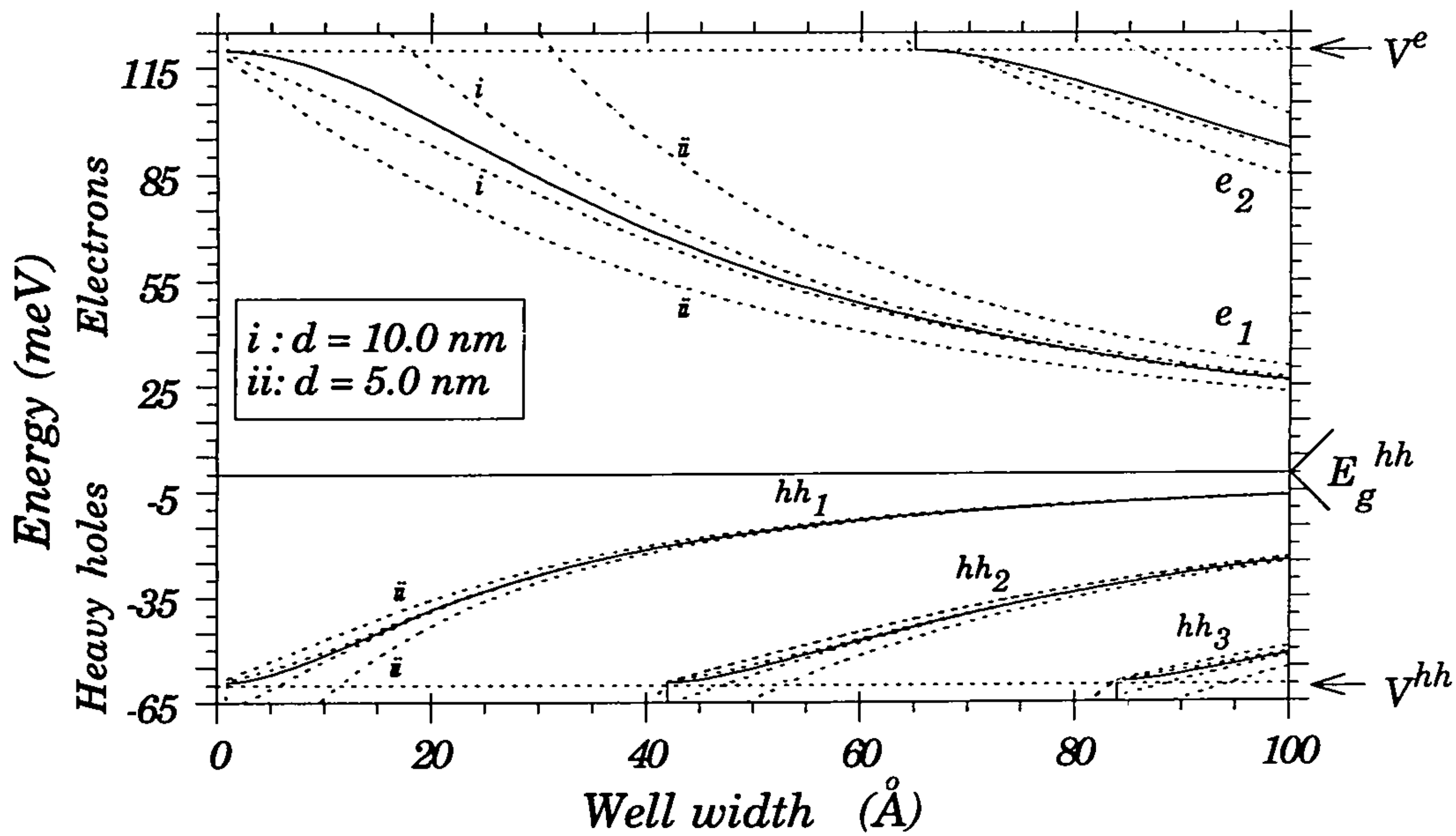

Fig. 4-1: Calculated well width dependence of the electron (top) and heavy hole (bottom) minibands of $In_{0.16}Ga_{0.84}As/GaAs$ superlattices for barrier thicknesses of 10.0 nm (i) and 5.0 nm (ii), the solid lines are for the corresponding SQW. For more details about the labels, refer to fig. 1-2 or 1-4.

width obtained by solving eq. (4-1) is the largest value that the energy difference between the highest and lowest of the n levels of the MQW can take. And so it is instructive to solve eq. (4-1) for an $In_{0.16}Ga_{0.84}As/GaAs$ superlattice system. Fig. 4-1 displays the well width dependence of the bound states of the corresponding SQW (or the isolated MQW), together with the bandwidth associated with superlattices having barrier thicknesses of d = 10.0 nm and 5.0 nm. As expected by considering the overlap of the wavefunctions, superlattices with thin barriers, higher lying energy levels, or light carriers (the electrons), will have larger bandwidths.

For most applications, satisfactory accuracy is achieved in evaluating the bound states of a MQW by finding the energy level(s) of the corresponding SQW, and then finding the bandwidth of the corresponding superlattice as discussed above. However, if the exact energy positions of the bound levels of the MQW are desired, one must solve the Schrödinger equation for the band diagram depicted in fig. 4-2, considering the exact number of wells, and also the finite-size of the cap layer:the wavefunctions in the cap and buffer layers are denoted by Φ_{cap} and Φ_{buf}; Φ_i^w denotes the wavefunction in the i-th well, and Φ_i^b is for the wavefunction in the i-th barrier (i.e. the barrier to the right the i-th well). Taking x = 0 at the cap/first well interface gives:

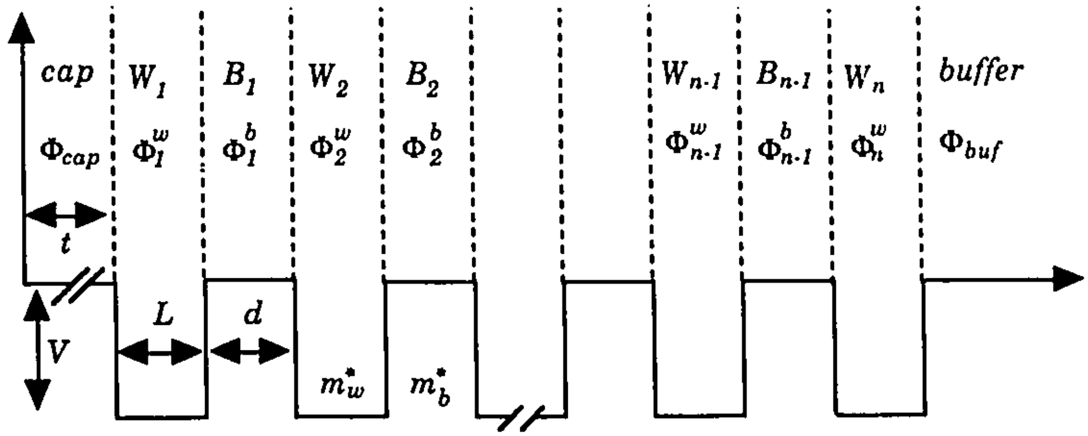

Fig. 4-2: Band diagram of a MQW with n wells of width L and depth V, separated with barriers of thickness d.

$$\Phi_{cap} \alpha \frac{\sinh k_b(x+t)}{\sinh k_b t} \quad \dagger$$

$$\Phi_i^w = a_i^w \sin k_w[x-(i-1)\times(L+d)] + b_i^w \cos k_w[x-(i-1)\times(L+d)],$$

$$\Phi_i^b = a_i^b \sinh k_b[x-L-(i-1)\times(L+d)] + b_i^b \cosh k_b[x-L-(i-1)\times(L+d)].$$

$$\Phi_{buf} \alpha e^{-k_b x}. \tag{4-2}$$

The wavefunction and its derivative divided by the relevant effective mass are matched at all the interfaces of the MQW structure to obtain the condition for the bound states:

$\dagger$ *the expression for* Φ_{cap} *was chosen such that for large t, it reduces to* $\Phi_{cap} \alpha e^{k_b x}$

$$a_n^w \sin k_w L + b_n^w \cos k_w L + \xi^{-1}(a_n^w \cos k_w L - b_n^w \sin k_w L) = 0 \tag{4-3a}$$

where

$$a_i^w = \xi \, (a_{i-1}^b \cosh k_b d + b_{i-1}^b \sinh k_b d), \qquad 1 < i < n$$
$$b_i^w = a_{i-1}^b \, (\sinh k_b d + b_{i-1}^b \cosh k_b d), \qquad 1 < i < n$$
$$a_i^b = 1/\xi \, (a_i^w \cos k_w L - b_i^w \sin k_w L), \qquad 1 \le i \le n$$
$$b_i^b = a_i^w \sin k_w L + b_i^w \cos k_w L \qquad 1 \le i \le n.$$
$$a_1^w = \xi \cosh k_b t / \sinh k_b t, \; b_1^w = 1 \tag{4-3b}$$

It is easy to verify that for large t, eq. (4-3a) reduces to eq. (1-1) for the SQW in the case n = 1; also for n = 2, eq. (4-3a) reduces to the expression[BZ84,W87] for the Double Quantum Well (DQW) having barriers of infinite spatial extent on each side of the DQW structure. The levels associated with the first electron bound states for well(s) of width L = 8.0 nm and depth V = 121 meV, and barrier(s) of thickness d = 10.0 nm are found from fig. 4-3 which shows the values of the L.H.S. of eq. (4-3a) in the case of a SQW, DQW, and so on, up to a MQW with 6 wells. Fig. 4-3a is valid for cap layers thicknesses larger than about 10.0 nm†, and fig. 4-3b is for a cap layer thickness t = 2.5 nm. Bound states are obtained if the L.H.S equals 0 as prescribed by eq. (4-3a). As expected,

† *Appendix 3 elaborates on an interesting analogy which can be found between fig. 4-3a for the bound states of the MQW with n wells, and the Legendre's polynomial* P_n.

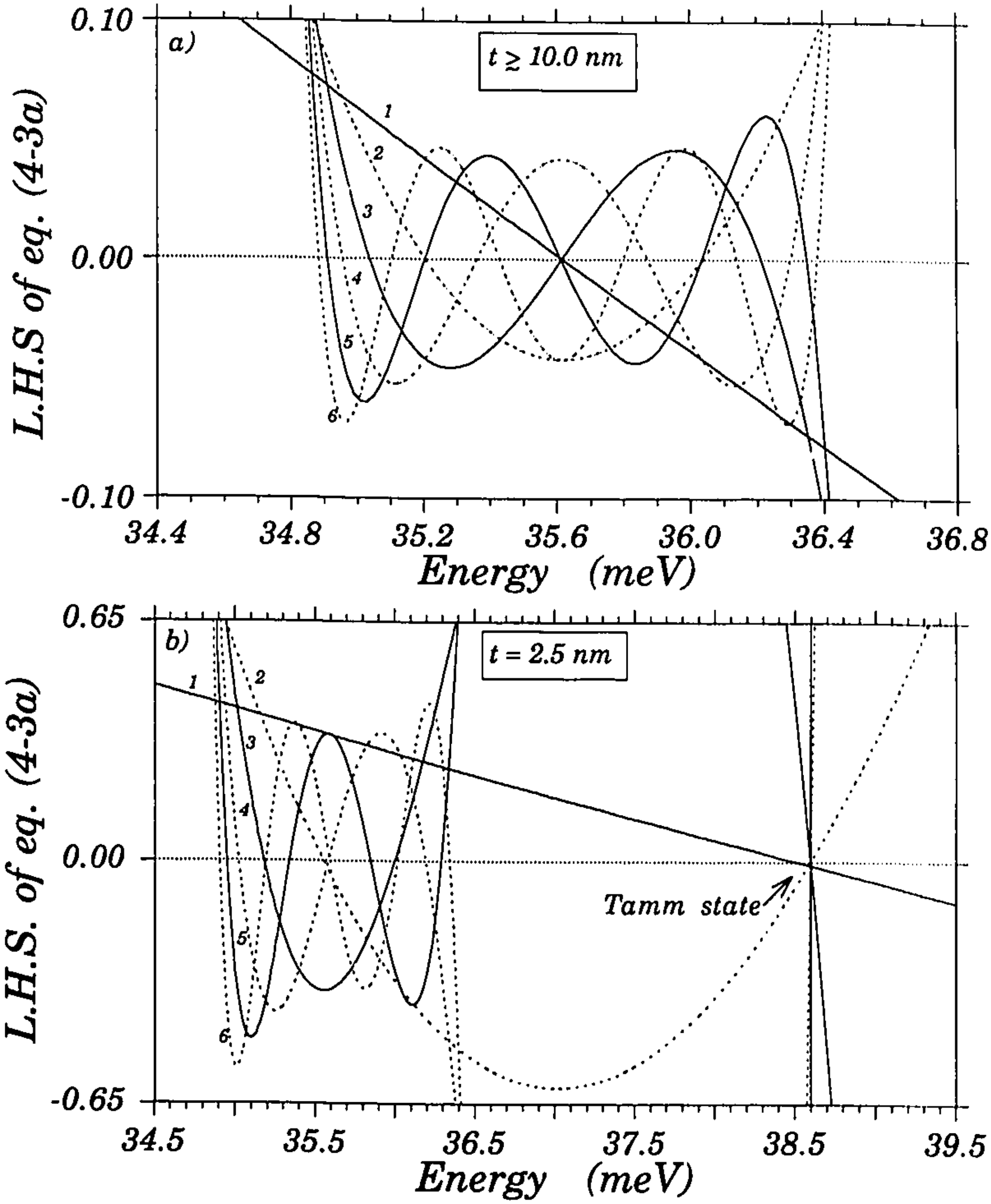

Fig. 4-3: Condition for the first bound electron state(s) for well(s) of width L = 8.0 nm and depth V = 121 meV, and barrier(s) of thickness d = 10.0 nm. 1 is for a SQW, 2 is for a DQW, and so on, 6 is for a MQW with 6 wells. Bound states exist at the energies at which the L.H.S. of eq. (4-3a) is equal to 0. a) is valid for cap layers thicker than about 10 nm, and b) is for t = 2.5 nm. For a thin cap layer, a Tamm state appears at higher energy.

the MQW has the same number of bound states and wells. For example in a) (i.e. for "thick" cap), the energy of the bound state of the SQW is found to be 35.62 meV, and the 5 levels of the MQW with 5 wells are: 34.91, 35.20, 35.62, 36.04, an 36.36 meV† . In the latter case, the energy difference between the highest and lowest levels is 1.45 meV. For the corresponding superlattice, the value found for the bandwidth from fig. 4-1 is 1.68 meV, and so the energy splitting of the levels of MQW with only 5 or 6 wells is comparable with the bandwidth of the corresponding superlattice ($n \rightarrow \infty$). Sect. 4-3 will give experimental results obtained with a MQW having 5 wells as described above. The spacing between the levels of the MQW electron ground state found above is to small to be resolved experimentally[CT89], but lineshape broadening associated with that "bandwidth" could be observed. In any case, fluctuation in the well width, or in the depth of the well due to small variations in the alloy composition, would induce changes in the energy levels[LS90] larger than those obtained for the splitting associated to the overlap of the wavefunctions.

In fig. 4-3b, for a cap layer thickness of 2.5 nm, the SQW level has been shifted toward higher energy by 3.0 meV from 35.6 to 38.6 meV because of the thin cap layer as was explained in sect. 1-3-1. The n-1 lowest levels of the MQWs are not

† *Appendix 3 gives an interesting alternative to evalulate the bound states of MQW.*

perturbed significantly by the thin cap layer, however the highest level of each MQWs is shifted to the same energy has that of the corresponding SQW with a thin cap layer. This single level at higher energy was labeled "Tamm state" in reference to Tamm's work† in 1932 which pointed out that the inclusion of the neglected surface in a Kronig-Penney model results in electronic states localized at the surface of a solid. This is also similar to the "Tamm states" found by Ohno & Mendez[O90] who observed similar levels in "terminated" superlattices: i.e. a superlattice having its last barrier of a different height, similar to the problem studied here if t=0 and the potential at the surface was considered of finite height. In any cases, the last well has a different electronic environment which perturbs its energy levels. In particular, here for the MQW sample with the thin cap layer, the well adjacent to the cap would be in an environment similar to the one described in sect. 1-3-1 for the SQWs. The cap layer thickness dependence of the 5 energy levels of the MQW with 5 wells of fig. 4-3b is shown in fig. 4-3c. As mentioned above the 4 lowest levels are not influenced significantly by the thickness of the cap layer (here, their energy is increased by ~ 0.4 meV between t ~ 10.0 nm and t = 0 nm), but the Tamm state increases its energy by 16 meV from t ~ 10.0 nm and t=0 nm.

† *From reference 1 of O90: I. Tamm, Phys. Z. Sowjetunion 1, 733 (1932).*

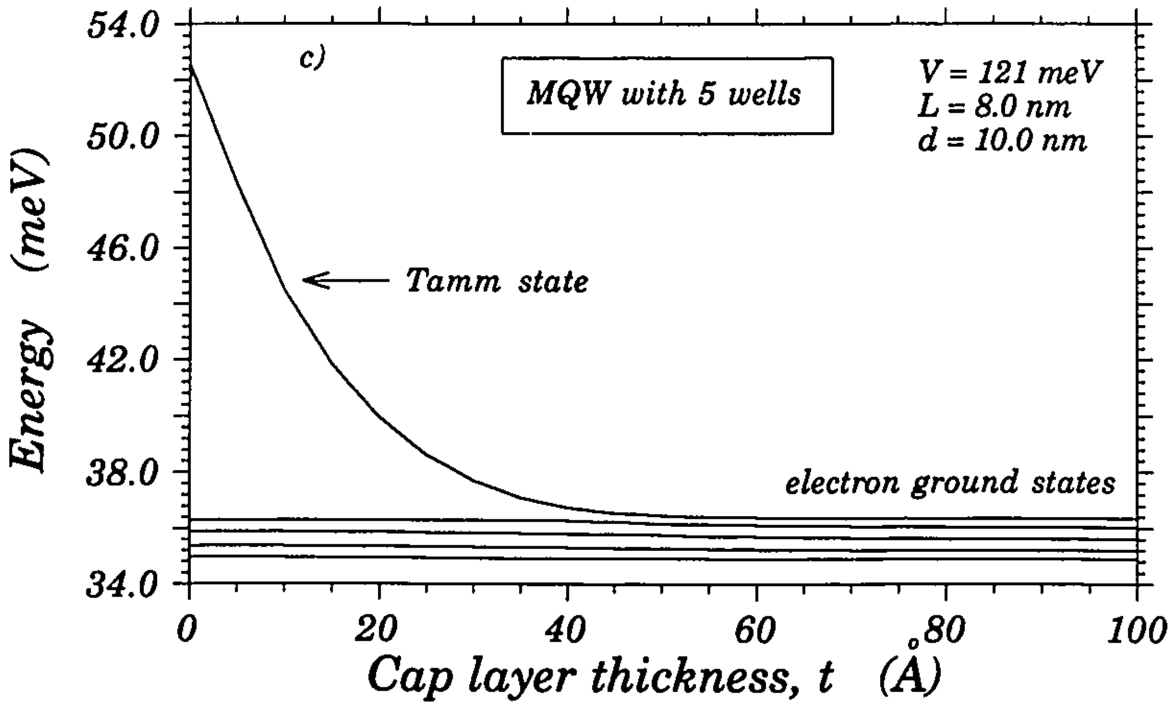

Fig. 4-3c: Dependence on the cap layer thickness of the 5 ground state electron levels of a MQW with 5 wells with L = 8.0 nm, d = 10.0 nm; and V = 121 meV. ($In_{0.16}Ga_{0.84}As/GaAs$ at T = 5 K)

The examples of the present section showed that for the cap layer thicknesses studied experimentally in this work, the energy levels of the bound states will not be affected by the size of the cap layer. As was shown for the SQW, this will not be the case for the continuum states which are discussed in next section.

4-2 Theory for the continuum states:

The band diagram corresponding to the MQW problem studied here was shown in fig. 4-2. The solution for the continuum states (i.e. energy larger than the barrier) is obtained in the same way as was done in sect. 1-3-2, but now the calculations have to be carried through all the interfaces as done in sect. 4-1. Taking $x = 0$ at the surface where the potential is assumed infinitely high, $\Phi_{cap}(x) \propto \sin k_b x$ in the cap layer, and if the wells are separated by barriers of thickness d, the solution in the region of the i^{th} well is given by:

$$\Phi_i^w = a_i^w \sin k_w[x-t-(i-1)\times(L+d)] + b_i^w \cos k_w[x-t-(i-1)\times(L+d)], \tag{4-4a}$$

and for the i^{th} barrier (the barrier following the i^{th} well):

$$\Phi_i^b = a_i^b \sin k_b[x-t-L-(i-1)\times(L+d)] + b_i^b \cos k_b[x-t-L-(i-1)\times(L+d)]. \tag{4-4b}$$

The wavefunction in the buffer region for a MQW having n wells is just $\Phi_{buf} = \Phi_n^b$. The wavefunction and its derivative divided by the relevant effective mass are matched at all the interfaces of the MQW structure to obtain the coefficients of eqs. (4-4a) and (4-4b):

$$a_1^w = \xi \cos k_b t,\ b_1^w = \sin k_b t, \tag{4-4c}$$

$$a_i^w = \xi\ (a_{i-1}^b \cos k_b d - b_{i-1}^b \sin k_b d), \qquad i > 1$$

$$b_i^w = a_{i-1}^b(\sin k_b d + b_{i-1}^b \cos k_b d), \qquad i > 1$$

$$a_i^b = 1/\xi\ (a_i^w \cos k_w L - b_i^w \sin k_w L), \qquad 1 \le i \le n$$

$$b_i^b = a_i^w \sin k_w L + b_i^w \cos k_w L \qquad 1 \le i \le n.$$

Integration of the probability density ($|\Phi(x)|^2$) in the various regions gives the unnormalized probabilities:

$$p_{cap} = t/2\left[1 - \frac{\sin 2k_b t}{2k_b t}\right], \tag{4-5}$$

for the i^{th} well:

$$p_i^w = L/2\left[(a_i^{w\,2} + b_i^{w\,2}) + (b_i^{w\,2} - a_i^{w\,2})\ \frac{\sin 2k_w L}{2k_w L} + 2a_i^w\ b_i^w\ \frac{\sin^2 k_w L}{k_w L}\right]$$

and for the i^{th} barrier: $i < n$ (n well):

$$p_i^b = d/2\left[(a_i^{b\,2} + b_i^{b\,2}) + (b_i^{b\,2} - a_i^{b\,2})\ \frac{\sin 2k_b d}{2k_b d} + 2a_i^b\ b_i^b\ \frac{\sin^2 k_b d}{k_b d}\right]$$

and finally for the buffer:

$$p_b = \frac{x_{max}}{2}\left[(a_n^{b\,2} + b_n^{b\,2}) + (b_n^{b\,2} - a_n^{b\,2})\frac{\sin 2k_b x_{max}}{2k_b x_{max}} + 2a_n^b\ b_n^b\ \frac{\sin^2 k_b x_{max}}{k_b x_{max}}\right]$$

The normalized probabilities of finding the carriers in the various regions of the MQW are then calculated from eqs.(4-5) in a manner similar to that used in eqs. (1-11) for the SQW case.

The cap-related oscillations of the probabilities of finding the carriers in the various regions will be affected by the presence of additional wells of the MQW. As a first step towards the illustration of the changes induced by the additional wells, the case of a Double Quantum Well (DQW) will be investigated theoretically here. For example, consider two wells with the characteristics of the single well of sect. 1-3-2, fig. 1-5, (well width 3.5 nm, cap layer is 50.0 nm, V^n = 121 meV, $m_w^* = m_b^* = 0.0665\ m_o$, buffer 1.0 μm) separated by d = 5.0 nm. The normalized probabilities of finding the carriers in the various regions (P_{cap}, P_1^W, P_1^b, P_2^W, P_b) of such a MQW structure are obtained from eqs. (4-4) and (4-5). Fig. 4-4a,b,c show the probabilities of finding the electrons in the cap layer (P_{cap}), over the first well (P_1^W), and over the second well (P_W^2) respectively. Comparing with fig. 1-5 for the SQW, one sees that the probabilities peak at around the same energies, but the peaks are sharper and higher, giving even better contrasts. A remarkable feature in the first well of the DQW (the well adjacent to the cap), in fig. 4-4b, is that at the peaks, the probabilities are higher than the classical probability in contrast to the situation of the SQW where they

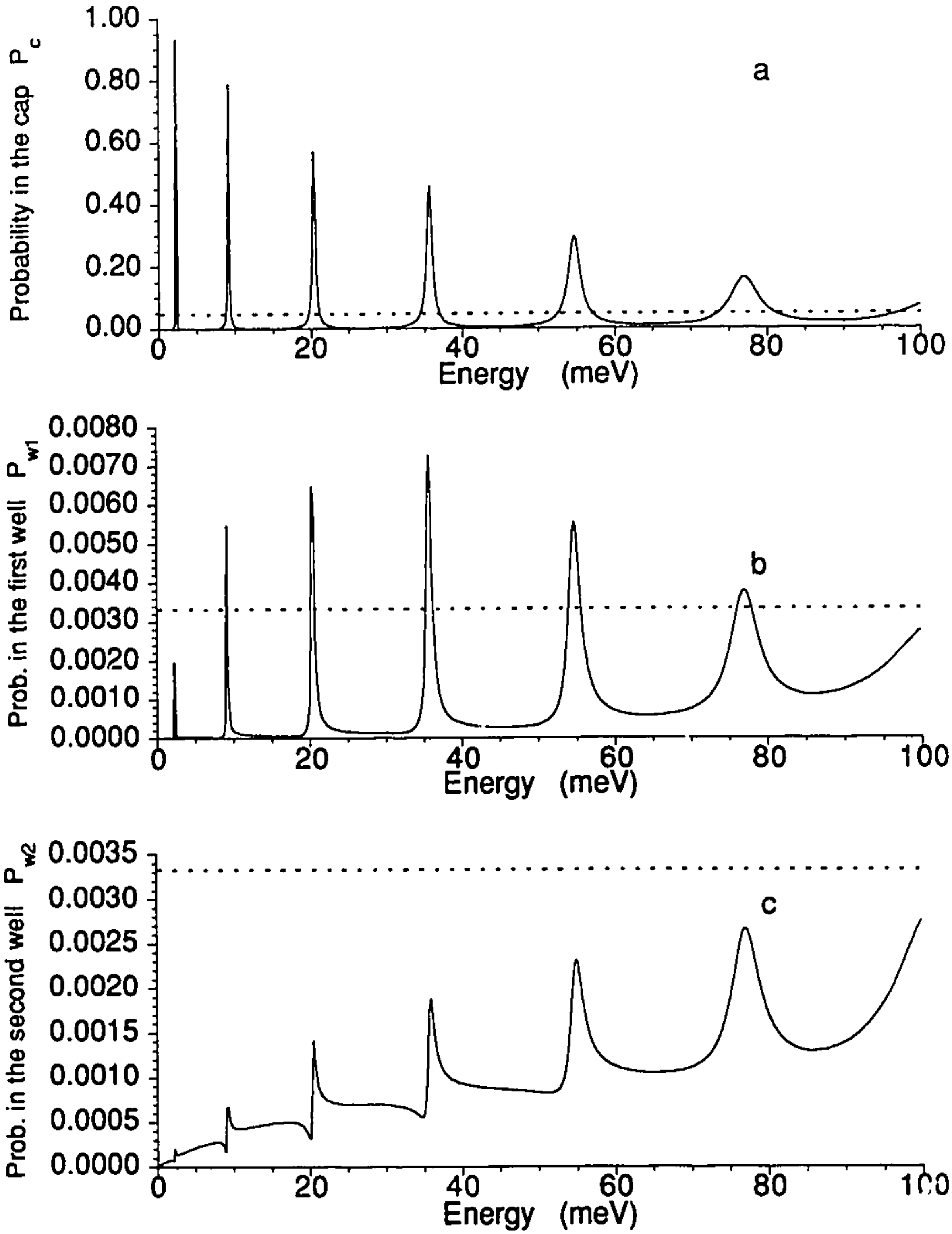

Fig. 4-4: Energy variations of the normalized probabilities of finding the electrons in the various regions of a Double Well separated by a barrier of width d = 5.0 nm, for the structure of fig. 1-5. a) is for the cap layer region and b) is for the first well, c) is for the second well. Compare with fig. 1-5 for a single well.

were lower (fig. 1-5b). However, in the second well (the well adjacent to the buffer) in fig. 4-4c, the values of the probabilities at the peaks are smaller than the classical probability, as in fig. 1-5b for the SQW. These results show that the first well, closer to the surface, will be more energy selective in capturing carriers in the continuum. This may result in different capture efficiencies for the various wells of a MQW structure.

Trial calculations with values other than $d = 5.0$ nm indicate that the sharpest contrasts in the probabilities (sharps peaks with high maxima and low minima) are obtained with small values of $k_b d$ (i.e. $k_b d$ smaller than π for $E \lesssim$ a hundred meV). Whenever $k_b d$ is equal to a multiple of π, extra features are observed with the probabilities. However, a detailed analysis of all the parameters involved in MQW in the vicinity of a high potential (or other structures such as the double barrier potential) is beyond the scope of this work. Calculations with more than two wells have indicated that the trend described above (sharper peaks with higher maxima and lower minima) continues as the number of wells is increased. And so it may be possible to observe better the influence of the finite size of the cap layer on the continuum states of MQW having the same parameters as those SQWs which showed only weak cap-related oscillatory behavior (samples 4 and 5). To that effect, the next section will present experimental results obtained with a MQW with 5 wells equivalent to the SQW of sample 5.

4.3 Experimental results:

The experimental results discussed in the present section were obtained on a MQW sample having 5 wells of nominal width L = 8.0 nm, with barriers of thickness d = 10.0 nm, a cap layer of 65 nm, and a buffer of 1.0 μm. Fig 4-5 shows a PV spectrum obtained with this MQW at T = 77 K. The labels of fig. 4-5 corresponds to those of fig. 3-22 showing ER spectra obtained with the corresponding SQW with the same well width and alloy composition; the PV spectrum displays typical staircase features associated with the 2-D density of state of the carriers confined in the well. This is in contrast with the derivative nature of the features of fig. 3-22, typical of the ER. The PV spectrum of fig. 4-5 was chosen to illustrate the effect of inter-well fluctuations of the parameters from the growth conditions. The peak labelled 11H′ originates from the 11H transition from one (or more) of the 5 wells which have a slightly smaller well width, or smaller alloy concentration (since the peak is at higher energies). The energy difference between 11H and 11H′ is about 12 meV. This value is much too large to be accounted by the bandwidth due to the overlap of the MQW wavefunctions (calculated to be ~ 2 meV in fig. 4-1 or 4-3). From calculation, this would correspond to a

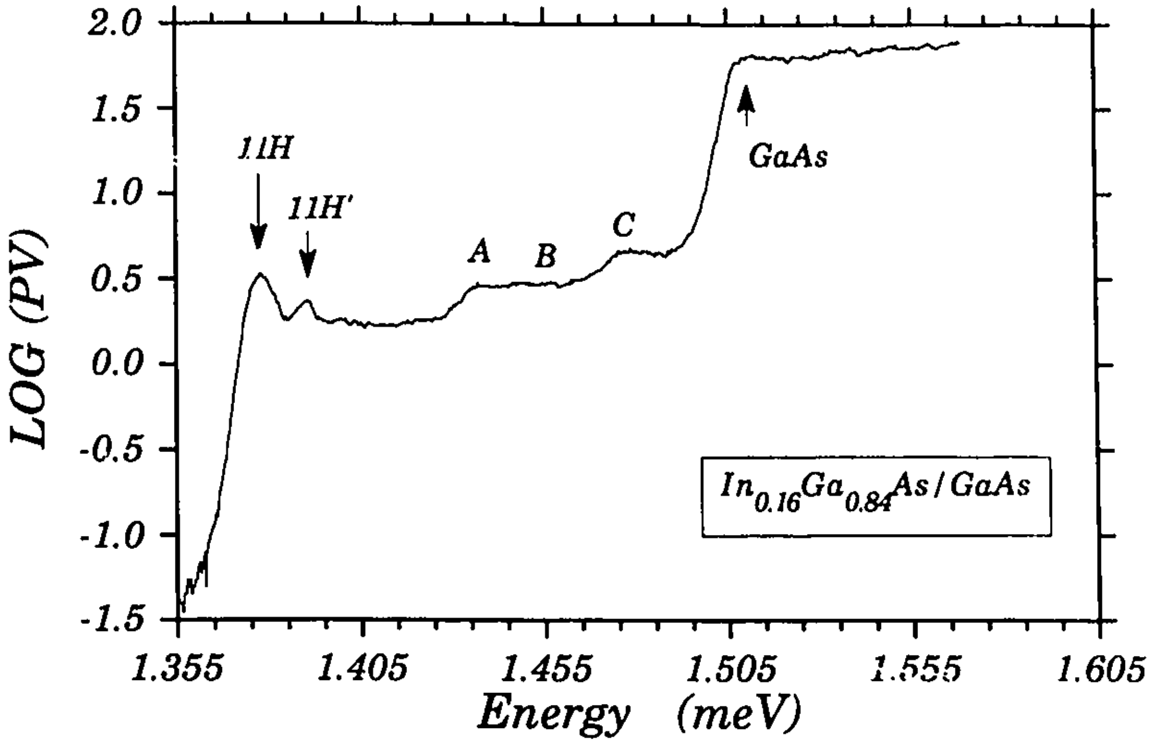

Fig. 4-5: Log (PV) spectrum of a MQW sample, at T = 77 K, with 5 wells of 8.0 nm, 4 barriers of 10.0 nm, and a cap of 65 nm (nominal values).

well about 1.0 nm narrower, or a indium composition smaller by about 1%. This interpretation is further confirmed by PL (spectra not shown), which shows a satellite peak also at an energy about 12 meV higher than the main 11H peak. The relative amplitude between the 11H and 11H' peak in the PL spectrum suggest that only one of the wells has different parameters. The other wells of the MQW are giving a 11H peak at the same energy of that of sample 5 of chapter 3, confirming that the only difference (apart for the well which gives rise to the 11H' peak) between this MQW and the SQW sample 5 of chapter 3, is that the MQW has 5 wells instead of one (with the same cap layer thickness t). Hence the ER results obtained with this MQW should be compared with those of the SQW sample 5 in fig. 3-22 to understand the influence of additional wells on the above-barrier cap-related oscillations.

The ER spectra obtained with the MQW sample, at T = 77 K, are shown in fig. 4-6 for bias voltages between -1.4 and 1.4 V by increments of 0.2 V. For bellow gap energies, the spectra are comparable to those of fig. 3-22, except for the 11H' peak explained above. The energy difference between the 11H and 11H' found by electrorelectance is also about 12 meV. The feature labelled B, associated with the continuum states (as explained in sect. 3-2-2), is shifting as in fig. 3-22 for the SQW. For above-gap energies, the cap-related oscillation are much more pronounced than those seen in the spectra of the SQW in fig. 3-22. This was expected because the presence of additional wells in the case of MQW was found to enhance the contrasts oscillations of the probabilities of finding the carriers in the various regions of the MQW structure (see sect. 4-2). The above barrier oscillations of fig. 4-6 resemble closely to the oscillations observed in the ER spectra of sample 2 (in fig. 3-18) which has the same cap layer thickness, but a narrower well width. At positive biases, the spectra display the cap-related oscillations for the corresponding cap thickness for the electrons. As the negative bias increases the electric field, the extrema of the

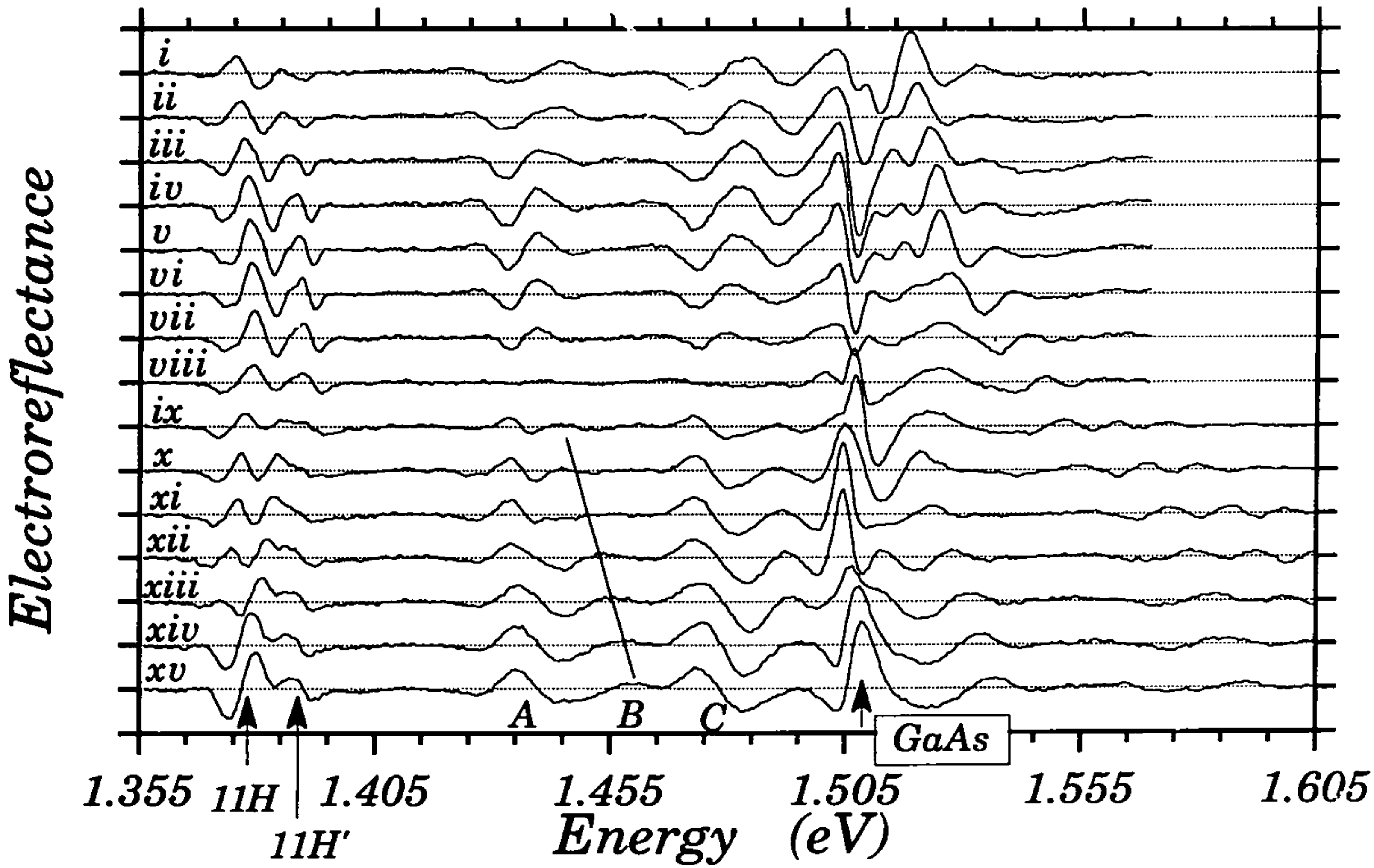

Fig. 4-6: ER spectra of a MQW sample, at T = 77 K, with 5 wells of 8.0 nm, 4 barriers of 10.0 nm, and a cap of 65 nm. The bias voltage is changed from 1.4 V (curve i) to -1.4 V (curve xv) by increment of 0.2 V. ($In_{0.16}Ga_{0.84}As/GaAs$).

oscillations are shifted towards higher energies.

The literature contains several examples[JD89,P88,TB90] of results which show above-barrier spectral structures observed in modulation spectroscopy of MQW samples. If thin cap layers were used, it is possible that some of these results may incorporate cap layer effects as discussed here. This may help to interpret the results of Tobler[TB90] which describes quadratic above-gap oscillations.

Sect. 4-3 has shown experimentally that the above-barrier oscillations related to the finite-size of the cap layer as discussed in chapter 1 were enhanced by the presence of additional wells as predicted in sect. 4-2. Further work remains to be done with MQWs because the cap layer thickness of the sample used in this work was to large to possibly observe any shifts in the bound states associated with the size of the cap layer as predicted in sect 4-1; and the barrier thickness and well width used here did not permit to resolve the splitting of the bound levels (as shown in sect 4-1) in the MQW sample (i.e. the overlap of the wavefunctions was to small for the present values of L and d).

CONCLUSIONS

The model of a SQW in the vicinity of a high potential was developed in chapter 1 to take into account the finite-size of the cap layers of SQW devices. The theory was presented for the bound states and for the continuum states of such structures. The theory predicts shifts in the energy of the bound states for cap layer thicknesses smaller than about 10.0 nm, and energy-dependent oscillations of the probabilities of finding the carriers in the various regions for the continuum states of the SQW structure with cap thicknesses as large as 100 nm. The theory also predicts that an applied uniform electric field can shift the extrema of the cap-related continuum states oscillations, and increase the well occupancy at small energies above the barrier. $In_xGa_{1-x}As/GaAs$ semiconductor heterostructures with cap layers between 50 nm and 100 nm were used to verify experimentally the theoretical model of chapter 1, after the samples were well characterized with a sequential study.

As expected from the theoretical considerations, transitions involving bound states only, did not show any cap layer related effect for the cap thickness studied (the smallest cap thickness was t=50 nm), but the ER spectra could be used to verify that the transitions follow the expected selection rules, and are Stark shifted with the electric field. Systems with thinner cap layers were studied by Moison et al[ME90] in order to reveal the effect of the cap layer on the bound energy levels in AlGaAs/GaAs quantum wells. The blue shift in the transitions involving bound states expected for thin cap layer was not observed, supposedly because of surface states. In the present study, the influence of the cap size on the continuum states was clearly demonstrated: cap-related energy-dependent oscillations were observed in PR (for the flat band condition) and ER (for the applied electric field) spectra at above-barrier energies. The spacing between the extrema of the oscillations increases as the energy above the barrier is increases, as expected (for the flat band condition) for extrema of oscillations determined mainly by $\sin^2(k_b t)$. For a 50 nm thick cap layer the carriers mainly responsible for oscillations were the heavy holes, and for thicker cap layer the carriers giving the major contribution to the oscillations changes to the electrons which have a smaller effective mass. The extrema of the oscillations were found to shift linearly with the applied electric field, but these shifts were not always in perfect quantitative agreement with the model (especially for thicker cap), probably because of band bending near the surface. For the thicker cap layer, the sample seems to recover the character expected for barrier of infinite extent on each side, the usual resonant states giving contribution to the spectra. It would be interesting to study experimentally samples with cap layer thicker than 100 nm in order to follow the above trend.

Chapter 4 has extended the model of the SQW of chapter 1 to deal with MQW. For the bound states, the theory considered the finite number of wells, and the finite-size of the cap layer. This showed that for cap thicknesses smaller than about 10 nm, the energy of the well closest to the surface would be modified similar what was predicted for the SQW, and similar to the Tamm states predicted and observed with superlattices terminated with a barrier having a different height. For the continuum states, it is predicted and observed in this work that that the contrast in the cap-related oscillations is enhanced by the presence of additional wells in the case of MQW. For example, cap-related above barrier oscillations were clearly observed in the ER spectra of the MQW, whereas these oscillations in the corresponding SQW were weak.

In summary, one cannot assume the barrier to be infinite in extent in many actual quantum well systems, and the cap layer thickness (and its nature: barrier-terminated sample like the InGaAs/GaAs system, or well terminated sample like it is often the case with the AlGaAs/GaAs system) must be considered in the design of the samples since it may significantly influence the properties of the system. Future work could try to verify the effect of a (very) thin cap layer on the bound states of

SQW and MQW as predicted in chapter 1 and 4, and also try to verify the energy splitting due to the overlap of the wavefunctions in MQW having a small number of wells. One could also study the present model in the presence of other external perturbations such as an applied magnetic field, or apply the present model to heterostructure systems based on different semiconductor materials, or to structures with a different potential configuration.

APPENDIX 1

COLLECTING PL WITH 2 LENSES

A particular emphasis will be given on the optimization of the experimental conditions, in order to get a maximum of sensitivity from the apparatus, and so to avoid unnecessary sample perturbations while probing their energy levels. A lack of attention on the specific characteristics of the equipment required, or the exact position of the optics could severely deteriorate the quality of the experimental results. In the present appendix, a short description will be given on how one can maximize the efficiency of a set-up using two lenses to collect the PL.

The experimental set-up for PL was shown schematically in fig. 2-4. The sample is placed in an optical cryostat, and is excited with a filtered laser beam. The emitted PL is collected and passed through a spectrometer, the dispersed PL is then detected with the PM. Two biconvex lenses (L1 and L2) are positioned to optimized the signal reaching the PM as sketched in fig. 2-4. The sample, at a distance d from the optical window inside the cryostat, is assumed to be a point source of PL (i.e. isotropic emission of PL originating from the point of excitation), the cross-section of the cone of light coming out of the optical window with a plane at a distance $d+\delta$ from the sample will be a circle of radius $r_l = r_w \frac{(d+\delta)}{d}$, where r_w is the radius of the window. If the focal length of L1 is chosen equal to the distance d+δ, the rays coming out of L1 are parallel, the image being projected at ∞. And so, the second lens L2 placed at a distance d_{12} will produce an image of the PL emitting sample at its focus, magnified by a factor $M=f_2/f_1$ (i.e. the ratio of the focal lengtns of the lenses). The rays going through the slits will proceed in the spectrometer as shown in the fig. 2-4, and reach the back mirror of the spectrometer. From simple geometrical consideration, the image formed in the spectrometer at a distance f_s will then have a lateral half-width $r_m = r_l \frac{f_r}{f_2}$. In practice d and r_w are fixed (for example for the liquid nitrogen cryostat used in the experiments, d=5.0 cm, r_w= 1.0 cm), so in order to maximize the throughput, δ and hence f_1= d+δ are chosen so that r_l is equal or smaller than the radius of the lenses used (typically, r_l = 25 mm), therefore $f_1 \leq$ 12.5 cm. The magnification M has to be minimum to avoid light hitting outside the narrow entrance slit, so that f_1 is chosen as large as possible: i.e. f_1=12.5 cm. The distance d_{12} will not influence very much the throughput because the rays are parallel between the two lenses, so it can be a useful adjustable distance in the optical setup. f_s is also fixed; it is the focal length of the spectrometer used: here, f_s= 1.0 m. Similarly, r_m is chosen equal to the half-width of the mirror in the back of the spectrometer: r_m= 6.5 cm. This fixes the value for $f_2 = f_s \frac{r_l}{r_m}$ $\approx$ 38 cm. These values will optimize the efficiency at collecting the emitted light and directing it to the PM through the spectrometer. Other system, such as mirrors (see appendix 2 which describes how to optimize a set-up using a single mirror with a white source for a monochromator), can be used to collect the PL; they can be optimized using similar considerations.

Sec. 2-2 also explained that the choice of the angle at which the PL is collected will have a significant influence on the efficiency of the detection. Collecting the PL perpendicularly to one of the surfaces of the sample (i.e. from the edge or from the face) will optimize the amount of PL reaching the detection system. Collecting the PL from the edge is easier experimentally, and will have the additional advantage that if the material is transmitting well at the wavelength of emission, the sample may form a waveguide for the PL into the collecting system.

APPENDIX 2

OPTIMIZATION OF THE EFFICIENCY OF A MONOCHROMATOR USING A SINGLE MIRROR TO COLLECT THE LIGHT

The required monochromatic beam of light for PR, ER, or PV was obtained using a set-up as in fig. 2-7. The light emitted by a 30 Watts quartz iodine light source is dispersed spectrometer such as the one described for the PL in appendix 1. The visible and infrared (IR) photons emitted by the vertical tungsten filament of width w_f=1 mm are collected and directed to the adjustable entrance slit (of width w_s) of the spectrometer. Appendix 1 described how to maximize the amount of light collected with two lenses for PL experiments. However, achromatic lenses could be required for experiments such as PR, ER, or PV because the broader range of wavelength covered. So it is often more convenient to collect the light with a single concave mirror which will not suffer from chromatic aberration. So here a description will be given on how to optimize the amount of light collected with a single-mirror system as shown in the fig. 2-7. Say the photon flux exiting through the aperture of the box containing the filament is ϕ_o, and the cross-section of the light cone at a distance o from the source has a diameter h = αo (where α is source dependent via the size of the aperture, and the aperture-filament distance). The mirror (which is assumed to reflected 100% of the light) of radius r_m and focal length f is placed at o, and produces an image of the filament on the entrance slit (which has a width w_s) at a distance $i=fo/(o-f)$, and magnified by a factor $g=f/(o-f)$. The rays going through the slit will form a cone which has a half-width $y=f_s r_m/i$ at a distance f_s from the slit. If ϕ_{eff} is the photon flux reaching the back mirror (which has a half-width r_{mb}) of the spectrometer at a distance f_s from the slit, the overall efficiency of the collecting system is $\varepsilon = \phi_{eff}/\phi_o = \varepsilon_m \varepsilon_s \varepsilon_{mb}$. It is the product of the fraction of the light collected by the mirror (ε_m), times the fraction which passed through the slit (ε_s), times the fraction which reach the mirror in the back of the spectrometer (ε_{mb}). It is easy to show that $\varepsilon_m = \pi r_m^2 /h^2$, $\varepsilon_s = w_s/gw_f$, $\varepsilon_{mb} = \pi r_{mb}^2 / \pi y^2$. And so after simplifications:

$$\varepsilon = \frac{\pi r_{mb}^2 w_s}{\alpha^2 f_s^2 w_f} \frac{f}{(o-f)}. \qquad (2\text{-}3)$$

Eq. (2-3) is valid for $w_s \leq gw_f$, and it can be shown that the optimum efficiency ($\varepsilon^{\bullet}$) is obtained if

$$f_s r_m / f r_{mb} \equiv \frac{f/\#_s}{f/\#_m} \geq 2 \qquad (2\text{-}4)$$

where $f/\#_s$ and $f/\#_m$ are the spectrometer and mirror f-number respectively, and if the back mirror of the spectrometer is just completely covered (i.e. $y=r_{mb}$). Then the optimum values for i and o are:

$$i^{\bullet} = f_s r_m / r_{mb},$$
$$o^{\bullet} = (f_s r_m / r_{mb}) / (f_s r_m / f r_{mb} - 1), \text{ and} \tag{2.5}$$
$$\varepsilon^{\bullet} = \frac{\pi r_{mb}^2 w_s}{\alpha^2 f_s^2 w_f} (f_s r_m / f r_{mb} - 1).$$

Eq. (2.5) indicates that the optimum efficiency for a chosen spectrometer improves proportionally to the radius of the mirror collecting the light, and is inversely proportional to its focal length, i.e. it improves inversely proportional to the f-number of the mirror ($f/\#_m$). Spherical aberrations imposes the limit on how small $f/\#_m$ can be chosen. For the system used, f_s=100 cm, r_{mb}= 8 cm, α=0.7, r_m=6.5 cm, f=29.3 cm, and so eqs. (2-5) are valid and give $i^{\bullet}$=81 cm, and $o^{\bullet}$=46cm, and $\varepsilon^{\bullet}$=7% (w_s/w_f), where the efficiency is directly proportional to the slitwidth (which is adjusted according to the resolution requirements).

If the f/# of the mirror is not smaller than a factor of two with respect to the f/# of the spectrometer, then the optimum efficiency is not as good. Indeed, if eq. (2-4) is not satisfied, i.e. for the case $\frac{f/\#_s}{f/\#_m} < 2$, the optimum efficiency is obtained if $i^{\bullet} = o^{\bullet} = 2f$; and then

$$\varepsilon^{\bullet} = \frac{\pi\, w_s}{4\alpha^2 w_f} \frac{r_m^2}{f^2} = \frac{\pi\, w_s}{4\alpha^2 w_f} \left(\frac{1}{f/\#_m}\right)^2.$$

Therefore if the f-numbers are almost matched, the optimum efficiency is inversely proportional to the mirror f-number, also the resolution may be affected because then the mirror at the back of the spectrometer (and hence the grating) will not be entirely covered (to cover entirely the mirror at the back of the spectrometer using a single mirror with the same f/#, one would have to place the source at infinity !).

In conclusion, to get a good efficiency in collecting the light with a single-mirror set-up, a mirror with a f-number smaller than half of that of the spectrometer must be used with the values obtained from eqs. (2-5).

The monochromatic beam which exits the spectrometer, is reflected, with another concave mirror, on the sample through one of the optical windows of the crystal. The efficiency of this process is 100 % as long as the distance between the mirror and the exit slit is not too large so that the light exiting the spectrometer could be entirely contained on the mirror. Within this restriction, the mirror will generally be placed as far as possible from the slit in order to increase the intensity of the light hitting the sample (i.e. decrease the magnification so that the area of the image of the slit on the sample is decreased).

APPENDIX 3

ANALOGY BETWEEN THE CONDITION FOR BOUND STATES OF MQW AND THE LEGENDRE'S POLYNOMIALS

Readers familiar with the Legendre's polynomials must have noticed the striking resemblance between fig. 4-3a which shows the conditions for the bound states of the MQWs, and the graph of Legendre's polynomial. For comparison purposes, fig. A-1 reproduces the Legendre's polynomials from $P_1(-x)$ to $P_6(-x)$, for x between -1 and 1. These polynomials can be found using Rodrigues' formula:

$$P_n(x) = \frac{1}{2^n n!} \frac{d^n}{dx^n} [(x^2-1)^n],$$

or using the relation between consecutive polynomials:

$$P_{n+1}(x) = \frac{1}{n+1} [(2n+1)\ x\ P_n(x) - n\ P_{n-1}(x)],$$

where

$P_1 = x,$

$P_2 = 1/2\ (3x^2 - 1),$

$P_3 = 1/2\ (5x^3 - 3x),$

$P_4 = 1/8\ (35x^4 - 30x^2 + 3),$

$P_5 = 1/8\ (63x^5 - 70x^3 + 15x), \ldots$

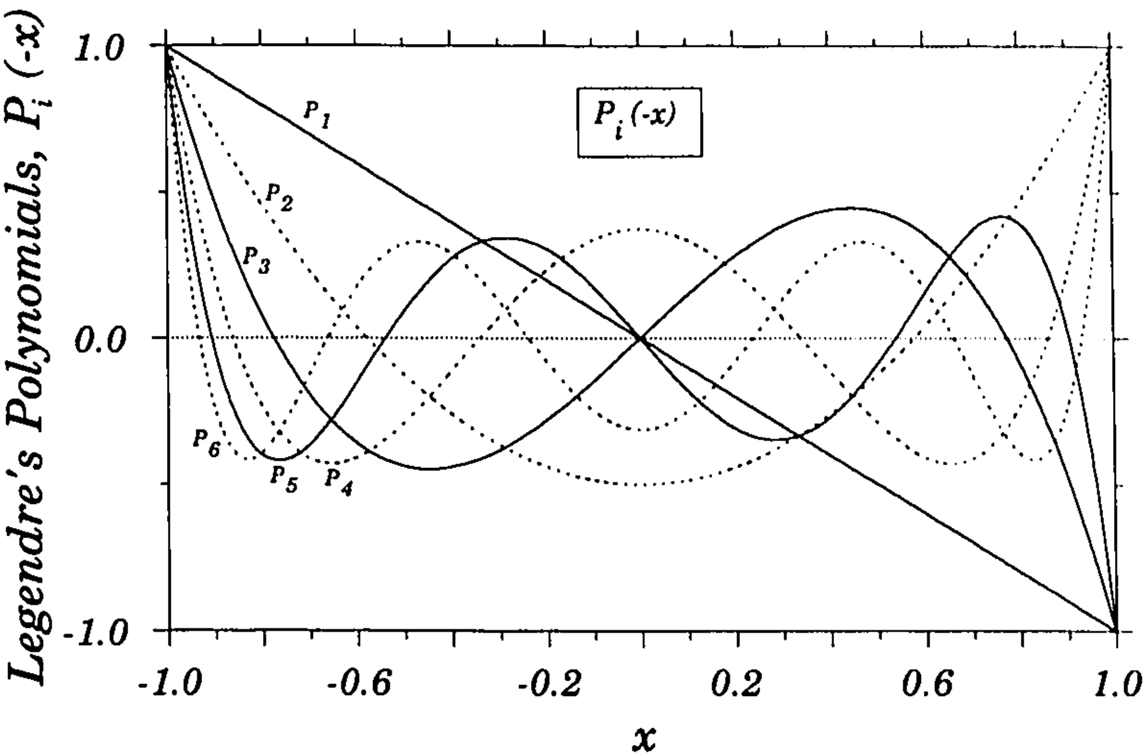

Fig. A-1: Legendre's polynomials. Compare with fig. 4-3a for the MQW bound states.

The resemblance is most likely link to the possibility to expand the condition for bound states in the asymptotic form of the sines and cosines of eq. (4-3a) near the energy at which a bound state occurs. There is no a priori reason why eq. (4-3a) would satisfy Legendre's differential equation

$$(1-x^2)Y'' - 2xY' + n(n+1)\ Y = 0$$

for energies close to a bound states, but in any case the resemblance can be very useful to evaluate the energy positions of the MQW bound states. Indeed, the bound states are found if the R.H.S of eq. (4-3a) equal 0. And so, one can

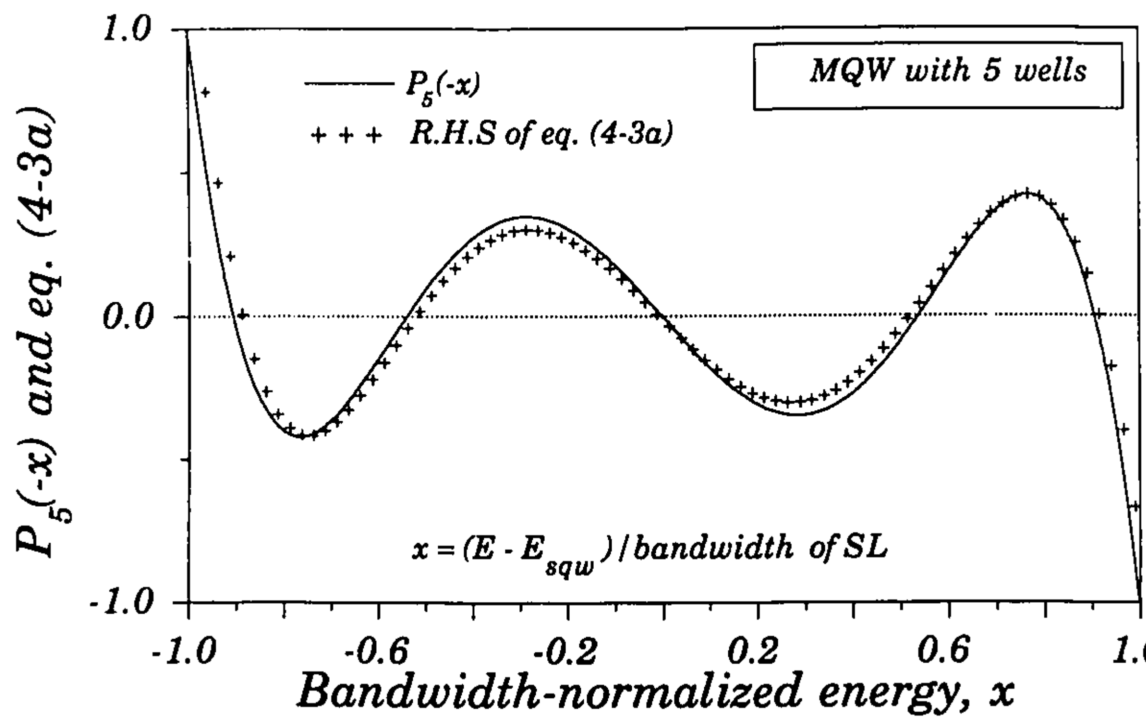

Fig. A-2: Evalution of the bound states of a MQW using the Legendre's polynomials, knowing the energy of the bound state of the corresponding SQW, and the bandwidth of the corresponding SL.

approximate the R.H.S of eq. (4-3a) with the Legendre's polynomials and then use the known values of the zeros of Legendre's polynomial (of order equal to the number of wells in the MQW) to evaluate the energies of the bound states. The zeros of the first few polynomials are as follow†:

n=2: $\pm\ 3^{-1\backslash 2}$
n=3: 0, $\pm\ (3/5)^{1/2}$
n=4: $\pm\ [(15 - 120^{1/2})/35]^{1/2}$, $\pm\ [(15 + 120^{1/2})/35]^{1/2}$

† see p. 916 of *AS65*.

Fig. A-2 gives an example for a MQW with 5 wells and $P_5(-x)$, where the energy in eq. (4-3a) was normalized to the bandwidth of the corresponding superlattice after subtracting the energy of the bound state of the corresponding SQW. As it can be seen on the figure, $P_5(-x)$ reproduces the zeros quite well. And so in summary, instead of solving the MQW levels with eq. (4-3a), one can approximate their energies by first finding the energy of the bound state of the corresponding SQW and the bandwidth of the corresponding superlattice, and then associate the energy range of this bandwidth to the range of -1 to 1 of the Legendre's polynomial of the same order, and make the correspondence with the zeros of that polynomial.

REFERENCES

A80 See for example, D.E. Aspnes, in HANDBOOK ON SEMICONDUCTORS, edited by T.S.Moss (North-Holland, Amsterdam, 1980), vol.2, p.109.

AS64 HANDBOOK OF MATHEMATICAL FUNCTIONS, edited by M. Abramowitz and I.A Stegun (National Bureau of Standards, Washington, D.C., 1964).

B84 G. Bastard, Phys. Rev. **B-30**, 3547 (1984).

B88 G. Bastard. WAVE MECHANICS APPLIED TO SEMICONDUCTOR HETEROSTRUCTURES. Les édition de physique, Paris 1988.

BB86 J.A. Brum and G. Bastard, Phys. Rev. **B-33**, 1420, (1986).

BB91 G. Bastard, J.A. Brum, and R. Ferreira *In* SOLID STATES PHYSICS, **vol. 44**. Edited by H. Ehrenreich and D. Turnbull, Academic Press Inc., San-Diego, 1991. P.229 ff.

BH90 D.C. Bertolet, J.K. Hsu, F.Agahi and K.M. Lau, J. Elec. Mater. **9**, 967, (1990).

BH92 R.A. Batchelor and A. Hamnett, J. Appl. Phy. **71**, 2414, (1992).

BM83 G. Bastard, E.E. Mendez, L.L. Chang, and L. Esaki, Phys. Rev. **B-28**, 3241, (1983).

BP74 G.L. Bir and G.E. Pikus. SYMMETRY AND STRAIN INDUCED EFFECTS IN SEMICONDUCTORS, John Wiley and Sons, N.-Y. (1974).

BZ84 G. Bastard, U.O. Ziemelis, C. Delalande, M. Voos, A.C. Gossard and W. Wiegmann, Solid State Commun., **49**, 671, (1984).

C88 A.Chommette et al, Semic.Sci.Technol. **3**, p.351, (1988).

CC91 C. Coriasso, D. Campi, C. Cacciatore, C. Alibert, S. Gaillard, B. Lambert, and A. Regreny, Europhysics Lett. **16**, 591, (1991).

CT89 S. Charbonneau, M.L.W. Thewalt, E.S. Koteles and B. Elman, Can. J. Phys. **67**, 315, (1989). & Phys. Rev. **B-38**, 6287, (1988).

CV90 F. Cerdeira, C. Vázquez-López, E. Ribeiro, P.A.

Rodrigues, V. Lemos, M.A. Sacilotti, and A.P. Roth, Phys. Rev **B-42**, 9480, (1990).

D90 G. Duggan. *In* Proceedings of SPIE's third symposium on advances in semiconductors, San Diego, March 17-21 1990, session 1283-25.

F92 S. Fafard, Phys. Rev. **B-__**, August 15, 1992.

FB86 J.E. Fouquet and R.D. Burnham, IEEE J. Quan. Elec. **QE-22**, 1799, (1986).

FF91 S. Fafard, E. Fortin and A.P. Roth, Can. J. Phys., **69**, 346, (1991).

FF92a S. Fafard, E. Fortin, and A.P. Roth, Phy. Rev. **B-45**, 13 769, 1992.

FF92b S. Fafard, E. Fortin, and A.P. Roth, Phys. Rev. B, to be published.

FH89a E. Fortin, B.Y. Hua, A.P. Roth, A. Charlebois, S. Fafard, and C. Lacelle. J. Appl. Phys., **66**, 4854 (1989).

FH89b E. Fortin, B.Y. Hua, and A.P. Roth. Phys. Rev. **B-39**, 10 887 (1989).

FR91 E.R. Fortin, A.P. Roth, J. Chim. Phys. **88**, 2197, (1991).

FS85 J.E. Fouquet and A.E. Siegman, Appl. Phys. Lett., **46**, 280, (1985).

G90 O. Glembocki, MRS symposium **160**, 631, (1990).

GS86 O.J. Glembocki, B.V. Shanabrook and W.T. Beard, Surface Science **174**, 206, (1986).

GS89 D.J. Glembocki and B.V. Shanabrook, Superlattices and Microstructures **5**, 603, (1989); & **3**, 235 (1987).

H91 R.J.W. Hodgson, J. Appl. Phys. **70**, 4023, (1991).

HB91 M. A. Herman, D. Bimberg, and J. Christen, J. Appl. Phys., **70**, p. R1, (1991).

HF88 B.Y. Hua, E. Fortin, A.P. Roth, R.A. Masut, Appl. Phys. Lett **53**, 1062, (1988).

HM85 Howes and Morgan, GALLIUM ARSENIDE, (1985).

HM92 F.Y. Huang and H. Morkoç, Appl. Phys. Lett. **60**, 710, (1992).

HQ91 Y.S. Huang, H. Qiang, F.H. Pollak, G.D. Pettit, P.D. Kirchner, J.M. Woodall, H. Stragier, and L.B. Sorensen, J. Appl. Phys. **70**, 7537, (1991).

HS90 H.Q. Hou, Y. Segawa, Y. Aoyagi, S. Namba and J.M. Zhou, Phys. Rev. **B-42**, 1284 (1990).
Also: W. Trzeciabowski and A.P. Roth, Superlattice and Microstructures, **6**, 315 (1989).

IK90 E.L. Ivchenko, V.P. Kochereshko, I.N. Uraltsev, and D.R. Yakovlev, Phys. Stat. Sol. **b 161**, 217, (1990).

IM87 Z. Ikonic, V. Milanovic and D.T. Tjapkin, Phy. Rev. Lett. **A-126**, 52, (1987).

J89 D.S. Jiang *et al*, Superlattices and Microstrucutres **6**, 387, (1989).

JB90 E.D. Jones, R.M. Biefeld, J.F. Klem, S.K. Lyo and G.C. Osbourn, Surface Science **228**, 330, (1990).

JD89 G. Ji, W. Dobbelaere, D. Huang and H. Morkoç, Phys.Rev. **B-39**, p. 3216 (1989).

JH87 G. Ji, D. Huang, U.K. Reddy, T.S. Henderson, R. Houdré, and H. Morkoç, J. Appl. Phys. **62**, 3366, (1987).

JJ88 M.J. Joyce, M.J. Johnson, M. Gal, and B.F. Usher, Phys. Rev. **B-38**, 10978, (1988).

JP90 H.X. Jiang, E.X. Ping, P. Zhou, and J.Y. Lin, Phys. Rev. **B-41**, 12 949, (1990).

KA88 R.M. Kolbas, N.G. Anderson, W.D. Laidig, Y. Sin, Y.C. Lo, K.Y. Hsieh and Y.J. Yang, IEEE J. **QE-24**, 1605 (1988).

KD68 H. Kressel, J.U. Dunse, H. Nelson and F.Z. Hawrylo, J. Appl. Phys. **39**, 2006 (1968).

KS90 A. Ksendzov, H. Shen, F.H. Pollak, D.P. Bour, Solid State Commun. **73**, 11, (1990). & Surface Science **228**, 326, (1990).

KY86 Y. Kan, M. Yamanishi, Y. Usami, and I. Suemune, IEEE J. Quan. Elec. **QE-22**, 1837, (1986).

L80 R.L. Liboff, INTRODUCTORY TO QUANTUM MECHANICS, Holden-day (1980).

LB86 NUMERICAL DATA AND FUNCTIONAL RELATIONSHIPS IN SCIENCE AND TECHNOLOGY, Landolt-Börnstein New Series, group III vol 22 a & b edited by O. Madelung.(1986).

LF86 W.W. Lui and M. Fukuma, J. Appl. Phys. 60, 1555, (1986).

LH90 J.D. Lambkin, L.K. Howard, and M.T. Emeny, Phys. Rev. **B-42**, 1738, (1990).

LS90 R.L. Liboff and S.R. Seidman, Phy. Rev. **B-42**, 9552, (1990)

M86 Y. Murayama, Phys. Rev. **B-34**, 2500, (1986).

MB82 E.E. Mendez, G. Bastard, L.L. Chang, L. Esaki, H. Morkoç and R. Fisher, Phys. Rev. **B-26**, 7101, (1982).

MB91 X. Marie, J. Barrau, B. Brousseau, T. Amand, M. Brousseau, E.V.K. Rao, and F. Alexandre, J. Appl. Phys. **69**, 812, (1991).

MC84 D.A.B. Miller, D.S. Chelma, T.C. Damen, A.C. Gossard, W. Wiegmann, T.H. Wood, and C.A. Burrus, Phys. Rev. Lett. **53**, 2173, (1984). & Phys. Rev. **B-32**, 1043, (1985).

MC85 J.Y. Marzin, M.N. Charasse, and B. Sermage, Phys. Rev. **B-31**, 8298, (1985).

MDR90 K.J Moore, G. Duggan, A. Raukema, and K. Woodbridge, Phys. Rev. **B-42**, 1326, (1990).

MDW90 K.J Moore, G. Duggan, K. Woodbridge, C. Roberts, N.J. Pulsford, and R.J. Nicholas, Phys. Rev. **B-42**, 3024, (1990).

ME90 J.M. Moison, K. Elcess, F. Houzay, J.Y. Marzin, J.M. Gérald, and M. Bensoussan, Phys. Rev. **B-41**, p. 12 945, (1990).

MK86 T. Mishima, J. Kasai, M. Morioka, Y. Sawada, Y. Katayama, Y. Shiraki, and Y. Murayama, Surface Science **174**, 307, (1986).

MP91 J.L. Merz and P.M. Petroff, Mater. Sc. Eng. **B8**, (1991).

NH86 J. Nagle, S. Hersee, M. Krakowski, T. Weil, and C. Weisbuch, Appl. Phys. Lett. **49**, 1325, (1986).

NM87 D.F. Nelson, R.C. Miller and D.A. Kleinman, Phys. Rev. **B-35**, 7770 (1987).

NR89 L.D. Nguyen, D.C. Radulescu, M.C. Foisy, P.J. Tasker and L.F. Eastman. IEEE Trans. **ED-36**, 833 (1989).

O90 H.Ohno et al, Phys. Rev. Lett. **64**, 2555, (1990).

OF90 N. Ogasawara, A. Fujiwara, N. Ohgushi, S. Fukatsu, Y. Shiraki, Y. Katayama and R. Ito, Phys. Rev. **B-42**, p. 9562, (1990).

P85 E.D. Palik, HANDBOOK OF OPTICAL CONSTANTS OF SOLIDS, Academic Press, p. 429 ff, (1985).

P88 S.H. Pan et al Phys.Rev. **B-38**, p. 3375, (1988).

P91 F.H. Pollak, Superlattices and Microstructures **10**, 333, (1991).

PA92 C. Parks, R.G. Alonso, A.K. Ramdas, M.R. Melloch, L.R. Ram-Mohan, and D. Dossa, Bull. Am. Phys. Soc. **37**, 53, (1992).

PC90 Pollak/Cardona/Aspnes, Proc. SPIE 1286, (1990).

PG88 F.H. Pollak and O.J. Glembocki, Proc. SPIE **946**, 2, (1988).

PS90 R. People and S.K. Sputz, Phys. Rev. **B-41**, 8431 (1990).

R88 U. Rössler, Solid State Com., **65**, 1279 (1988).

RC90 T. Ruf, M. Cardona, Phys. Rev. **B-41**, 10747 (1990).

RJ87 U.K. Reddy, G. Ji, T. Henderson, H. Morkoç, and J.N. Schulman, J. Appl. Phys. **62**, 145, (1987).

RJ89 U.K. Reddy, G. Ji, T. Henderson, D. Huang, R. Houdré, H. Morkoç, and C.W. Litton, J. Vac Sci. Technol. **B7**, 1106, (1989)

RM87 A.P. Roth, R.A. Masut, M. Sacilotti, P.J. D'Arcy, G.I. Sproule, D.F. Mitchell, and Y. Lepage. Can. J. Phys. **65**, 909 (1987).

S86 J.J. Song *et al*, Phys. Rev. **B-34**, 8958, (1986).

S87 J.J. Song *et al*, Appl. Phys. Lett. **50**, 1269, (1987).

S90 M. Sydor *et al*, J. Appl. Phys. **67**, 7423, (1990).

SA89 M. Sydor, J. Angelo, J.J. Wilson, W.C. Mitchel, and M.Y. Yen, Phys, Rev. **B-40**, 8473, (1989).

SC91a V. Srinivas, Y.J. Chen and Y.P. Ho, Bull. Am. Phys. Soc. **36**, (3), p. 548, (1991).

SC91b M. Sundaram, S.A. Chalmers, P.F. Hopkins, and A.C. Gossard, Science **254**, 1326, (1991).

T91 Y. S Tang, J. Appl. Phys., 69, 8298, (1991).

TB90 R.L. Tober and J.P. Bruno, International Conference on Modulation Spectroscopy, F.H. Pollak, M.Cardona, D.E. Aspnes, Editors, Proc. SPIE 1286, p.291, (1990).

TG91 W. Trzeciakowski and M. Gurioli, Phys. Rev. **B-44**, p. 3880 (1991).

V67 Y.P. Varshni, Physica **34**, 149, (1967)

VR91 C. Vázquez-López, E. Ribeiro, F. Cerdeira, P. Motisuke, M.A. Sacilotti, and A.P. Roth, J. Appl. Phys. 69, 7836, (1991).

W87 C. Weisbuch *In* SEMICONDUCTORS AND SEMIMETALS. Vol. 24. *Edited by* R. Dingle. Academic Press Inc. New-York. 1987. Chap. 1.

WV91 QUANTUM SEMICONDUCTOR STRUCTURES by C. Weisbuch and B. Vinter, Academic Press 1991.

Z91 W. Zhou et al, J. Appl. Phys., 69, p. 4075, (1991).

ZP84 J.E. Zucker, A. Pinczuk, D.S. Chemla, A. Gossard and W. Weigmann, Phys. Rev. **B-29**, 7065, (1984).